Study of the Performance of Different Subgrid-Scale Models and Large Eddy Simulation of Premixed Combustion

Vom Fachbereich Maschinenbau

an der Technischen Universität Darmstadt

zur

Erlangung des Grades eines Doktor-Ingenieurs (Dr.-Ing.)

genehmigte

Dissertation

vorgelegt von

M.S. Rajani Kumar Akula

aus Visakhapatnam, Indian

Berichterstatter:	Prof. Dr.-Ing. Johannes Janicka
Mitberichterstatter:	Prof. Dr. Rer.nat.Michael Pfitzner
Tag der Einreichung:	06.10.2006
Tag der mündlichen Prüfung:	06.02.2007

Darmstadt 2006

D17

Acknowledgements

The present work has been carried out at the Institute of Energy and Powerplant Technology, Department of Mechanical Engineering, Darmstadt University of Technology. The financial support comes from the Deutsche Forschungs gemeinschaft (DFG).

I would like to express my sincere gratitude to my supervisor, Prof. Johannes Janicka, for giving so much freedom to me and sharing some of his profound knowledge in modelling of combustion with me. This thesis would never have reached this point without his encouragement and brilliant advice. I would also want to thank him for his limitless patience.

I wish to thank Prof. Dr. Rer. nat. Michael Pfitzner for his willingness to report on my work.

I would also want to thank Prof. rer. nat. A. Sadiki, for useful discussions and constant encouragement.

My thanks to all of my colleagues, especially Bernhard Wegner, Dr. Alexander Maltsev, Dr. Andreas Kempf, Dr. Michael Düsing, Dr. Markus Klein, Felix flemming, Martin Freitag and Dr. Elena Schneider for the helpful discussions. I wish to thank Ranga reddy, Mouldi Chrigui, Jesus, Clemens and other EKT colleagues for the pleasant working atmosphere during my stay at EKT. I take this opportunity to thank all EKT staff for their kind support.

I wish to thank Dr. Sunil Omar, Dr. Rahul Harshe, Dr. Sandeep, Himanshu, Swathi, Chakrapani, Debashis, Poonam and Dr. Rama Subramanium for their moral support and great time we had together.

Last, but not least, I owe a great debt of gratitude to my family specially my parents, who have always been very loving, supportive and believed in my abilities.

Rajani Kumar Akula
Darmstadt, October 2006

To my parents

Contents

Nomenclature

Latin symbols

Symbol	Dimension	Definition
A_L and A_M	m^2	Laminar and turbulent flame front area
A_{fj}	-	Pre-exponential frequency factor in Arrhenius law for elementary reaction j
b	-	Regress variable
C	-	Progress variable or model constant
C_d , C_{ε}, C_S, C_p	-	Model constants
D	s^{-1}	Diffusion coefficient
Da	-	Damköhler number
E_j	J/kg	Activation Energy for species k
E_ω	m^3/s^2	Turbulent kinetic enrgy density
g	m/s^2	Gravity acceleration
$G(\ )$	-	Filter function
Ka	-	Karlovitz number
K_{fj} and K_{rj}	-	Forward and reverse constants of the reaction rates
k_ω	$1/m$	Wave number
k_{sgs}		Subgrid scale kinetic energy
L	m	Characteristic length scale
L_{ij}		Leonardo stress term
Le	-	Lewis number
l_t		Integral length scale
l_F	m	Laminar flame thickness
p	pa	Static pressure
Pr	-	Prandtl number
R		Ideal gas constant
R_{ij}^L and R_{ij}^T		Spatial and Time correlation function
Re	-	Reynolds number
u	m/s	Velocity
S_L , S_d and S_t	m/s	Laminar flame speed, displacement flame speed and turbulent flame speed respectively
Sc	-	Schmidt number
$\overline{S}_{ij}$		Filtered rate-of-strain tensor
t	s	Time
T	K	Temperature or time scale
T_t	s	Integral turbulent time scale
T_{ij} and τ_{ij}		Sub test and grid stresses
x,y,z	m	Cartesien coordinates

y_k	-	Mass fraction of species *k*
z	-	Mixture fraction

Greek symbols

Symbol	Dimension	Definition
ρ	Kg/m^2	Density
ε		Kinetic energy dissipation rate
δ_{ij}		Kronecker delta
η_k	m	Kolmogorov length scale
ν	m^2/s	Kinematic viscosity
τ_k	s	Kolmogorov time scale
Δ	m	Filter width
ω	s^{-1}	Spatial frequency
$\dot{\omega}_{kj}$	$kg/m^3 s$	Reaction rate
Ξ		Flame wrinkling factor
Σ		Flame surface density
Ω		Angular velocity
ψ		Conserved variable
σ		Surface

Abbreviations

Abbreviation	Definition
BML	Bray-Moss-Libby
CDS	Central Difference Scheme
CFM	Coherent Flame Model
CMC	Conditional Moment Closure
EBU	Eddy-Break-Up model
EDM	Eddy-Dissipation model
FSD	Flame Surface Density
ILDM	Intrinsic Low Dimentional Manifolds
LDA	Laser Doppler Anemometry
LES	Large Eddy Simulation
LHS	Left Hand Side
NSE	Navier-Stokes equations
PDF	Probability DensityFunction
RANS	Reynolds Averaging based numerical Simulation
RHS	Right hand side
RMS	Root Mean Square
SGS	Subgrid scale
SIP	Strongly Implicit Pressure
UDS	Upwind
ZFK	Zeldovich Frank Kamenetsky von Karman theory

Chapter 1

Introduction

1.1 Motivation and Objective

The energy generation over the world remains primarily due to the fossil fuel. Over 80% of all the energy produced by combustion (Coal, Gas, Oil) [1]. During the last decades many attempts have been paid towards the renewable energy. Among the most important of these sources are solar and wind. They are characterized by their environmental cleanliness and their virtual inexhaustibility. In most cases, however, they are not suitable for large-scale power generation as well as relatively expensive to build and maintain. Despite its known disadvantages, combustion remains the cheapest and the most direct way to generate energy. It is therefore important to seek for improvements of combustion processes in order to promote the efficiency of the energy conversion. The combustion process typically burns fuel in a device to create heat and power. Most fuels are mixtures of hydrocarbons, e.g. gasoline and diesel fuels, which are compounds that contain hydrogen and carbon atoms. In 'perfect' combustion, oxygen in the air would combine with all the hydrogen in the fuel to form water and with all the carbon in the fuel to form carbon dioxide. Nitrogen in the air would remain unaffected. In reality, the combustion process is not 'perfect', and combustion devices emit several types of pollutants as combustion by-products. Pollutants generated by combustion include particulate matter [2,3], such as fly ash, soot, various aerosols, etc.; the sulphur oxides, SO2 and SO3; unburned and partially burned hydrocarbons (UHC); oxides of nitrogen, NO*x*, which represents the combination of NO and NO2; carbon monoxide, CO; and greenhouse gases, particularly CO2. These pollutants affect our environment and human health in many ways.

Many advanced combustors have been developed up to date to satisfy the emission limits; however, they are still facing many problems. For example, there are many problems that are related to the lean combustion: lean blow-off, flame stabilization, acoustic resonance, and so on. Considering the future coming more stringent emission limits, the working condition of the combustors will be more rigorous, and the problems will be more serious. To meet this high industry demand, a deeper and better understanding of the physics of the turbulent combustion process is required. In doing this, both experimental and computational studies

are necessary. During the last twenty years, substantial experimental studies have been conducted with non-intrusive optical measuring equipments. They have proven successful in providing information on turbulence and flame structures, interaction between turbulence and combustion, and have become standard tools in combustion research. Based on the data obtained using these measuring techniques, a better understanding of the complex physical and chemical mechanisms that govern turbulent combustion can be expected. A recent review of the combustion diagnostic techniques based on laser equipments is given by [4].

The experimental studies, however, suffer from many limitations, such as the time required to design, manufacture, prepare experimental setup, high cost of the setup and measuring equipments, and especially, they can not provide detailed whole flow field information. Due to these limitations, the main objectives of the experimental studies are not to help combustor design directly, but to improve the physical understanding of the combustion process and to provide databases for validation or development of the combustion prediction models.

On the other hand, in the design process of economically efficient as well as ecologically justifiable combustion applications, the numerical simulation of technically relevant combustion phenomena has gained increasing importance in the recent years. In the past, numerical simulation of combustion processes in turbulent flows has been primarily the focus of scientific research. Also formerly, design and process advancement were primarily due to the intuitive ideas and experimental analysis. Now, numerical simulation of the combustion process promises a fast and inexpensive method to supplement and even advance the design process. Secondly, computational resources have increased exponentially over time. Thus, today, and especially in the near future, the computational power needed to model turbulent premixed combustion processes is available, not only in scientific research but also for industrial applications. The combustion models presented in this work aims at the industrial design process. These models require relatively less computational resources compared to other methods like levelset techniques [56] whilst retaining the relevant underlying physics of turbulent premixed combustion.

In premixed combustion flows, fuel and oxidizer are mixed on a molecular level. If the mixture lies within the flammability limits, a local increase in temperature, for example by a spark, initiates the combustion process. The chemical reactions taking place are typically very fast, so that propagating thin flame fronts develop whose widths are in the order of a tenth of a mille metre in the case of hydrocarbon fuels. The propagation of the premixed combustion front normal to itself, the so-called burning velocity, is the key feature of premixed

combustion. In turbulent premixed flows proper capturing of the turbulence–combustion interactions is important. Even though, direct numerical simulations (DNS) of Navier-Stokes equations can predict turbulence without models, these types of simulations are restricted to very simple geometries. On the other hand, The Large eddy simulations (LES) are now viewed as a promising tool to address turbulent combustion flows where classical Reynolds-averaging numerical simulations (RANS) approaches have proved to lack precision or where the intrinsically unsteady nature of the flow makes RANS clearly inadequate. LES allows a better description of the turbulence–combustion interactions because large structures are explicitly computed and instantaneous fresh and burnt gas zones, where turbulence characteristics are quite different, are clearly identified. But LES of premixed combustion is difficult due to the thickness of the premixed flame is about 0.1–1 mm and generally smaller than the LES mesh size. By using progress variable approaches it is very difficult to resolve the flame front. To overcome this difficulty certain modifications have to be made for the progress variable equation. For this purpose, by using flame surface density approach [57] and the artificially thickened flame model [58] large eddy simulation of premixed combustion is performed in this work. Nevertheless for better modelling of premixed combustion one has to capture the turbulence as accurately as possible and which requires better understanding of SGS models.

So, for good numerical simulations of the turbulent premixed combustion one has to model the turbulence properly. For this a detailed study of the SGS models is required in the case of LES. In this work, first detailed study of the different SGS models have presented. In the later part of the thesis LES of premixed combustion is presented by considering flame surface density model and the artificial thickened model.

1.2 Structure of the Thesis

This work is arranged into seven main chapters.

In chapter 2, basics of the turbulence and the combustion are presented. First an overview of the turbulence and its modelling techniques are discussed with more emphasis on large eddy simulation. Thereafter different combustion processes are presented. Additionally, premixed combustion is explained in detail.

In Chapter 3, subgrid scale (SGS) modeling in large eddy simulation is presented. In the first part, necessary requirements of the SGS modeling are discussed. In the second part different SGS models, which are used in the present work, are discussed in detail.

Chapter 4 describes the modelling techniques for turbulent premixed flames. Initially the basic difficulties existing in the modelling of the premixed flames are presented and then various modelling techniques for the premixed flames are discussed. Especially modelling techniques based on the progress variable are presented clearly. Finally different techniques to handle the flame-wrinkling and flame-wall interactions are presented.

Chapter 5 introduces the numerical procedure used. First the basic structure of the FASTEST3D code is presented. Additionally, the numerical technique which is proposed for the extension of the incompressible solver to variable density solver is presented.

Chapter 6 contain results and discussions. In this chapter, some applications of the derived LES code to the simulation of non-reactive flows and premixed combustion are presented. In the first part a study of the performance of different SGS models is presented. In the last part LES of the bluff-body stabilized premixed flame by considering flame surface density and thickened flame model are presented.

Finally, Chapter 7 summarizes the contents of this thesis and suggests some possible directions for future research.

Chapter 2

Basics of the turbulence and combustion

In this chapter the basics of the turbulence and the combustion or presented. First an overview of the turbulence and its modelling techniques are presented with more emphasis on large eddy simulation. In the second part basics of the combustion are presented. Additionally, premixed combustion is explained in detail.

2.1 Turbulence simulation

Turbulence is experienced by us every day. Fluid flows around cars, ships and airplanes can be turbulent. Atmospheric flows, water currents below the ocean's surface and rivers can be characterized as turbulent as well. Many other examples of turbulent flows arise in aeronautics, hydraulics, nuclear and chemical engineering, environmental sciences, oceanography, meteorology, and others. The incompressible Navier-Stokes equations contain a full description of turbulence given that they describe the motion of every Newtonian incompressible fluid based on conservation principles without further assumptions.

Unfortunately, except for very simple flows, there is no analytical solution to these equations. Moreover, the Navier-Stokes equations can exhibit great sensitivity to initial and boundary conditions leading to unpredictable chaotic behaviour. Although the fundamental laws behind the Navier-Stokes equations are purely deterministic, these equations, similar to other simpler deterministic equations, can often behave chaotically under certain conditions. For laminar flows, analytical or numerical solutions can be directly compared to experimental results. However, due to the randomness in turbulent flows, it is hopeless to track instantaneous behaviour. Instead, the goal is to measure this behaviour in the temporal or spatial mean.

2.1.1 Physical description of turbulence

There is no widely accepted definition of turbulence, as it is one of the least-known physical processes. Here are some of the features of the turbulence:

- Turbulent flows are irregular. This is a very important feature, appearing in almost any definition of turbulence [5]. Because of irregularity, the deterministic approach to turbulence becomes impractical, in that it appears impossible to describe the turbulent

motion in all details as a function of space and time. However, it is believed possible to indicate average (in time and/or space) velocity and pressure.

- Turbulent flows are diffusive. This causes rapid mixing and increased rates of momentum, heat and mass transfer. Turbulent flows should be able to mix passive transported quantities such as temperature, density, etc. much more rapidly than if only molecular diffusion processes were involved. For example, if a passive scalar is being transported by the flow, a certain amount of mixing will occur due to molecular diffusion. In a turbulent flow, a similar mixing occurs, but with a much greater amount than predicted by molecular diffusion. From the practical stand point, diffusivity is very important. The engineer, for instance, is mainly concerned with the knowledge of turbulent heat diffusion coefficients, or the turbulent drag (depending on turbulent momentum diffusion in the flow).

- Turbulent flows are rotational. For a large class of flows, turbulence arises due to the presence of boundaries or obstacles, which create vorticity inside a flow which was initially irrotational. Turbulence is thus associated to vorticity, and it is impossible to imagine a turbulent irrotational flow.

- Turbulent flows occur at high Reynolds numbers. The Reynolds number represents the ratio between inertial forces and viscous forces in the flow. Turbulence often arises from instabilities in laminar flows when the Reynolds number becomes high enough. These instabilities are related to the complex interaction of viscous and convective (inertial) influences.

- Turbulent flows are dissipative. Viscosity effects result in the conversion of kinetic energy of the flow into heat. If there is no external source of energy to make up for this kinetic energy loss, the turbulent motion will decay.

- Turbulent flows are characterized by a wide range of scales of motions, unlike in laminar flows in which there are usually a few scales. As per Kolmogorov's theory [5], which has been demonstrated countless of times through experiments as well as computations, energy is transferred from the largest to the smallest scales at which point viscosity acts as a converter of energy into heat.

- Turbulent flows are continuum phenomena. Even the smallest scales in a turbulent flow are ordinarily far larger than any molecular length scale.

- Turbulence is a feature of fluid flows, and not of fluids. If the Reynolds number is high enough, most of the dynamics associated to the smaller scales in the turbulence is the same in all fluids. In short, the main characteristics of turbulent flows are not controlled by the molecular properties of the particular fluid.

First, let us take a look at the equations that govern turbulent flows. In the following section governing equations for the turbulent flows are presented.

2.1.2 Mathematical description of turbulence

The governing equations describing any incompressible Newtonian fluid motion including turbulence are the well-known Navier-Stokes equations (NSE):

$$\frac{\partial \rho}{\partial t} + \frac{\partial \rho u_i}{\partial x_i} = 0 \tag{2.1}$$

$$\frac{\partial \rho u_i}{\partial t} + \frac{\partial \rho u_i u_j}{\partial x_j} = -\frac{\partial p}{\partial x_i} + \frac{\partial}{\partial x_j}\left[\rho \nu \left(\frac{\partial u_j}{\partial x_i} + \frac{\partial u_i}{\partial x_j}\right)\right] + \rho g_i \tag{2.2}$$

In the equations (2.1) and (2.2), ρ represents density and u_i ($i = 1, 2, 3$) denotes three components of the velocity along the x_i direction. In the equation (2.2), g_i represents gravity acceleration; p is pressure and ν is kinematic viscosity.

Thus, since all turbulent flows satisfy the Navier-Stokes equations, it seems natural to use a mathematical approach in trying to understand turbulence. However, the present state of the mathematical theory of the Navier-Stokes equations is not encouraging. Except for very simple settings like Couette flow or Poiseuille flow, we do not have an analytical solution.

2.1.3 Characteristic Turbulent Time and Length Scales

Turbulent flows are characterized by the existence of a multitude of eddies of different sizes. This is due to the fact that in high Reynolds number turbulent flows large eddies break up into smaller eddies which in turn break up into even smaller eddies. This process continues until viscous forces start to dominate and the smallest eddies are dissipated. This so-called eddy cascade hypothesis goes back to Kolmogorov's theory for homogeneous, isotropic turbulence [6, 7]. It states that a stationary energy transfer from the large eddies down to the smallest eddies occurs in the so-called inertial subrange of turbulence. This energy transfer is local in the sense that energy from one eddy is transferred only to the eddy of the next smaller length scale. Due to the locality of the energy transfer, the energy transfer rate, i.e., the kinetic energy per eddy turnover time, is independent of the length scale of the eddies and thus constant within the inertial subrange. This scale invariance is the most important hypothesis

for large Reynolds number flows. It is integrated into every standard turbulence model, thereby satisfying the requirement of Reynolds number independence in the large Reynolds number limit, and a model for turbulent combustion should also abide by this premise.

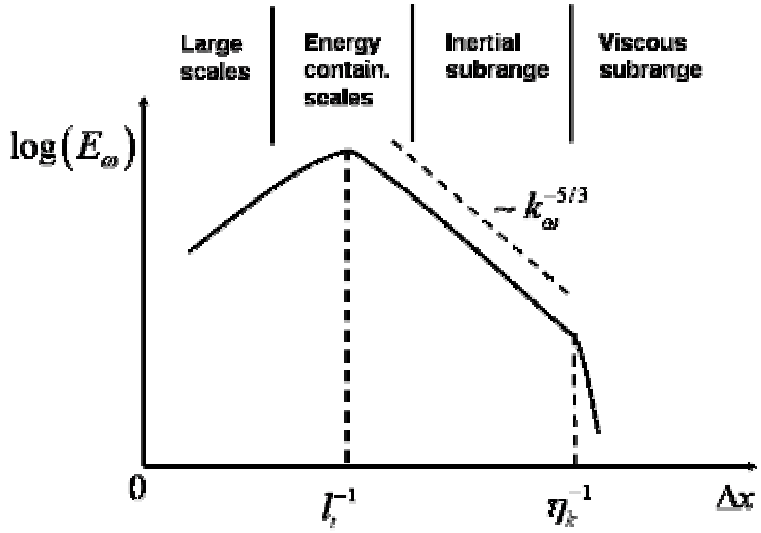

Figure 2.1 *Energy spectrum*

Fig. 2.1 shows the energy spectrum $E_\omega(k_\omega)$ of homogeneous, isotropic turbulence as a function of the reciprocal of the eddy size, the wave number k_ω. The constant energy transfer rate in the inertial subrange leads to a slope of -5/3, which results from dimensional analysis. Two important characteristic turbulent length scales bounding the inertial subrange can also be identified in this figure, the Kolmogorov length scale η_k and the integral length scale l_t. The Kolmogorov length scale η_k denotes the scale of the smallest eddies. At this length scale, viscous forces dominate and thereby converting the kinetic energy of the smallest eddies into thermal energy. The Kolmogorov length scale thus has to be a function of the kinematic viscosity ν and the kinetic energy dissipation rate ε. It can be determined by dimensional analysis as:

$$\eta_k = \frac{\nu^{3/4}}{\varepsilon^{1/4}} \tag{2.3}$$

In addition, the Kolmogorov time scale τ_k, which is proportional to the turnover time of a Kolmogorov eddy, can be calculated by dimensional analysis as:

$$\tau_k = \frac{\nu^{1/2}}{\varepsilon^{1/2}} \tag{2.4}$$

The integral length scale l_t corresponds to the length scale of those eddies that contain the most energy. The integral length scale can be defined with the help of the two-point spatial correlation function for statistically steady (time independent) turbulence

$$R_{ij}^{L}\left(x, x+\Delta x\right)=\frac{\overline{u_i^{'}\left(x\right)u_j^{'}\left(x+\Delta x\right)}}{\sqrt{\overline{u_i^{'2}\left(x\right)}}\sqrt{\overline{u_i^{'2}\left(x+\Delta x\right)}}} \tag{2.5}$$

as

$$L_{ij}(x)=\frac{1}{2}\int_{-\infty}^{+\infty}R_{ij}^{L}\left(x, x+\Delta x\right)d\left(\Delta x\right) \tag{2.6}$$

Here, L_{ij} denotes the length scale tensor. For homogeneous isotropic turbulence the integral length scale is independent of the direction and is given by

$$l_t=\frac{1}{3}L_{ii} \tag{2.7}$$

The two-point velocity correlation function for homogeneous isotropic turbulence and the corresponding integral turbulent length scale are schematically shown in Fig. 2.2. The corresponding time scale can be determined from the known time correlation function

$$R_{ij}^{T}\left(x,t,t+\Delta t\right)=\frac{\overline{u_i^{'}\left(t\right)u_j^{'}\left(t+\Delta t\right)}}{\sqrt{\overline{u_i^{'2}\left(t\right)}}\sqrt{\overline{u_i^{'2}\left(t+\Delta t\right)}}} \tag{2.8}$$

as

$$T_{ij}(x)=\frac{1}{2}\int_{-\infty}^{+\infty}R_{ij}^{T}\left(x,t,t+\Delta t\right)d\left(\Delta t\right) \tag{2.9}$$

Assuming isotropy and homogeneity leads to

$$T_t=\frac{1}{3}T_{ii} \tag{2.10}$$

Qualitatively the integral turbulent time scale can be interpreted as an averaged inverse rotational frequency of the typical big eddy appearing in the spatial location *x*.

Though turbulence in practical flows is neither isotropic nor homogeneous, the idealized integral length scale in equation (2.7) provides at least coarse quantitative information about spatial correlation and sizes of typical energy containing eddies in turbulent flows.

Qualitatively the integral turbulent length scale can be interpreted as an averaged radius of the typical big eddy appearing in the spatial location *x*.

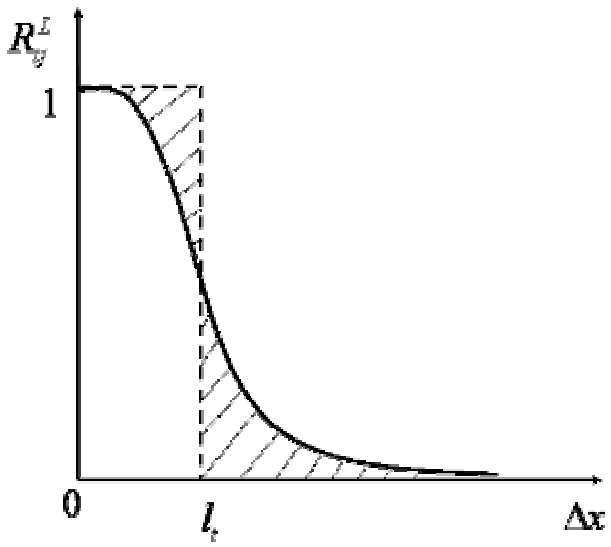

Figure 2.2 Two-point velocity correlation function versus the distance between two point Δx for homogeneous isotropic turbulence

The turbulent kinetic energy spectrum obtained from the Fourier transformation of the spatial isotropic two-point correlation function R_{ij}^L is schematically plotted in Fig. 2.1. $E_\omega\left(k_\omega\right)$ is the kinetic energy density per wave number k_ω or the inverse turbulent length scale.

2.1.4 Numerical Approach to Turbulence

As we have seen from the previous sections, both approaches (mathematical and physical) are pretty far from giving a complete answer to the understanding of turbulence. However, mainly due to the efforts in the engineering and geophysics communities, the numerical simulation of turbulent flows emerged as an essential approach in tackling the turbulence. Even though the numerical approach has undeniable accomplishments, it is by no means an easy and straightforward one. In the following sections some of the simulation techniques are presented.

2.1.4.1 Direct numerical simulation (DNS)

The most natural approach to turbulence is direct numerical simulation (DNS), in which all the scales of motion are simulated or resolved by the numerical method solely using the Navier-Stokes equations. As discussed earlier, the range of scales of motions in a turbulent flow grows with the Reynolds number. More specifically, small scales exist down to $O\left(Re^{-3/4}\right)$, as per Kolmogorov's theory discussed in any introductory turbulence text such

as (2.1). Thus, in order to capture all of the scales on a grid, a grid size of $h \approx Re^{-3/4}$ is required, translating to a grid of approximately $Re^{9/4}$ grid points. One can get a fair idea of the large numbers of grid points required in a DNS by looking the following some typical Reynolds numbers encountered in turbulent flows of interest.

- Flow around a model airplane with characteristic length and velocity scales of 1 m and 1 m/s, respectively: $Re \approx 7 \cdot 10^4$
- Flow around cars with characteristic velocity of 3 m/s: $Re \approx 6 \cdot 10^5$
- Flow around airplanes with characteristic velocity of 30 m/s: $Re \approx 2 \cdot 10^7$
- Atmospheric flows: $Re \approx 2 \cdot 10^7$

Thus, for $Re \approx 10^6$, a reasonable number for many flows of practical interest, the number of grid points would be about $10^{13.5}$. Present computational resources make such calculations impractical. Moreover, in an expensive DNS a huge amount of information would be generated which is mostly not required by the practical user. He or she would mostly be content with knowing the average flow and some lower moments to a precision of a few percent. Hence, for many applications a DNS which is of great value for theoretical investigations and model testing is not only unaffordable but would also result in computational overkill.

Even though DNS is unsuited for most simulations of interest, in some cases it can be a useful tool to validate turbulence models. For example Kim *et al.* in [8] present a DNS of channel flow, and Le *et al.* in [9] present a DNS of flow over a backward-facing step. Both of these studies were conducted to gain new insight into the physical mechanisms involved in turbulent flow.

Because the DNS approach, based solely on the Navier-Stokes equations, is not suitable for most turbulent flows, researchers had to find different approaches. The first of such approach is that of the Reynolds-averaged Navier-Stokes equations.

2.1.4.2 Reynolds-averaging: Reynolds-averaged Navier-Stokes simulation (RANS)

As was pointed out earlier, irregularity is one of the most important features in turbulent flows. Even though it seems impossible to describe the turbulent motion in all details as a function of time and space coordinates, it appears possible to indicate average values of the flow variables (velocity and pressure). As is pointed out in [10], mere observation of turbulent flows and time histories of turbulent quantities show that these averages exist because of the following reasons:

1. At a given point in the turbulent flow domain a distinct pattern is repeated more or irregularly in time.

2. At a given instant a distinct pattern is repeated more or less irregularly in space; so turbulence, broadly speaking, has the same over-all structure throughout the domain considered.

Furthermore, although general assumptions regarding the behaviour of the smallest scales lead to turbulence models, details of the motion at this level are not of interest for most applications in engineering and geophysics. Motivated by the latter, Osborne Reynolds developed a statistical approach in 1895 and derived the famous equations that bear his name to describe the dynamics of the mean or average flow, otherwise the largest of the scales. Formally, the Reynolds equations are obtained from the Navier-Stokes equations (2.1) and (2.2) by decomposing the velocity *u* and the pressure *p* into mean (average) and fluctuation components as

$$u = \overline{u} + u' \quad ; \quad p = \overline{p} + p' \tag{2.11}$$

where the fluctuations reflect the turbulent intensities of the variables. There are essentially two ways to define the mean components $\overline{u}$ and $\overline{p}$. These are ensemble averaging and time averaging:

Ensemble Averaging: This is done by performing many physical experiments on the same problem, measuring the velocity and pressure at every time and at every point in the domain, and then averaging over this set of experimental data. Ensemble averaging can be done via multiple realizations of a physical experiment or via multiple computational simulations with white noise introduced into the problem data such as boundary and initial conditions.

Time Averaging: This was Reynold's original approach, who defined the mean flow variables as

$$\overline{u}(x,t) = \frac{1}{T}\int_t^{t+T} u(\lambda,x)\,d\lambda, \quad \overline{p}(x,t) = \frac{1}{T}\int_t^{t+T} p(\lambda,x)\,d\lambda \tag{2.12}$$

The time scale *T* has to be sufficiently long that choosing a larger time scale would produce the same mean components. At the same time, *T* should be short enough relative to temporal variations in the mean not associated with turbulence as vortex shedding. For statistically stationary turbulence, the means are time independent thus they can be defined as

$$\bar{u}(x)=\frac{1}{T}\int_t^{t+T} u(x,t)\,dt,\quad \bar{p}(x)=\frac{1}{T}\int_t^{t+T} p(x,t)\,dt \tag{2.13}$$

In the limit as $T\to\infty$ the following properties hold for the means and fluctuations of *u* and *p*:

$$\bar{\bar{u}}=\bar{u},\ \bar{\bar{p}}=\bar{p},\ \bar{u}'=0,\ \bar{p}'=0 \tag{2.14}$$

The previous conditions are often imposed when approximating a sufficiently large *T*.

Substitution of the decomposition given in equation (2.11) into the Navier-Stokes equations (2.1) and (2.2) leads to the well-known Reynolds-averaged Navier-Stokes equations. These are of the same form as the original ones, except that they describe the behaviour of $(\bar{u},\bar{p})$ instead of (u,p). Furthermore, in addition to the mean viscous stress in terms of the gradient of $\bar{u}$, the Reynolds-averaged Navier-Stokes equations also possess a second stress, namely the Reynolds stress, representing the influence of the fluctuating components upon the mean flow components $(\bar{u},\bar{p})$. Resulting Reynolds averaged equations are given by

$$\frac{\partial\bar{\rho}}{\partial t}+\frac{\partial\overline{\rho u_i}}{\partial x_i}=0 \tag{2.15}$$

$$\frac{\partial\left(\overline{\rho u_i}\right)}{\partial t}+\frac{\partial\left(\overline{\rho u_j u_i}\right)}{\partial x_j}=-\frac{\partial\bar{p}}{\partial x_i}+\frac{\partial}{\partial x_j}\left(\bar{\rho}\nu\left(\frac{\partial\bar{u}_j}{\partial x_i}+\frac{\partial\bar{u}_i}{\partial x_j}\right)-\overline{\rho u_i' u_j'}\right)+\bar{\rho}g_i \tag{2.16}$$

In the equation (2.16), the new term $\overline{u_i' u_j'}$ is called as Reynolds stress tensor and one has to model it. There are different models available in the literature. Numerical solution of the Reynolds-averaged Navier-Stokes equations together with a model for the Reynolds stress is what is referred to as Reynolds-averaged Navier-Stokes simulation (RANS). The present work will not focus on the Reynolds-averaged Navier-Stokes equations and its closure problem. Instead, it will focus on an analogous set of equations referred to as the filtered Navier-Stokes equations, introduced in the following subsection.

2.1.4.3 Spatial filtering: Large-eddy simulation (LES)

In the spatial filtering approach to turbulence, a low-pass, local, spatial filter is applied to the Navier-Stokes equations, instead of an ensemble or temporal average. The main idea is similar to that of Reynolds-averaging in which the equations governing the mean components of the flow are derived. The mean components can be thought of as the *largest* of the scales in the turbulence. With spatial filtering, the equations governing the *larger* components of the

turbulent scales are derived. Spatial filtering decomposes the variables into two components as

$$u = \bar{u} + u' \text{ and } p = \bar{p} + p' \tag{2.17}$$

Here $\bar{u}$ and $\bar{p}$ are the resolved (filtered or larger) components and u' and p' are the residual (subgrid or smaller) components.

The effect of filtering can be seen in the sketch shown in Fig. 2.3 in which the filtered component of a function and the original function are depicted. The filtering operation serves to damp scales on the order of the filter width denoted as Δ. The width is a certain characteristic length of the filter.

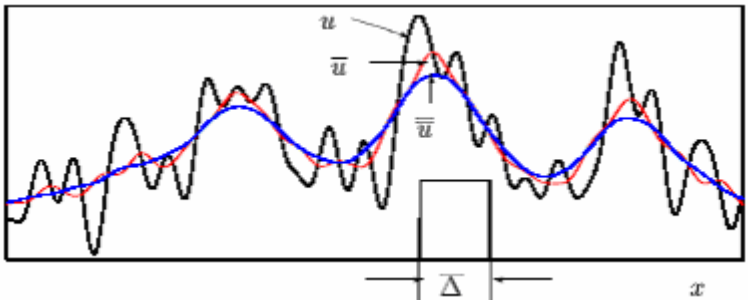

Figure 2.3 *Filtered functions $\bar{\bar{u}}$ and $\bar{u}$ obtained from $u(x)$ by applying a box filter*

Leonard [5] proposed to define $\bar{u}(x)$ by

$$\bar{u}(x) = \int_{-\infty}^{+\infty} G(x - x')u(x')dx' \tag{2.18}$$

An integral of this kind is called a convolution. Here, *G* is a compactly supported or at least rapidly decaying filter function with $\int G(x)dx = 1$ and width Δ. The latter can be defined by the second moment of *G* as $\Delta = \sqrt{12\int x^2 G(x)dx}$.

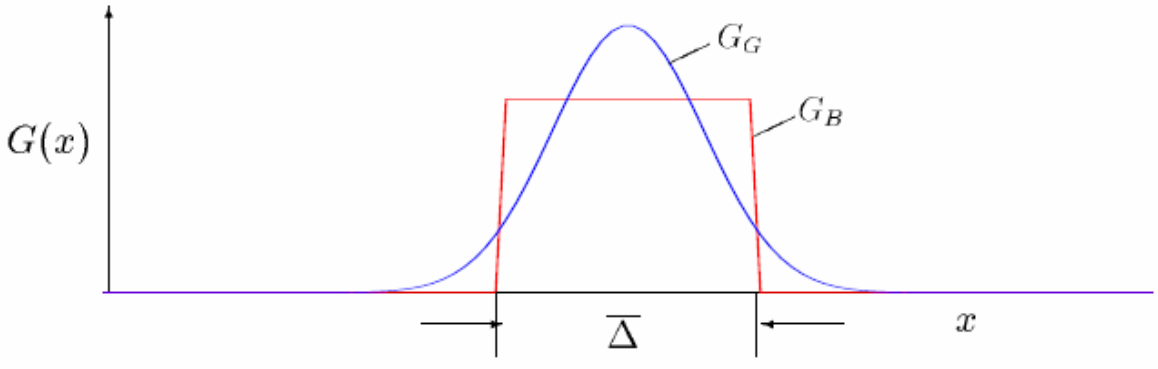

Figure 2.4 *Gaussian filter G_G and box filter G_B*

Fig. 2.4 displays the Gaussian filter $G_G = \sqrt{6/\pi}\,1/\Delta\, exp\left(-6x^2/\Delta^2\right)$ and the box filter defined by $G_B = 1/\Delta$ if $|x| \le \Delta/2$ and $G_B = 0$ elsewhere. According to equation (2.18), $\overline{u}(x)$ is a continuous smooth function as displayed in Fig. 2.3 which can subsequently be discretized by any numerical method. This has the advantage that one can separate conceptually the filtering from the discretization issue.

It is helpful to transfer equation (2.18) to Fourier space by means of the definition $\hat{u}(\omega) = \int u(\omega) e^{-i\omega x} dx$, since in Fourier space, where the spatial frequency ω is the independent variable, a convolution integral turns into a simple product. Equation (2.18) then reads

$$\hat{\overline{u}}(\omega) = \hat{G}(\omega)\hat{u}(\omega) \tag{2.19}$$

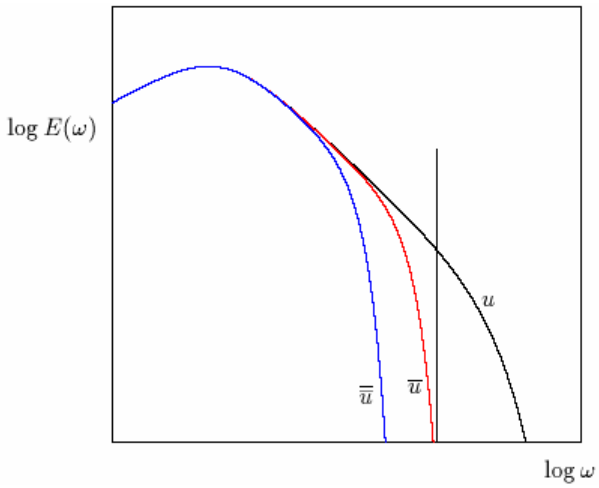

Figure 2.5 *Effect of filtering on the spectrum*

Fig. 2.5 illustrates the filtering in Fourier space. Equation (2.19) allows the definition of another filter, the Fourier cut-off filter with $\hat{G}_F(\omega) = 1$ if $|\omega| \le \pi/\Delta$ and 0 elsewhere. From equation (2.19) it is obvious that only this filter yields $\overline{\overline{u}} = \overline{u}$, since $\left(\hat{G}_F\right)^2 = \hat{G}_F$. In all other cases the identity is not fulfilled. This can be understood by comparing $\overline{u}$ and $\overline{\overline{u}}$ for the box filter in Fig. 2.3 and 2.5. In filtering operations following relations are true for the box filter or Gaussian filter:

$$\overline{\overline{u}} \neq \overline{u},\ \overline{u\overline{v}} \neq \overline{u}\,\overline{v} \tag{2.20}$$

which distinguishes clearly the filtering in LES from Reynolds averaging given in equation (2.14) (see Germano [11]). The vertical line in Fig. 2.5 represents the nominal cutoff at $\pi/\overline{\Delta}$ related to the grid. The Fourier cutoff filter $\widehat{G_F}$ would yield a spectrum of *u* which is equal to the one of *u* left of this line and zero right of it. Equation (2.19) and Fig. 2.5 therefore demonstrate that when a general filter is applied, such as the box filter, this does not yield a neat cut through the energy spectrum but rather some smoother decay to zero. This is important since SGS modelling often assumes that the spectrum of the resolved scales near the cutoff follows an inertial spectrum with a particular slope and a particular amount of energy transported from the coarse to the fine scales on the average.

Applying the three dimensional equivalent of the filter in equation (2.18) to the equation (2.1) and (2.2), the following equations for the filtered velocity components $\overline{u}_i$ result

$$\frac{\partial \overline{\rho}}{\partial t} + \frac{\partial \overline{\rho}\overline{u_i}}{\partial x_i} = 0 \tag{2.21}$$

$$\frac{\partial \left(\overline{\rho}\overline{u_i}\right)}{\partial t} + \frac{\partial \left(\overline{\rho}\overline{u_j}\overline{u_i}\right)}{\partial x_j} = -\frac{\partial \overline{p}}{\partial x_i} + \frac{\partial}{\partial x_j}\left(\overline{\rho\nu}\left(\frac{\partial \overline{u_j}}{\partial x_i} + \frac{\partial \overline{u_i}}{\partial x_j}\right) - \tau_{ij}\right) + \overline{\rho} g_i \tag{2.22}$$

τ_{ij} represents the impact of the unresolved velocity components on the resolved ones and has to be modelled. In mathematical terms it arises from the nonlinearity of the convection term which does not commute with the linear filtering operation. There are two different procedures exist based on the type of filtering operation. These are implicit and explicit filtering procedures. Eventhough the present work follows the implicit filtering approach some differences between these approaches are explained in the following section.

2.1.4.4 Implicit filtering versus explicit filtering

The filtering approach relaxes the link between the size of the computed scales and the size of the grid since the filter can be coarser than the employed grid. Consequently, the modelled motion should be called subfilter rather than subgrid scale motion. The latter labelling results from the Schumann type approach and is frequently used for historical reasons to designate the former. In practice, however, the filter *G* does not appear explicitly at all in many LES codes, so that in fact the Schumann approach is followed. Due to the conceptual advantages of the filtering approach reconciliation of both is generally attempted in two ways. The first observation is that a finite difference method for equations (2.21) and (2.22) with a box filter

employs the same discrete unknowns as Schumann's approach, such as $\overline{u}(x_k) = {}^{V_k}\overline{u}$ (volume averaging) with k referring to a grid point. Choosing appropriate finite difference formulae the same or very similar discretization matrices are obtained in both cases. Another argument is that the definition of discrete unknowns amounts to an 'implicit filtering' - i.e., filtering with some unknown filter (but one that in principle exists) -since any scale smaller than the grid is automatically discarded. In this way the filter is more or less used symbolically only to make the effect of a later discretization appears in the continuous equations. This is easier in terms of notation and stimulates physical reasoning for the subsequent SGS modelling.

In contrast to implicit filtering one can use a computational grid finer than the width of filter *G* and only retain the largest scales by some (explicit) filtering operation. This explicit filtering is recently being advocated by several authors such as Moin [12] since it considerably reduces numerical discretization errors as the retained motion is always well resolved. This procedure leads to grid independent LES. On the other hand it increases the modelling demands since for the same number of grid points more scales of turbulent motion have to be modelled and it is up to now not fully clear which approach is more advantageous [13].

The filtering approach of Leonard is almost exclusively introduced today in papers on LES and has triggered substantial development, e.g. in subgrid-scale modelling. In practice, however, it is most often used rather as a concept than as a precise algorithmic construction.

2.2 Basics of the Combustion

The intensive development of mathematical combustion theory began in the first half of the twentieth century. It was originally initiated by military objectives. The definition of combustion in terms of macroscopic kinetics is given in [14], one of the pioneering works in this area: "Combustion is the proceeding of a chemical reaction under condition of progressive self-acceleration, which is, in turn, caused by the accumulation in a system either of heat or catalyzing reaction products". The macroscopic theory of combustion deals with investigation of the role of convection, diffusion and heat exchange and their interaction in chemical reaction processes. The elements of chemical kinetics necessary for further considerations are briefly described in section 2.2.1. Generally speaking, single-phase combustion can be subdivided into two major parts. These include non-premixed or diffusion and premixed combustion that are described in the next sections. The less idealized and more commonly occurring in practice partially premixed combustion is considered next.

2.2.1 Chemical kinetics

The chemical kinetics is the study and research of reactions with respect to reaction rates, formed species, formation of new intermediates etc. The points of interest are basically linked to amounts reacted, formed, and the speed of their formation, i.e., the rate at which the concentration of reactants and products change. Consider the following example:

$$\nu_A^{'}A+\nu_B^{'}B \rightarrow \nu_C^{'}C \tag{2.23}$$

Factors $\nu_A^{'}$, $\nu_B^{'}$ and $\nu_C^{'}$ denote the molar stoichiometric coefficients of species *A*, *B* and *C*. The equation (2.23) states that the chemical reaction involves direct conversion from reactant in to product. In reality the chemical reaction can have not only one step, but also few steps, that complicate the chemical kinetics and allow many possible reaction mechanisms. A complete mechanism must also account for all reactants used, and all products formed. The equation (2.23) is then not enough to describe a chemical reaction and a system of equations arise:

$$\sum_{k=1}^{N}\nu_{kj}^{'}M_k \rightleftharpoons \sum_{k=1}^{N}\nu_{kj}^{''}M_k \quad \text{for } j=1,M \tag{2.24}$$

where M_k represents the symbol of species *k*, $\nu_{kj}^{'}$ and $\nu_{kj}^{''}$ are the molar stoichiometric coefficients of species *k* in reaction *j*. The above system of equations must obey the mass conservation given by:

$$\sum_{k=1}^{N}\nu_{kj}^{'}W_k \rightleftharpoons \sum_{k=1}^{N}\nu_{kj}^{''}W_k \quad \text{for } j=1,M \tag{2.25}$$

here W_k denotes the molecular weight of species *k*. However the balanced equation (2.25) does not tell us how the reactants become products. The rate of the overall process will be determined by the slowest (highest energy) step in the reaction mechanism. The mass reaction rate $\dot{\omega}_{kj}$ of species *k* in the reaction *j* is given by:

$$\dot{\omega}_{kj}=r_j W_k \nu_{kj} \quad \text{with} \quad \nu_{kj}=\nu_{kj}^{''}-\nu_{kj}^{'} \tag{2.26}$$

where r_j represents the rate of progress of reaction *j*. By considering all *M* reactions, which take palace within a reaction mechanism, the mass reaction rate $\dot{\omega}_k$ is the sum of all produced rates $\dot{\omega}_{kj}$:

$$\dot{\omega}_k = \sum_{j=1}^{M} \dot{\omega}_{kj} = W_k \sum_{j=1}^{M} r_j \nu_{kj} \tag{2.27}$$

The sum of all mass reaction rates $\dot{\omega}_k$ produced for all species *k* is given by equation (2.28) and obeys the law of mass conservation.

$$\sum_{k=1}^{N} \dot{\omega}_k = \sum_{j=1}^{M} \left(r_j \sum_{k=1}^{N} W_k \nu_{kj} \right) = 0 \tag{2.28}$$

The progress rate r_j of reaction *j*, which denotes the change of products formation in time, can be affected by four factors:

- Concentrations
- Phase of the reactants
- Temperature
- The presence of catalyst

If we plot the concentration of a product forming against time we will get a curve. The tangential slope at any place on that curve would be the instantaneous rate at that moment in time. The reaction rate r_j for a considered reaction j is written [15] as

$$r_j = K_{fj} \prod_{k=1}^{N} \left(\frac{\rho y_k}{W_k} \right)^{\nu'_{kj}} - K_{rj} \prod_{k=1}^{N} \left(\frac{\rho y_k}{W_k} \right)^{\nu''_{kj}} \tag{2.29}$$

where K_{fj} and K_{rj} are the forward and reverse constants of the reaction rates. $\rho y_k / W_k$ is the molar concentration of species *k*. The rate constants are difficult to determine and are related to the temperature of the system by what is known as the Arrhenius equation:

$$K_{fj} = A_{fj} T^{\beta j} \exp\left(-\frac{E_j}{RT} \right) = A_{fj} T^{\beta j} \exp\left(-\frac{T_{aj}}{T} \right) \tag{2.30}$$

where *R* is the ideal gas constant (*8.314 J/mole.K*), *T* is the temperature in Kelvin with the temperature exponent β_j, E_j is the activation energy in joules/mole, T_{aj} is the activation temperature in *K*, and A_{fj} is a constant called the frequency factor; which is related to the fraction of collisions between reactants having the proper orientation. The backwards constant rates K_{rj} are calculated using the equilibrium and the forward rates constants:

$$K_{rj} = \frac{K_{fj}}{\left(\frac{p_a}{RT}\right)^{\sum_{k=1}^{N} \nu_{kj}} \exp\left(\frac{\Delta S_j^0}{R} - \frac{\Delta H_j^0}{RT}\right)} \tag{2.31}$$

where $p_a = 1$ bar. The Δ symbols refer to changes occurring when passing from reactants to products in the j^{th} reaction: ΔH_j^0 and ΔS_j^0 are respectively enthalpy and entropy changes for the reaction *j*. These quantities are obtained from tabulations [15]. The computing of r_j for every reaction necessitate the calculation of forward and backward constants, i.e., the knowledge of all variables: frequency factors A_{fj}, temperature exponents β_j and the activation energy E_j. The huge number of variables and parameters required for the computation of r_j makes the tasks very complex. Using a detailed mechanism in the frame of numerical combustion leads to the resolution of a balance equation for each species included. Consequently it aggravates the tasks for the CFD. In order to use numerical simulation of practical combustion processes, one should use simplified models for the chemical kinetics i.e. the one step reaction mechanism, equilibrium model [16], Flamelet model [17] or ILDM [18]

2.2.2 Governing equations for reacting flows

In a combustion process, many species and chemical reactions are involved. To numerically simulate the combustion process, a system of species transport equations have to be solved in addition to the N–S equations for the flow field. Denote the mass fraction of species *k* with y_k (k = 1,……N), where *N* is the number of species involved, then transport equation for species *k* can be derived as

$$\frac{\partial \rho y_k}{\partial t} + \frac{\partial \rho y_k u_i}{\partial x_i} = \frac{\partial}{\partial x_i}\left(D_k \rho \frac{\partial y_k}{\partial x_i}\right) + \omega_k \tag{2.32}$$

where ω_k is formation rate of species *k*, it is calculated as summation of formation rates from total *M* elementary chemical reactions as explained in the previous section.

In deriving equation (2.32), the diffusive flux in the first term on the r.h.s. is simplified based on Fick's law. The molecular transport process that causes the diffusive flux, however, is very complex. Detailed description can be found in Williams [19].

2.2.3 Non-premixed flame

Diffusion flames represent a specific class of combustion problems. The main feature of these flames is that fuel and oxidizer are not mixed before they enter the domain where they are burnt. Mixing brings reactants into the reaction zone where thin layers of burnable mixtures at different equivalence ratios are formed and combustion takes place. Thus, mixing becomes one of the main issues in this type of flames controlling the behavior of the whole combustion system. Combustion occurs only in a limited region, where fuel and oxidizer are adequately mixed. Outside this region the mixture is either too rich (fuel side) or too lean (oxidizer side) for chemical reactions to proceed. In contrast to premixed flames that are considered in the next section, diffusion flames are not able to propagate against the flow. A definite "thickness" can not be assigned to these flames either. Among industrial applications the diesel engine can be mentioned as a typical example for diffusion flame. Combustion in aero-propulsion devices (aero engines) also takes place in diffusion mode. From the design and safety point of view, diffusion flames are simpler because no premixing with a given equivalence ratio is required and they do not propagate. However, their burning efficiency is restricted compared with premixed flames because the mixing or rather the rate of mixing limits the speed at which chemical reactions may proceed. In modern stationary gas turbines these flames are only employed for the piloting (or stabilization) of the main flame mostly in start-up regimes.

The main disadvantage of pure diffusion flames is that they are less effectible in terms of combustion temperature and, consequently, NO_x emissions. The fuel can be diluted with nitrogen or exhaust gases, but the maximal combustion temperature is always achieved in the region of stoichiometric mixture where the greatest NO_x formation rates take place.

Nevertheless, the fundamental understandings as well as modeling details of diffusion combustion phenomena are very important in context of partially premixed flames that actually appear in stationary gas turbine combustors.

Besides the more complex methods like the flamelet [20], the simplest approach for the modeling of diffusion flames is the well-known mixture fraction [15] description. The transport equation of mixture fraction equation does not have reaction source term. All scalars such as temperature, species concentrations, and density are related to this variable in some way. Bilger [21] and Klimenko [22] proposed a conditional moment closure (CMC) concept for non-premixed turbulent combustion. They observed that most fluctuations of the reactive

scalars can be associated with the fluctuation of the mixture fraction. Unfortunately, this variable is not useful in premixed combustion, since the value of it is constant everywhere.

2.2.4 Premixed flame

Another special class of combustion processes is represented by premixed combustion. Contrary to the diffusion flames considered in the previous section, in premixed flames the fuel and oxidizer are completely mixed on the molecular level before combustion takes place. A schematic representation of an idealized one-dimensional flame is shown in Fig. 2.6. This idealized representation is introduced by Zeldovich and Frank-Kamenetsky (ZFK) (see e.g. [14]) in their asymptotic analysis. One can see the development of the gas temperature T along the only considered axis x from minimal value T_0 (reactants) to maximal value $T_{\max}$ (products) and, consequently, the one-dimensional flame structure. Actually the flame front, if it is considered as an interval where significant temperature changes occur, consists of two main zones:

- Preheating zone where the diffusion of heat and mass proceeds very intensively while chemical reactions are not yet running;
- Reaction zone where, in contrast to the preheating zone, chemical reaction rates rapidly grow up first and then go down so that chemistry dominates against diffusion.

Behind the reaction zone a post flame region (or oxidation zone) is located where no significant heat is released and only some slow (in terms of kinetics) reactions occur at the high temperature achieved in the reaction zone. The fundamental issues of Zeldovich-Frank-Kamenetsky-von-Karman (ZFK) asymptotic theory are as follows:

- The reaction zone is located in the high temperature part of the flame and has a temperature nearly equal to $T_{\max}$;
- The thickness of the reaction zone δ is approximately one order of magnitude smaller than the thickness of the flame front l_f;
- The flame front propagates in the reactants' direction with velocity $\vec{s}$. This velocity is proportional to the square root of the reaction rate (see equation (2.30)) taken at $T = T_{\max}$ and to the thermal diffusivity

$$\left|\vec{s}\right|^2 \sim \frac{\lambda}{\rho c_p}.\exp\left(\frac{E}{RT_{\max}}\right) \tag{2.33}$$

that reveals, consequently, the nature of the flame propagation coupled with the kinetics of the heat release and with heat conduction from the hot to the cold gas layers;

- The maximal combustion temperature $T_{\max}$ is equal to the adiabatic temperature of the chemical reaction that, in turn, can be determined independently on the flame propagation theory from thermodynamic equilibrium.

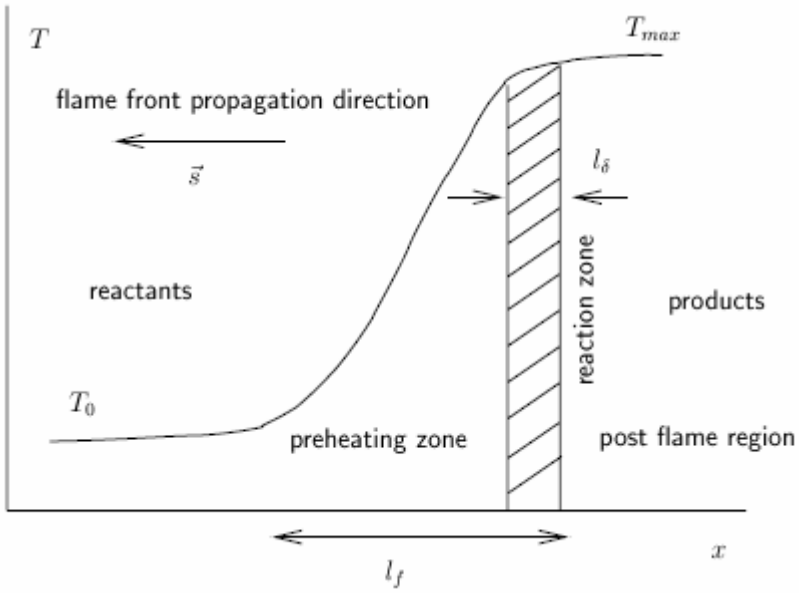

Figure 2.6 Schematic illustration of the structure of laminar and stationary flame

In spite of lots of simplification and assumptions introduced in ZFK asymptotical thermal propagation theory, it helps to understand the fundamental mechanism. Namely that the flame propagation is caused by diffusive processes and the gradients, necessary for diffusion, are sustained by the chemical reaction. This fact is common for all premixed flames independently on the flow regime: laminar or turbulent.

First, it is the laminar burning velocity (called by some authors the laminar flame speed) which is defined as a flow velocity necessary to keep a laminar premixed flame in the steady state (no propagation in reactants' direction). It is also directed normal to the flame front from products (burnt) to reactants (unburnt). The laminar burning velocity can be determined analytically under certain assumptions (ZFK theory [14], Williams [23] etc.). However, these assumptions lead to quantitatively poor results especially for rich flames. More accurate results may be obtained either from one-dimensional computations using detailed chemistry

or from experiments. Actually the laminar burning velocity for a given fuel is only a function of the fuel/oxidizer ratio (equivalence ratio ϕ), pressure and the initial temperature of reactants. The laminar burning velocity decreases with increasing pressure and it increases with increasing temperature of the fresh gases. The variation of the laminar burning velocity with respect to mixture fraction for a methane/air combustion system at pressure $p = 1\ bars$ and fresh mixture temperature $T = 298K$ is shown in Fig. 2.7. The measured values (points) and the fitted curve (line) are presented in Fig. 2.7. Here, the equivalence ratio ϕ is converted into the mixture fraction *z* according to

$$z = \frac{\phi z_{st}}{1 - z_{st}(1-\phi)} \tag{2.34}$$

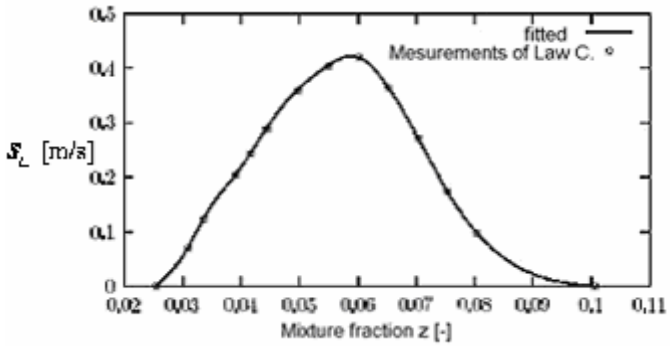

Figure 2.7 Laminar burning velocity for methane/air system at p=bar, T_0=298K

where z_{st} is the stoichiometric mixture fraction value corresponding to the complete consumption of reactants or $\phi = 1$ and calculated for the global reaction (2.23) as

$$z_{st} = \frac{1}{1 + \frac{\nu_O' W_O Y_F}{\nu_F' W_F Y_O}} \tag{2.35}$$

The left and the right boundaries in Fig. 2.7 (mixture fraction values at which $s_L = 0$) correspond to the so called flammability limits. Beyond these limits, the mixture is either too lean or too rich for reactions to proceed.

Another important aspect is that the fuel consumption and the main products formation take place in the narrow reaction zone, but for the pollutant formation, both the reaction zone and the post flame region are important. Due to the fact that the post flame region is significantly larger than the reaction zone and consequently the residence time, which is much longer, the

importance of this region for the "slowly" formed species (e.g. NOx) is even greater than that of the reaction zone.

2.2.5 Partially premixed flame

The non-premixed and premixed regimes of combustion discussed in the previous sections are actually separated in terms of mixing. However, in technical applications, that also include stationary gas turbines, there are very few situations when one of these combustion regimes appears in its pure form. More often a combination of non-premixed and premixed combustion modes takes place featuring the so-called partially premixed combustion phenomenon. The definition of partially premixed combustion given by Peters in [20] is as follows "If the fuel and oxidizer enter separately, but partially mix by turbulence before combustion, the turbulent flame propagates through a stratified mixture. Such a mode of combustion has traditionally been called partially premixed combustion". In partially premixed flames the equivalence ratio ϕ of the fresh gas mixture directly in vicinity of the flame front is still located within the flammability limits but cannot be a priori specified like in perfectly premixed flames because of the additional mixing processes (not mandatory turbulent) appearing before combustion proceeds. Therefore, the equivalence ratio ϕ changes. These changes directly influence the flame propagation process. If the equivalence ratio varies only within the lean region ($z < z_{st}$), the complete fuel consumption occur in the flame front. But if the mixture includes rich values of ϕ then the premixed flame is accompanied by an additional diffusion flame in the post flame region where the remaining fuel oxidizes. This type of flames is called triple flame. An example of a triple flame may be a lifted jet diffusion flame schematically shown in Fig. 2.8. One observes that depending on the nozzle exit velocity, the diffusion flame structure may be destroyed, i.e., at a sufficiently low nozzle exit velocity value a diffusion flame is attached to the nozzle. But increasing the exit velocity leads to stretching and finally disruption of the flame. Consequently, the flame lifts, the reactants mix above the nozzle without reaction to proceed, and a premixed flame stabilizes downstream within the jet. The stabilization appears at those points where the equilibrium between the flow velocity and the burning velocity (that depends on the local mixture) is achieved. In the region with rich (lean) mixture a rich premixed flame is stabilized. The fuel which is not consumed in the rich premixed flame diffuses across the flame into the post flame region and oxidizes building an additional diffusion flame along the stoichiometric mixture surfaces ($z = z_{st}$). Thus, three flame zones can be distinguished at one spatial

location: lean premixed, rich premixed and diffusion flame. The location of the flame stabilization depends on the nozzle exit velocity and is characterized by the lift-off height. The lift-off height increases with increasing jet exit velocity but it can not exceed a critical value at which the flame is completely blown out.

In real gas turbine combustors the situation is even more complicated. The flow is more complex, featuring different recirculation zones and gradients in different directions. The fuel is usually injected into a compact mixing chamber where it is mixed with the oxidizer. It is very important to accurately predict the mixing and flame stabilization processes for the construction of the burner.

Partially premixed flames represent a very nice example of highly complicated phenomena where fluid dynamics mixing and combustion interact strongly influencing each other. Therefore, the importance of their understanding and possible prediction can not be emphasized enough.

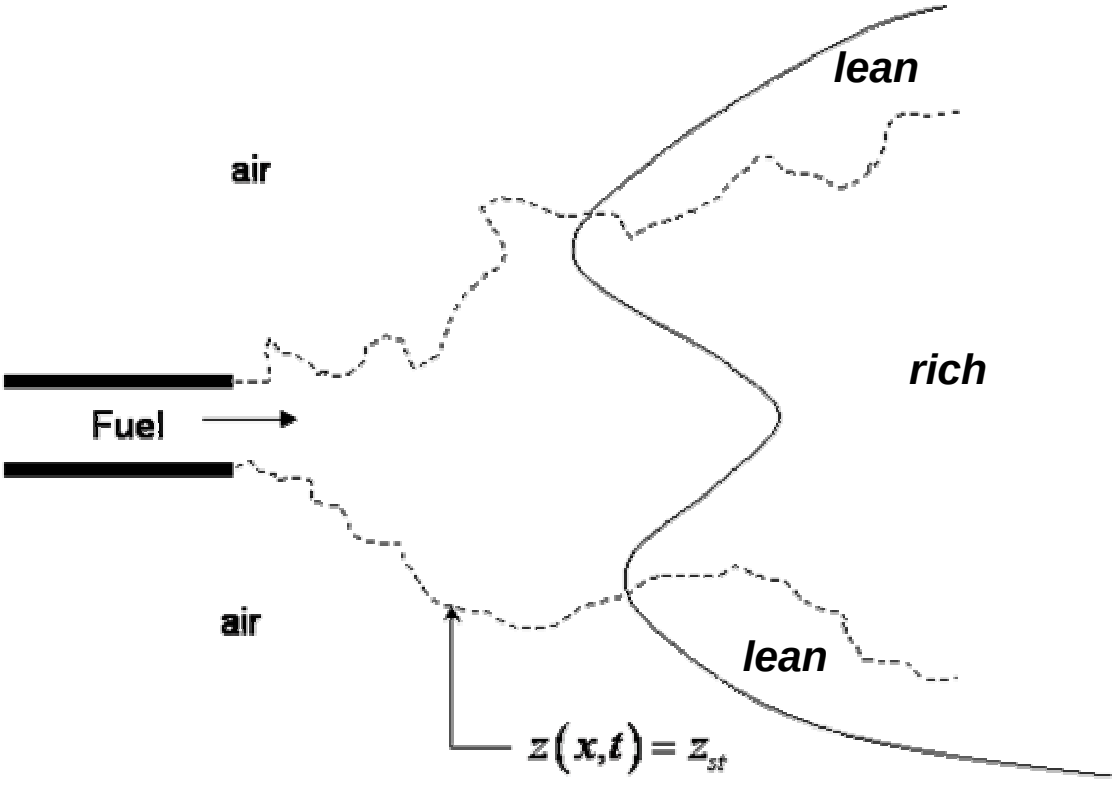

Figure 2.8 *Lifted jet diffusion flame*

Since this work is on premixed combustion, the non-premixed and partially premixed theory put aside and concentrated only on the premixed flames.

2.2.6 Regimes of Turbulent Premixed Combustion

Turbulent premixed reacting flows can be described by a wide range of characteristic time and length scales, spanning several orders of magnitude. The relevant turbulent time and length scales are presented, followed by an overview of the relevant chemical time and length scales for laminar premixed combustion. When these characteristic chemical time and length scales are compared to those of the turbulent flow in a regime diagram, different regimes of premixed turbulent combustion can be identified.

Combustion takes place, in most combustion engines, within a turbulent flow field. Turbulence increases the reactants mixture consumption rate and hence heat releasing rate to much greater values than those of laminar combustion. This is preferable for decrease of the combustion engines size for a given energy output. In turbulent premixed combustion, the unburnt mixture enters into the mean turbulent flame zone in a direction normal to the mean front at a speed much higher than the laminar flame speed S_L. This speed is defined as turbulent flame speed S_T. Fig. 2.9 shows an idealized steady premixed flame in a duct, with two zoom views of the flame at the bottom.

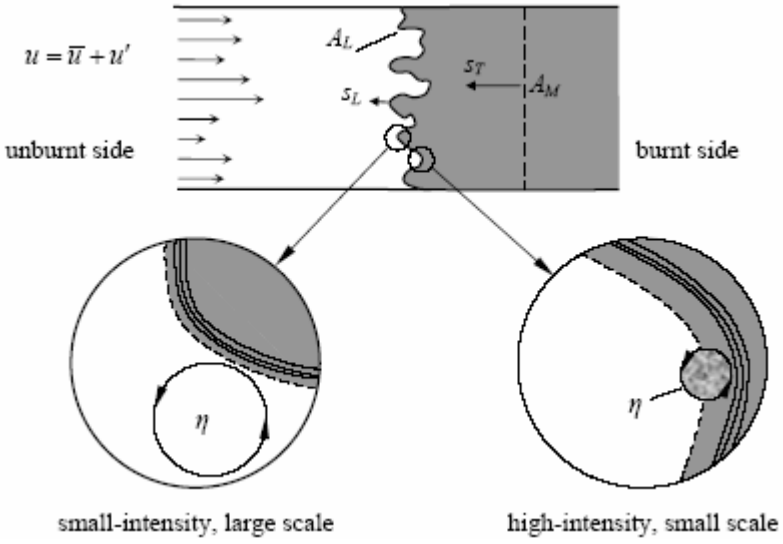

Figure 2.9 A schematic drawing of an idealized steady premixed flame in a duct.

Damköhler [24] was the first one to analyze the early experimental data for turbulent burning velocity S_T. In his work, he specified two different regimes of turbulent premixed combustion: the small-intensity, large scale turbulence and the high intensity, small scale turbulence. For small-intensity, large scale turbulence, Damköhler proposed that

$$\frac{S_T}{S_L} = \frac{A_L}{A_M} \tag{2.36}$$

where A_L is the total laminar flame front area, A_M is the mean turbulent flame area, as shown in Fig. 2.9. Further, Damköhler proposed that the area ratio on the r.h.s. of equation (2.36) is proportional to $1 + u'/S_L$; thus, the turbulent flame speed can be expressed as

$$S_T \sim S_L + u' \tag{2.37}$$

For high-intensity, small scale turbulence, Damköhler assumed that turbulence only modifies the transport between the reaction zone and the unburnt zone with an enhanced equivalent diffusivity to replace the molecular kinematic viscosity. From the scaling relation for the laminar flame speed

$$S_L \sim \left(\nu / t_F\right)^{1/2} \tag{2.38}$$

The turbulent flame speed is estimated with

$$S_T \sim \left(\nu_t / t_F\right)^{1/2} \tag{2.39}$$

Here, ν and ν_t are the molecular and turbulent kinematic viscosity, respectively. From equations (2.38) and (2.39), a relation between S_T and S_L is obtained as

$$\frac{S_T}{S_L} \sim \left(\frac{\nu_t}{\nu}\right)^{1/2} \tag{2.40}$$

Peters [20] identified the small-intensity, large scale and the high-intensity, small scale turbulence, with the corrugated flamelets regime and thin reaction zone regime (see Fig. 2.10), respectively. The two zoom views in Fig. 2.9 are schematic plotting of these two regimes. For small-intensity turbulence (left of bottom zoom view), the Kolmogorov scale is larger than the flame thickness, and the interaction between the flame front and the turbulence field is purely kinematic, i.e. turbulence can wrinkle the flame but can not disturb its local structure. For high-intensity turbulence (right of bottom zoom view), the Kolmogorov eddy scale is smaller than the preheat zone; hence, it can enter into the preheat zone, and enhances the transport of radicals and heat between the reaction zone and the unburnt gas.

A large number of experiments for measuring the turbulent flame speed have been conducted with different combustion configurations, such as the Bunsen flame, counter-flow flame, swirling flame and so on. Review articles on the turbulent flame speed are available in the

literature, e.g. [25]. It is found that, at low turbulence intensity, the turbulent flame speed increase almost linearly with the turbulence level. If the turbulence levels are higher than some critical value, the turbulent flame speed, however, only increases slightly, and even quenching of the combustion may happen. This effect is known as turbulent flame speed bending in combustion literature [25]. In order to distinguish the influence of different turbulence levels on the turbulent combustion, it is useful to classify the turbulent combustion into different regimes. To do this, a few dimensionless parameters are first introduced.

To simplify the analysis, it is common to assume equal diffusivities for all reactive scalars and the Schmidt number *Sc*, Lewis number *Le* and Prandtl number *Pr* unity.

$$Le = \frac{\alpha}{D} = 1, \quad Pr = \frac{\nu}{\alpha} = 1, \quad Sc = \frac{\nu}{D} = 1 \tag{2.41}$$

where ν, α and *D* are the momentum, thermal and mass diffusivity, respectively. In addition to this, relations for the laminar flame thickness l_F, reaction time scale t_F and laminar flame speed S_L are assumed based on the order analysis.

$$l_F = \frac{D}{S_L}, \qquad t_F = \frac{l_F}{S_L} = \frac{D}{S_L^2} \tag{2.42}$$

Then, the turbulent Reynolds number Re_l is expressed in terms of the turbulent fluctuation u' and turbulent integral length scale l_t as

$$Re_l = \frac{u' l_t}{\nu} = \frac{u' l_t}{S_L l_F} \tag{2.43}$$

The Damköhler number *Da*, the ratio of turbulent integral time scale T_t to the reaction time scale t_F, is expressed as

$$Da = \frac{T_t}{t_F} = \frac{l}{u'} \frac{S_L}{l_F} \tag{2.44}$$

The Karlovitz number compares the reaction time scale t_F to the Kolmogorov time scale t_k

$$Ka = \frac{t_F}{t_k} = \frac{l_F^2}{\eta^2} \tag{2.45}$$

It is easy to derive a relation from equations (2.43) and (2.45) as

$$Re_l = Da^2 Ka^2 \tag{2.46}$$

Figure 2.10 shows a turbulent premixed combustion regime diagram in terms of length and velocity scale ratios in the log–log scale. This diagram is similar to those of Peters [20], Borghi [26] and it categorizes the turbulent premixed combustion into five regimes. The *laminar flames regime* is located in the lower-left corner, which is separated from all turbulent flame regimes by line Re_l =1. In *wrinkled flamelets regime*, the large eddies turnover velocity u' is less than the laminar flame speed, which does not exist in most of the practical applications.

In Figure 2.10, the line *Ka*=1 is called the Klimov–Williams criterion. Below this line, the flame thickness l_F is thinner than the Kolmogorov length scale. The turbulence eddies can only wrinkle the flame front and not able to disturb the reactive-diffusive laminar flame structure. This regime ($Ka<1 \text{and} u'/S_L>1$) is called the *corrugated flamelets regime*, in which the flame front generally remains quasi-laminar.

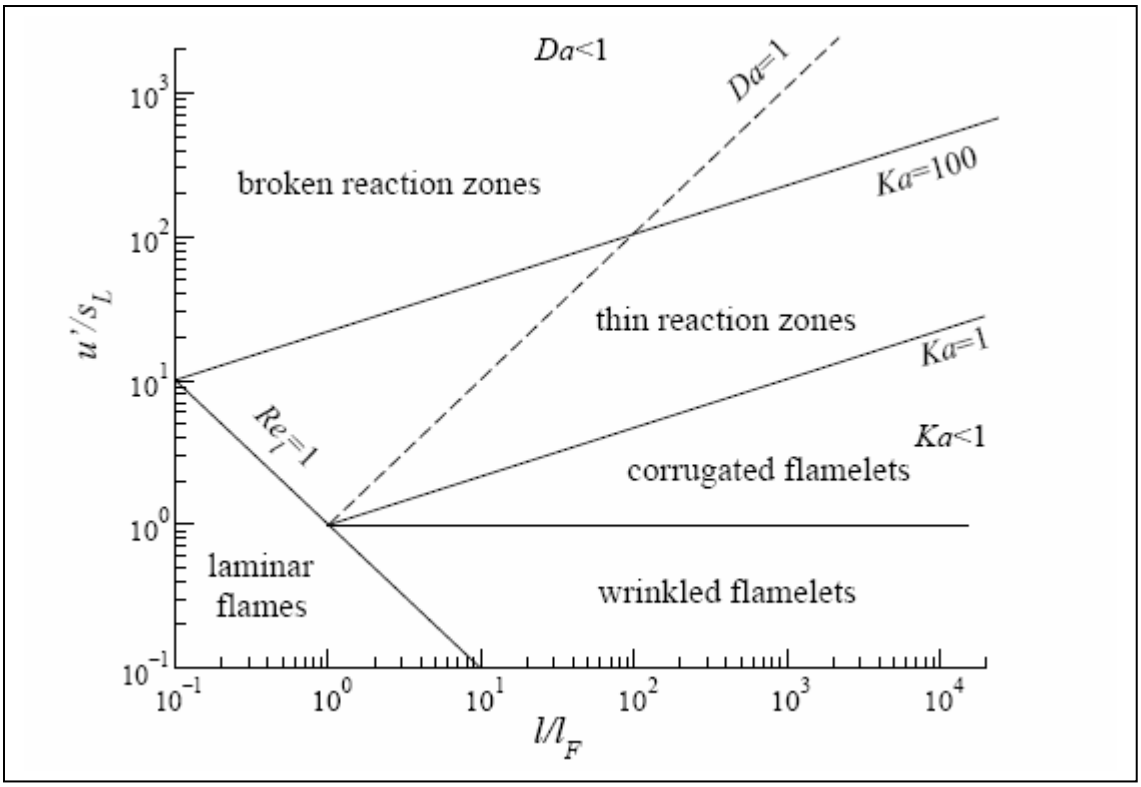

Figure 2.10 A regime diagram for premixed turbulent combustion

The line *Ka*=100 is corresponding to the situation that the Kolmogorov length scale is equal to the inner layer thickness, which assumes the inner layer thickness is one tenth of the flame thickness l_F. The regime characterized by 1<*Ka*<100 and $Re_l > 1$ is called the *thin reaction*

zones. Peters [20] argued that in this regime, the Kolmogorov eddies can enter into the preheat zone but can not penetrate into the inner layer, since $l_\delta < \eta < l_F$ where l_δ denotes the thickness of inner layer. Due to this, this regime is also called '*thickened-wrinkled flame*' [15]. Above the line *Ka*=100, it is called *broken reaction zones*, in which both the preheat zone and inner layer are disturbed by the turbulence eddies, and thin flame could no longer be identified.

Fig. 2.10 also shows the line *Da*=1, above which the turbulent mixing time is shorter than the reaction time, hence the overall reaction rate is limited by chemistry. This regime (*Da*<1) is often called the '*well-stirred reactor*'. In practical combustion engines, this regime is generally difficult to access, since complete fast mixing without quenching is almost impossible to achieve [3]. In theory analysis, however, it is useful, for example, it estimates the maximum overall energy release rate in a fixed volume.

2.2.7 Turbulent Premixed Combustion Models

The system of reacting Navier-Stokes equations together with equation (2.32), describes the underlying physics and chemistry of turbulent premixed combustion completely. However, the time scales of the chemical reaction rates are generally significantly smaller than the smallest turbulent time scales, thus leading to a very stiff system of coupled, non-linear differential equations. As compared to DNS calculations of non-reacting turbulent flows, the computational effort is drastically increased, exceeding the computational resources available today and in the foreseeable future by far. Hence, only very limited, isolated turbulent premixed combustion problems are solved by employing reduced mechanisms using reacting DNS. Again, the computational effort can be reduced to acceptable levels if the averaged reacting Navier-Stokes equations are solved instead of the instantaneous ones. Unfortunately, the averaging of the reacting Navier-Stokes equations produces unclosed terms that require modeling. In this section only overview of Reynolds averaging modelling techniques are presented. Detailed discussion of Large eddy simulations of premixed combustion are presented in the chapter 4.

In RANS modelling of reactive flows the Reynolds stress terms and the turbulent transport terms for non-reacting scalars are closed within the scope of turbulence models. The unclosed turbulent transport terms for reacting scalars and, above all, the mean chemical source terms, $\overline{\omega}_k$, have to be closed by appropriate turbulent combustion models. In the case of premixed turbulent combustion, the prevailing models in literature can be classified according to their underlying modelling assumptions into three main groups: turbulence controlled models [27], PDF models [15], and flamelet models [20] as shown in Fig. 2.11.

	Infinitely fast chemistry	Finite rate chemistry
Turbulence controlled models	Eddy-Break-Up model Eddy-Dissipation model	
PDF models		PDF transport equations
Flamelet models	Bray-Moss-Libby Coherent Flame Model	level set

Figure 2.11 *Overview of turbulent premixed combustion models*

Chapter 3

SGS modeling in LES

In this chapter, subgrid scale (SGS) modeling of large eddy simulation is presented. In the first part, necessary properties of the SGS modeling are discussed. In the second part different SGS models, which are used in the present work are discussed in detail. Finally in the last part further possibilities of the SGS modeling are presented.

3.1 Ideal SGS modeling

3.1.1 Dependence of the SGS model on energy in subgrid -scales

- In low Reynolds number flow cases, where $k_{SGS}/k \leq 30\%$, results are relatively insensitive to the type of SGS model used. However results can be very sensitive to the numerics if artificial dissipation is present (e.g., convective terms are discretized by using upwind schemes). Nevertheless with the use of coarse grids the importance of the SGS models increases even in the low Reynolds number cases.
- In high Reynolds number flow cases, where $k_{SGS}/k > 30\%$, SGS model play a very important role. In these cases a better model gives better results.

3.1.2 Requirements that a good SGS model must fulfil

- A good SGS model must represent interaction between large and small scales. This property is very important especially in the case of high Reynolds number flows.
- The most important feature of a SGS model is to provide adequate dissipation, which means proper transport of energy from the resolved grid scales to the unresolved grid scales. Especially in energy conserving codes (ideal for LES) the only way for turbulent kinetic energy to leave the resolved modes is by the dissipation provided by the SGS model.
- The dissipation rate must depend on the large scales of the flow rather than being imposed arbitrarily by the model. In other words a SGS model must depend on the large-scales statistics and must be sufficiently flexible to adjust to the changes in these statistics.

- Ability to capture backscatter, i.e., the reintroduction of the energy from the small eddies to large eddies.
- A good SGS model must not introduce noise. This property is very important in compressible flow simulations.

3.2 Implemented SGS models

In this section different SGS models, which are implemented in this work are presented and discussed in detail.

3.2.1 Linear Eddy viscosity models

The eddy viscosity approach is based on the assumption that small scale turbulence affects the flow in the same way as the molecular viscosity. Therefore, the fine structure term τ_{ij} (see equation (2.22)) may be modeled by adding a turbulent viscosity ν_t to the molecular viscosity ν, resulting in an effective viscosity $\nu_{eff} = \nu_t + \nu$.

By using the turbulent viscosity ν_t, the deviatoric part of the SGS stress in the filtered incompressible Navier-Stokes equation can be approximated as

$$\tau_{ij}^d = \tau_{ij} - \frac{1}{3}\tau_{kk}\delta_{ij} = -2\nu_t \bar{S}_{ij} = -\nu_t\left(\frac{\partial \bar{u}_j}{\partial x_i} + \frac{\partial \bar{u}_i}{\partial x_j}\right) \qquad where \quad \bar{S}_{ij} = \frac{1}{2}\left(\frac{\partial \bar{u}_j}{\partial x_i} + \frac{\partial \bar{u}_i}{\partial x_j}\right) \tag{3.1}$$

Dimensionally eddy viscosity is represented as l^2t^{-1} and SGS eddy viscosity can be expressed in terms of velocity scale (q) and length scale (l) as follows

$$\nu_t = Cql \tag{3.2}$$

Unlike RANS, in LES the length scale l can be easily defined as the largest size of unresolved scales which is approximately equal to the filter width $\bar{\Delta}$, which is coherent with the idea that only the unresolved structures are to be modeled. But defining the velocity scale is quite difficult in LES compared to RANS. Based on the definition of the velocity scale there are two very popular eddy viscosity models. One is the Smagorinsky model [28] and the other one is based on the SGS kinetic energy [29].

3.2.1.1 Smagorinsky model

In this model the velocity scale q is expressed as the variation of velocity over one grid element (1d case).

$$q = l\frac{\partial \overline{u}}{\partial x} = l\overline{S} \tag{3.3}$$

where $\overline{S}$ is the filtered rate-of-strain.

Better choice for the 3d flows is $\overline{S} = \left(2\overline{S}_{ij}\overline{S}_{ij}\right)^{1/2}$ and using this velocity scale one can get

$$\nu_t = C\overline{\Delta}^2\overline{S} = C_S^2\overline{\Delta}^2\left(2\overline{S}_{ij}\overline{S}_{ij}\right)^{1/2} \tag{3.4}$$

where C_S is the model parameter. This model was basically designed for the global weather modelling. Nevertheless it predicts many flows reasonably well. Model constant value varies with flow type from 0.065 to 0.25, for e.g., isotropic turbulence case it is 0.2 [30], for channel flows it is 0.1[31].

Defining the length scale is uncertain with anisotropic grids for this model. There are two possibilities to calculate the filter width:

$$\overline{\Delta} = \left(\Delta_1\Delta_2\Delta_3\right)^{1/3} \tag{3.5}$$

$$\text{and } \overline{\Delta} = (\Delta_1^2 + \Delta_2^2 + \Delta_3^2)^{1/2} \tag{3.6}$$

where Δ_1, Δ_2 and Δ_3 represent grid dimensions in x, y and z dimensions. Usage of the filter size given by the formulation from equation (3.5) is problematic for the pencil type grids. To rectify this problem one must use formulation given by Scotti et. al. [32], which is based on an improved estimation of dissipation rate in the anisotropic grid case. In this formulation filter is assumed to be anisotropic but homogeneous, i.e., the cut-off length is constant in each direction of space. Length scale in this case is given by the

$$\overline{\Delta} = \left(\Delta_1\Delta_2\Delta_3\right)^{1/3} f(a_1, a_2) \tag{3.7}$$

where $$f\left(a_1, a_2\right) = \cosh\sqrt{\frac{4}{27}\left[\left(\ln a_1\right)^2 - \ln a_1 \ln a_2 + \left(\ln a_2\right)^2\right]} \tag{3.8}$$

In the above equation (3.8) a_1, a_2 represent the aspect ratios of a grid and given by the $a_1 = \Delta_2/\Delta_1$ and $a_2 = \Delta_3/\Delta_1$ with the assumption of $\Delta_{\max} = \Delta_1$.

This Smagorinsky model cannot predict the backscatter. Model constant requires a proper modification to account for complex phenomena's like rotation, stratification etc. On the other hand, in the vicinity of a wall, C_S should be reduced. This can be achieved with the damping function proposed by van Driest [33]. However, van Driest damping is not possible in complex configurations. A truly desirable approach is to calculate automatically the model parameter for each location of the flow field, as in the dynamic procedure (see section 3.2.2). As it can be seen from equation (3.1) Smagorinsky model basically assumes that the principal axes of the SGS stress tensor are aligned with those of the resolved strain rate tensor, a result which is not supported by the direct numerical simulation data [34].

3.2.1.2 Models based on SGS kinetic energy

The Smagorinsky model does not contain any information regarding the total amount of energy in the subgrid scales, k_{sgs}. Therefore, if the model coefficient becomes negative in any part of the domain, the model does not have any information on the available energy in the subgrid scales and is therefore unable to provide a mechanism to saturate the reverse flow of energy. A model that keeps the track of SGS kinetic energy will address this problem. Expressing the velocity scale $q = \sqrt{k_{sgs}}$ and based on the dimensional analysis linear eddy viscosity is given as

$$\nu_t = C_d \overline{\Delta} \sqrt{k_{sgs}} \tag{3.9}$$

where C_d represents model parameter. In this approach we have to solve the partial differential equation for the SGS kinetic energy $k_{sgs.}$ So these models are called one equation models.

The model coefficient can still have either sign, but it was observed that numerical computations using this kind of models are much more stable when the coefficient is negative. In other words, these models can account for relatively large amounts of backscatter in a numerically stable way. The energy flows back and forth between the resolved and subgrid scales while their sum decays monotonically due to the viscous effects in the absence of external input of energy.

Typically, the equation for k_{sgs} is similar to the one used in RANS models, but the form of the dissipation term is different. In the original model of Yoshizawa [29] the following equation was used:

$$\frac{\partial k_{sgs}}{\partial t} + \left(\overline{u}_j k_{sgs}\right)_{,j} = \left(\left(\upsilon_t + \upsilon_l\right)\left(k_{sgs}\right)_{,j}\right)_{,j} - \tau_{ij}\overline{S}_{ij} - C_\varepsilon \frac{k_{sgs}^{3/2}}{\overline{\Delta}} \tag{3.10}$$

where C_d =0.07 and C_ε =1.05. In the equation (3.10) on the RHS, first term represents diffusion term, second term represents production and the last term represents dissipation.

3.2.2 Dynamic SGS models

From the previous sections it is apparent that for physical reasons one would prefer to replace the model constant values C_S, C_d and C_ε by a value changing in space and time. The dynamic procedure has been developed by Germano et al [35], in order to determine such a value from the information provided by the resolved scales, in particular the ones close to the cutoff scale. The basic idea of this dynamic procedure is to calculate the model parameter from the smallest resolved scales. In this procedure the chosen model is applied not only on the grid scale or filter scale $\overline{\Delta}$, but also on a coarser scale $\tilde{\Delta}$ as illustrated in the Fig. 3.1. This is the so called test scale filter with, e.g., $\tilde{\Delta} = 2\overline{\Delta}$

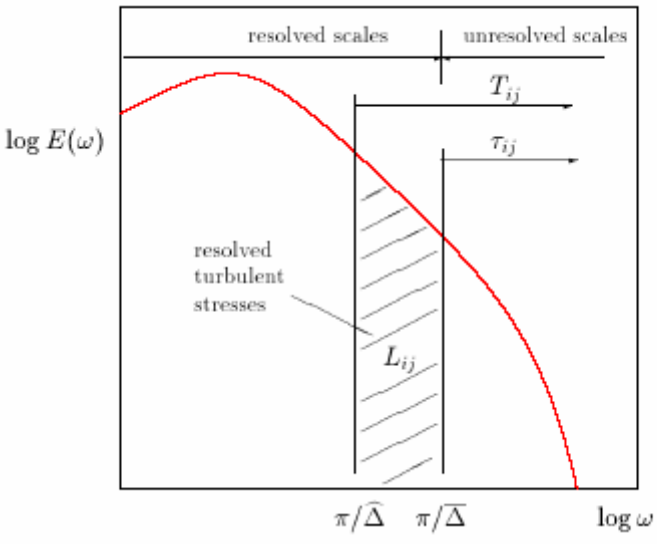

Figure 3.1 *Illustration of the dynamic modelling idea*

Subgrid scale stresses at $\overline{\Delta}$-level is given by

$$\tau_{ij} = \overline{u_i u_j} - \overline{u_i}\,\overline{u_j} \approx f(C, \overline{\Delta}, \overline{u_i}, ...) \tag{3.11}$$

Subgrid scale stresses at $\tilde{\Delta}$-level is given by

$$T_{ij} = \widetilde{\widetilde{u_i u_j}} - \widetilde{\widetilde{u_i}}\,\widetilde{\widetilde{u_j}} \approx f(C, \tilde{\Delta}, \widetilde{u_i}, ...) \tag{3.12}$$

From the known resolved velocities u_i the velocities $\widetilde{u_i}$ are computed by applying the proper filter for example box filter or Gaussian filter. Similarly, the term $L_{ij} = \widetilde{\overline{u_i}\overline{u_j}} - \widetilde{\overline{u_i}}\,\widetilde{\overline{u_j}}$ can be evaluated by using these filters. It is this part of the subtest stresses T_{ij} which is resolved on the grid $\overline{\Delta}$ as sketched in Fig. 3.1. The total stresses $\overline{u_i u_j}$ in the expression for T_{ij} can be decomposed into the contribution $\overline{u_i}\,\overline{u_j}$ resolved on the grid $\overline{\Delta}$ and the reminder τ_{ij}. Inserting this in to equation (3.12) gives

$$T_{ij} = L_{ij} + \widetilde{\tau_{ij}} \tag{3.13}$$

known as Germano's identity [35]. Hence, on one hand L_{ij} can be computed, on the other hand the SGS model yields a model expression when inserting equations (3.11), (3.12) in (3.13):

$$L_{ij}^{app} = f(C, \tilde{\Delta}, \widetilde{u_i}, ...) - \widetilde{f(C, \overline{\Delta}, \overline{u_i}, ...)} \tag{3.14}$$

Ideally C would be chosen such that residual E_{ij} becomes "0".

$$E_{ij} = L_{ij} - L_{ij}^{app} = 0 \tag{3.15}$$

But this is a tensor equation and can only be fulfilled in some average sense, minimizing e.g. the root mean square of the left hand side as proposed by Lilly [36].

3.2.2.1 Dynamic Smagorinsky model (DSM)

By applying the dynamic procedure to Smagorinsky model one can get the following expression by using equation (3.14)

$$L_{ij}^{app} = -2C\tilde{\Delta}^2 \left|\widetilde{S}\right| \widetilde{S_{ij}} + \widetilde{2C\overline{\Delta}^2 \left|\overline{S}\right| \overline{S_{ij}}} \tag{3.16}$$

with $C = C_S^2$ for convenience. Classically, the model is developed by extracting *C* from the filtered expression in the second term, assuming scale invariance, although in fact *C* can vary in space. The right hand side of equation (3.16) can then be written as $2CM_{ij}$ so that inserting it into equation (3.15) with the least-squares minimization mentioned above yields

$$C = \frac{L_{ij} M_{ij}}{2 M_{ij} M_{ij}} \tag{3.17}$$

where $$M_{ij} = -C\widetilde{\Delta}^2 \left|\widetilde{S}\right| \widetilde{S_{ij}} + \widetilde{C\overline{\Delta}^2 \left|\overline{S}\right| \overline{S_{ij}}} = -C\widetilde{\Delta}^2 \left|\widetilde{S}\right| \widetilde{S_{ij}} + \widetilde{C\overline{\Delta}^2 \left|\overline{S}\right| \overline{S_{ij}}} \tag{3.18}$$

with $\widetilde{C} = C$. Now onwards this model is referred as Germano-Lilly dynamic Smagorinsky model.

The advantage of equation (3.17) is that now the model parameter of the Smagorinsky model is no longer required from the user but is determined by the model itself. In fact, it is automatically reduced close to walls and vanishes for well resolved laminar flows. Negative values of *C* are possible and are interpreted by some authors as a way to model backscatter. In fact the resulting "backward diffusion" can however generate numerical instability so that often the condition or the clipping $\nu + \nu_t \geq 0$ is imposed. Furthermore, *C* determined by equation (3.17) as it is, exhibits very large oscillations which generally need to be regularized in some way. Most often nominator and denominator are averaged in spatially homogeneous directions space before being used. However, this requires the flow to have at least one homogeneous direction. Another way is to relax the value in time.

A further important observation based on results from numerical simulations of various flows is that the model coefficient has large variations in fairly small regions of the flow. For instance, in simulations of (decay of) isotropic turbulence:

$$\left\langle C_d^2 \right\rangle - \left\langle C_d \right\rangle^2 \approx 10 \left\langle C_d \right\rangle^2 \tag{3.19}$$

which suggests that the removal of *C* from the filter in equation (3.18) was not justified.

Advantages of dynamic Smagorinsky model:

- This model is self-contained, means no need to specify model parameter.

- Eliminates need to prescribe proper length scale means no need to choose formula for Δ with anisotropic grid. Dynamic method actually computes ν_t rather than C means if Δ is changed then C changes to compensate the resultant turbulent viscosity.
- No need to modify for 'extra strains' like stratification, rotation effects automatically included.
- This model can predict zero eddy viscosity in laminar regions of the flow.
- When it works well, it is self-compensating means if there is too much energy in smallest resolved scales then dynamic model will increase eddy viscosity. This implies reduction of energy in small scales later. On the other hand it behaves exactly opposite if energy is too small.

Disadvantages of dynamic Smagorinsky model:

- Model parameter variation is too large, means variance is too large (equation (3.19))
- Produces large negative values of ν_t. Unfortunately this behaviour stays for long time, and results in numerical instability.
- Assumption of a scale-invariant coefficient C in equation (3.18) is incorrect means C should not be removed from the filter.
- This model depends too much on smallest scales, which results in noise generation.

3.2.2.2 Localized dynamic smagorinsky model

There are several ways to improve the deficiencies of the dynamic Smagorinsky model, especially for non-homogeneous flows when averaging in one or two directions that would reduce the sharp fluctuations in the values of the model coefficient is not possible. A very consistent approach is the *dynamic localization model* of Ghosal et al.[37] in which an integral equation is solved to determine the model coefficient. There is no need to average expressions locally or in the homogeneous directions but an integral formulation of the identity equation (3.13) or (3.16) is used. This identity rigorously removes the mathematical inconsistency, i.e. the assumption of $\widetilde{2C\overline{\Delta}^2\left|\overline{S}\right|\overline{S_{ij}}}$ is equal to $2C\widetilde{\overline{\Delta}^2\left|\overline{S}\right|\overline{S_{ij}}}$, at the expense of solving an integral equation at each time step (this is computationally quite expensive, comparable to the solution of a Poisson equation). The integral equation is obtained by minimizing a functional (in this case the integral of the error, see equation (3.15), over the

entire domain). If no additional constraints are imposed on *C*, the integral equation is linear. If the additional constraint that *C*>0 is imposed everywhere in the flow the integral equation is nonlinear, thus more expensive to solve.

Several simpler variants exist that reduce the computational overhead related to solving exactly the integral equation, but then one cannot mathematically guarantee that C>0. Piomelli and Liu [38] proposed that instead of solving directly the integral equation for C, one can try to solve it iteratively.

By recasting the equation (3.16) one can get the following form

$$L_{ij}^{app} = -2C\widetilde{\Delta}^2 \left|\widetilde{S}\right| \widetilde{S_{ij}} + \widetilde{2C^*\overline{\Delta}^2 \left|\overline{S}\right| \overline{S_{ij}}} \tag{3.20}$$

by assuming $\alpha_{ij} = -2\widetilde{\Delta}^2 \left|\widetilde{S}\right| \widetilde{S_{ij}}$ and $\beta_{ij} = -2\overline{\Delta}^2 \left|\overline{S}\right| \overline{S_{ij}}$, above equation can be expressed as

$$L_{ij}^{app} = C\alpha_{ij} - \widetilde{C^*\beta_{ij}} \tag{3.21}$$

$$C = \frac{\alpha_{ij}\left(L_{ij}^{app} + \widetilde{C^*\beta_{ij}}\right)}{\alpha_{ij}\alpha_{ij}} \tag{3.22}$$

$$C^* = C^{(n-1)} + \Delta t \left.\frac{\partial C}{\partial t}\right|^{(n-1)} + \text{.....} \tag{3.23}$$

where the superscript (n-1) is related to the value of the variable at the (n-1)th time step, and Δt is the value of the time step. For simplicity one can use $C^* = C^{(n-1)}$. The resulting procedure is fully local, and does not induce large extra computational effort as the original localized procedure does. Nevertheless the proposed method requires clipping to yield a well-behaved algorithm.

3.2.2.3The Dynamic Lagrangian SGS Model:

This approach proposed by Meneveau et al. [39] for non-homogeneous flows is to use Lagrangian averaging, meaning to take the average over a path line (back in time).

The Lagrangian averaging <> is here defined as:

$$I_f = \langle f \rangle = \int_{-\infty}^{t} f(t')W(t-t')dt' \tag{3.24}$$

$$C = \frac{\langle L_{ij}M_{ij} \rangle}{2\langle M_{ij}M_{ij} \rangle} = \frac{I_{LM}^n}{2I_{MM}^n} \tag{3.25}$$

The idea behind using Lagrangian averaging in the formula for the model coefficient is based on the consideration that memory effects should be calculated in a Lagrangian framework, following the fluid particle, rather than in an Eulerian framework, which sees different particles, with different histories, at each instant. Thus the integral in equation (3.24) is carried out following a fluid path-line, *W(t)* is an exponential weighting function chosen to give more weight to recent times, *n* denotes the time step and, using equation (3.24):

$$I_{LM} = \int_{-\infty}^{t} L_{ij}(t')M_{ij}(t')W(t-t')\,dt' \tag{3.26}$$

$$I_{MM} = \int_{-\infty}^{t} M_{ij}(t')M_{ij}(t')W(t-t')\,dt' \tag{3.27}$$

To simplify the numerical implementation (where it is not computationally efficient to integrate to far back in time) one can choose the weight function:

$$W(t) = 1/T \cdot \exp(-t/T) \tag{3.28}$$

with the time constant (T) defined as:

$$T = 1.5\Delta \cdot \left(-8I_{LM}^n I_{MM}^n\right)^{-1/8} \tag{3.29}$$

in which case one can show that the integrals from equation (3.26) and (3.27) can be approximated by:

$$I_{LM}^n(\vec{x}) = H\left\{\varepsilon L_{ij}^n M_{ij}^n + (1-\varepsilon) I_{LM}^{n-1}(\vec{x} - \vec{u}^n \Delta t)\right\} \tag{3.30}$$

$$I_{MM}^n(\vec{x}) = H\left\{\varepsilon M_{ij}^n M_{ij}^n + (1-\varepsilon) I_{MM}^{n-1}(\vec{x} - \vec{u}^n \Delta t)\right\} \tag{3.31}$$

where H is the ramp function, the coefficient ε is defined as:

$$\varepsilon = \frac{\Delta t/T}{1+\Delta t/T} \tag{3.32}$$

So that the evaluation of the integrals from equation (3.30) and (3.31) at $x - u^n \Delta t$ can be performed by linear interpolation. In order to avoid complex values for T (see equation (3.29)), if $C(\vec{x},t) = 0$ is reached, I_{LM}^n is set to zero. Nevertheless an extra parameter T that characterizes the averaging time was introduced. Ideally the averaging time should depend on the local time scale.

It was found that this way of estimating the model coefficient reduced the fraction of the points where the model will predict negative values and reduces the variability in the dynamic coefficient values with the effect of finally improving the robustness of the numerical simulation.

3.2.2.4 Dynamic one equation model based on SGS kinetic energy

This model has been proposed by Davidson group [40]. The modelled transport equation for the subgrid kinetic energy (k_{sgs}) is given by below equation:

$$\frac{\partial k_{sgs}}{\partial t} + \underbrace{\left(\overline{u}_j k_{sgs}\right)_{,j}}_{C_{sgs}} = \underbrace{\left(\left(\left\langle C\right\rangle_{xyz} \Delta \overline{k_{sgs}^{\frac{1}{2}}} + \nu\right)\left(k_{sgs}\right)_{,j}\right)_{,j}}_{D_{sgs}} + \underbrace{2\nu_{sgs}\overline{S}_{ij}\overline{S}_{ij}}_{P_{sgs}} - \underbrace{C_\varepsilon \frac{\overline{k_{sgs}^{\frac{3}{2}}}}{\Delta}}_{\varepsilon_{sgs}} \tag{3.33}$$

The production term P_{sgs} is given by the

$$P_{sgs} = 2\nu_{sgs}\overline{S}_{ij}\overline{S}_{ij} = -2C\Delta \overline{k_{sgs}^{\frac{1}{2}}}\overline{S}_{ij}\overline{S}_{ij}$$

The dynamic coefficient C in the production term is computed in a similar way as in the standard dynamic model, i.e.,

$$C = \frac{L_{ij}M_{ij}}{M_{ij}M_{ij}} \tag{3.34}$$

where $$L_{ij} = \widetilde{\overline{u}_i\overline{u}_j} - \widetilde{\overline{u}}_i\widetilde{\overline{u}}_j \;;\; M_{ij} = -2\widetilde{\Delta}\widetilde{K^{\frac{1}{2}}\overline{S}_{ij}} + \widetilde{2\Delta \overline{k_{sgs}^{\frac{1}{2}}}\overline{S}_{ij}}, K = \widetilde{k_{sgs}} + \frac{1}{2}L_{ii} \tag{3.35}$$

Here L_{ij} denotes the dynamic Leonard stresses, and $K = T_{ii}/2$ is the subgrid kinetic energy on the test level. The dissipation term ε_{sgs} is given by:

$$\varepsilon_{sgs} = C_\varepsilon \frac{\overline{k_{sgs}^{3/2}}}{\Delta} \tag{3.36}$$

In order to estimate C_ε in equation (3.33 or 3.36) let us consider the equations for the *K* and k_{sgs}. They are given in symbolic form by:

$$C_{ksgs} - D_{ksgs} = P_{ksgs} - C_\varepsilon \frac{k_{sgs}^{3/2}}{\Delta} \tag{3.37}$$

and analogously:

$$C_K - D_K = P_K - C_\varepsilon \frac{K^{3/2}}{\tilde{\Delta}} \tag{3.38}$$

By applying test filter to the equation (3.37) one can assume that the transport of k_{sgs} is proportional to that of K with the constant of proportionality $\tilde{k}_{sgs}/K$, equation (3.37) and (3.38) give

$$\widetilde{P_{ksgs}} - \widetilde{C_\varepsilon \frac{k_{sgs}^{3/2}}{\Delta}} = \frac{\widetilde{k_{sgs}}}{K}\left(P_K - C_\varepsilon \frac{K^{3/2}}{\tilde{\Delta}} \right) \tag{3.39}$$

$$C_\varepsilon^{n+1} = \left(P_K - \widetilde{P_{ksgs}} + \widetilde{C_\varepsilon^n \frac{k_{sgs}^{3/2}}{\Delta}} \right) \frac{\tilde{\Delta}}{K^{\frac{1}{2}} \widetilde{k_{sgs}}} \tag{3.40}$$

The dissipation cannot be negative which requires that we limit C_ε to positive values. i.e., $C_\varepsilon \geq 0$. In equation (3.40) C_ε^n kept inside the filtering process which is similar to the procedure explained in the section (3.2.2.2).

To ensure numerical stability a constant value of *C* in space ($\langle C \rangle_{xyz}$) is used in the momentum equations, which is determined by condition that the production in the whole computational domain should remain the same, i.e.

$$\left\langle 2C\Delta k_{sgs}^{\frac{1}{2}} \overline{S}_{ij} \overline{S}_{ij} \right\rangle_{xyz} = \langle C \rangle_{xyz} \left\langle 2\Delta k_{sgs}^{\frac{1}{2}} \overline{S}_{ij} \overline{S}_{ij} \right\rangle_{xyz} \tag{3.41}$$

The main idea behind this treatment is to include all local dynamic information through the source terms of the transport equation for k_{sgs}. This is probably physically more meaningful since large local variations of *C* appear only in the source term, and the effect of the large fluctuations in the dynamic coefficients will be smoothed out in a natural way. This means that the need to restrict or limit the dynamic coefficient is reduced or may not be necessary altogether. However, if we have to restrict the dynamic coefficients in the k_{sgs} equation this does not affect the results as much as if the coefficient in the original dynamic model is restricted. The reason is that in the one-equation model the coefficients affect the stresses only in an indirect way (the source terms are part of a transport equation) whereas in the original dynamic model the dynamic coefficient is linearly proportional to the stresses.

The spatial variation of *C* is included via the production term in the modelled k_{sgs} equation. In this way backscatter is taken into account in an indirect way. Although it is not fed directly back to the resolved flow, it influences the resolved flow via the kinetic subgrid energy. A negative production reduces k_{sgs} and this effect influences the neighbourhood through convection and diffusion of k_{sgs}.

3.2.3 Anisotropic eddy viscosity models

These models are based on tensorial eddy viscosity. There are several anisotropic models available [41, 42, 43]. In the present work the following model is developed and implemented.

3.2.3.1 An anisotropic dynamic one equation subgrid scale model for large eddy simulation

This model was proposed by Akula et.al. [44]. It has been shown by Speziale [45] that the anisotropy exists at inertial as well as dissipation scales. Although the existing one-equation models well account for backscatter, they are not suitable for the representation of anisotropy of the subgrid-scales due to the local isotropy assumption made in the eddy viscosity formulation. Due to this assumption, these models may lead to wrong prediction of backscatter, and thus of the production of SGS kinetic energy. The latter strongly influences the evaluation of the turbulent viscosity, which plays a dominant role in flow predictions. The present model considers an anisotropic eddy viscosity formulation. In general a one equation model is based on the transport equation of SGS kinetic energy given by equation (3.10) as

$$\frac{\partial k_{sgs}}{\partial t} + \left(u_j k_{sgs}\right)_{,j} = \left(\left(\upsilon_t + \upsilon_l\right)\left(k_{sgs}\right)_{,j}\right)_{,j} - \tau_{ij} S_{ij} - \varepsilon \tag{3.42}$$

where
$$\nu_t = C\Delta\sqrt{k_{sgs}} \tag{3.43}$$

In the equation (3.43) the second and third terms in the right hand side represents production, dissipation. In the present approach the production term can be expressed as

$$P_{ksgs} = -\tau_{ij}^a S_{ij} \tag{3.44}$$

where
$$\tau_{ij}^a = -\left(\nu_{ik}\overline{S}_{kj} + \nu_{jk}\overline{S}_{ki}\right) \tag{3.45}$$

Here one can observe that we are using tensorial eddy viscosity instead of scalar eddy viscosity. The main reason behind this expression is to include the anisotropic effects in the prediction of the production of SGS kinetic energy.

$$\nu_{ij} = C_p\overline{\Delta}\sqrt{k_{sgs}}\,\frac{L_{ij}^a}{L_{kk}} \tag{3.46}$$

where L_{ij}^a is given by

$$L_{ij}^{a} = L_{ij} - \frac{\delta_{ij}}{3} L_{kk} \tag{3.47}$$

which is based on the assumption that the anisotropy of the unresolved turbulence-velocity scales is equal to the anisotropy of the resolved part of the SGS turbulent stress tensor (that is, the modified Leonard term): this assumption is somewhat similar to the similarity hypothesis formulated by Bardina [46] (see section 3.2.4), according to whom a strict analogy exists between the smallest resolved and the largest unresolved scales.

An additional modification to the dissipation term is introduced following the RANS low Reynolds number modelling

$$\varepsilon^{m} = \varepsilon + \varepsilon_{w} \tag{3.48}$$

$$\varepsilon_{w} = 2\nu \frac{\partial \sqrt{k_{sgs}}}{\partial x_{j}} \frac{\partial \sqrt{k_{sgs}}}{\partial x_{j}} \tag{3.49}$$

Model coefficient in the production term can be evaluated by using Germano identity from equation (3.14).

$$-C_{p} \frac{\tilde{\Delta}\sqrt{K}}{L_{kk}^{T}} \left(L_{ik}^{Ta} \tilde{S}_{kj} + L_{jk}^{Ta} \tilde{S}_{ki} \right) + \overline{\left(C_{p} \frac{\bar{\Delta}\sqrt{k_{sgs}}}{L_{kk}^{m}} \left(L_{ik}^{a} \bar{S}_{kj} + L_{jk}^{a} \bar{S}_{ki} \right) \right)} = L_{ij} \tag{3.50}$$

For more information see [44].

3.2.4 Scale similarity models

Scale similarity models (SSM) have been created to overcome the drawbacks of eddy viscosity type models. Basic idea of this model is the smallest resolved scales are not very different from the largest unresolved scales. This assumes that the most important interactions are the interactions between the largest subgrid scales and smallest resolved scales. In order to construct a model these scales have to be defined.

Unresolved scales ($\leq \Delta$) are represented by $u_i' = u_i - \bar{u}_i$. Largest unresolved scales are given by $\bar{u}_i' = \bar{u}_i - \bar{\bar{u}}_i$. Smallest resolved scales are defined by second filter on the resolved field and given by $\bar{u}_i - \bar{\bar{u}}_i$. It is very clear that largest unresolved scales and smallest resolved scales are represented by the same expressions. So we assume that these scales have similar structure (near grid cutoff). In other words, it is assumed that the SGS stresses for the full velocity field are the same as the ones corresponding to the resolved field $\bar{u}_i$ [46]

$$\tau_{ij} = \overline{u_i u_j} - \bar{u}_i \bar{u}_j \sim \overline{\bar{u}_i \bar{u}_j} - \bar{\bar{u}}_i \bar{\bar{u}}_j \tag{3.51}$$

These ideas are clearer by looking at the Fig. 3.2, from which one can understand the relation among the different velocity fields.

Performance of scale-similarity model:

- Improves energy spectra (compared to Smagorinsky)
- Can account for the transfer of energy from Small resolved scales → large resolved scales (backscatter accounted in a physical way)
- Correlates well with exact stress (a priori analysis)
- Not dissipative (does not dissipate energy automatically as Smagorinsky model with constant coefficient does, e.g., in laminar region of a flow the eddy viscosity and turbulence dissipation predicted by Smagorinsky model will be different from zero and positive, which is obviously wrong)
- Inadequate as stand-alone SGS model (not very robust numerically as it does not introduce enough dissipation in some cases, needs to be combined with a purely dissipative model, e.g., Smagorinsky like; this is the main idea behind mixed models to be discussed later)

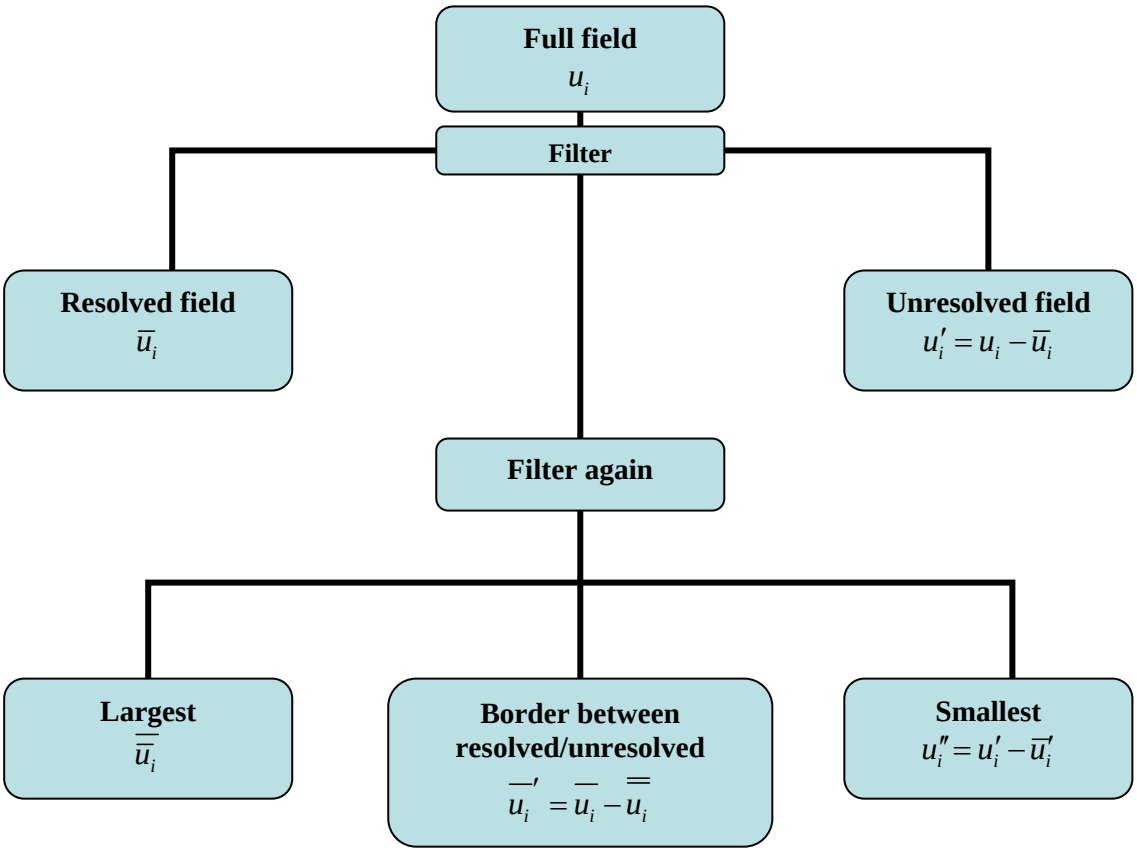

Figure 3.2 Explanation of different velocity scales in scale similarity model

Bardina model uses a second application of the same filter and therefore single cutoff scale. This model is generalized to the case of two cutoff levels by following Liu-Meneveau-Katz model [47]:

$$\tau_{ij} = C_1\left(\widetilde{\overline{u}_i\overline{u}_j} - \tilde{\overline{u}}_i\tilde{\overline{u}}_j\right) \tag{3.52}$$

One of the advantage of this model is that C_1 can vary from 0 to 1.

3.2.5 One parameter dynamic mixed model

In spite of its remarkable success, DSM has several aspects that need improvement. Because the Smagorinsky model is employed as the base model, DSM is an eddy viscosity model which requires that the principal axes of the SGS stress tensor be aligned with the resolved strain rate tensor. As Lund [34] has shown, although DSM accurately predicts the mean dissipation rate, it does not correlate with the channel flow DNS data of Kim et al. [48] as well as the Smagorinsky model in the local dissipation rate. A related and more serious problem arises when the dynamic model coefficient C is computed locally. Excessive energy backscatter occurs due to large fluctuations of the coefficient which leads to an exponentially growing instability [49].These results show that DSM can accurately predict the mean flow quantities when the averaged model coefficient is used but gives inadequate representation of the local quantities.

It is reasonable to argue that the local noise in the DSM may be reduced by using a base model which does not assume the alignment of the SGS stress and the resolved strain rate tensors. A model of this nature is the scale similarity model proposed by Bardina et al [46]. It was found that the scale similarity model did not dissipate energy, however, when it was combined linearly with the Smagorinsky model, the resulting “mixed model” did dissipate energy and predicted turbulence statistics better than the Smagorinsky model alone.

Based on these insights, Zang et. al. proposed the mixed model as the base model in the dynamic closure. The new model, which one might call the one parameter dynamic mixed model, retains the favourable features of DSM and has several additional advantages. The scale similarity or the resolved term is expected to provide a major part of the SGS backscatter which will reduce the fluctuation of the model coefficient and enable the SGS model to have a better representation of the local flow dynamics. In this model Smagorinsky model constant is calculated by the dynamic procedure. The subgrid tensor deviator at Δ-level and $\tilde{\Delta}$-level are given by

$$\tau_{ij} = -2\nu_t \overline{S}_{ij} + L_{ij} - \frac{1}{3} L_{kk}\delta_{ij} \tag{3.53}$$

$$T_{ij} = -2\nu_t \widetilde{\overline{S}}_{ij} + Q_{ij} - \frac{1}{3} Q_{kk}\delta_{ij} \tag{3.54}$$

in which

$$Q_{ij} = \widetilde{\overline{u}_i \overline{u}_j} - \widetilde{\overline{u}}_i \widetilde{\overline{u}}_j \tag{3.55}$$

and ν_t is given by equation (3.4).

The residual is given by

$$E_{ij} = L_{ij} - H_{ij} - \left(2CM_{ij} + \delta_{ij}P_{kk}\right) \tag{3.56}$$

in which

$$H_{ij} = \widetilde{\overline{u}_i}\widetilde{\overline{u}_j} - \widetilde{\overline{u}_i}\widetilde{\overline{u}_j} \tag{3.57}$$

and where P_{kk} represents the trace of the subgrid tensor. The Germano-Lilly procedure leads to:

$$C = \frac{\left(L_{ij} - H_{ij}\right)M_{ij}}{2M_{ij}M_{ij}} \tag{3.58}$$

Generally it has been observed that LES with this model reduce the value of the dynamic constant with respect to that predicted by the usual dynamic model, i.e., based on the Smagorinsky model. This can be explained by the fact that the difference between the L_{ij} and H_{ij} appears to be very small and gives small value for the dynamical constant. This shows that the subgrid viscosity model serves only to model a residual part of the full subgrid tensor and not totally, as in the usual dynamic model.

Vremen et. al. [50] proposed a variant of this model. For the sake of mathematical consistency, by making the model for the tensor T_{ij} dependent only on the velocity field that corresponds to the same level of filtering, i.e., $\widetilde{\overline{u}}$. In this model Q_{ij} given as:

$$Q_{ij} = \widetilde{\widetilde{\overline{u}_i}\widetilde{\overline{u}_j}} - \widetilde{\widetilde{\overline{u}_i}}\widetilde{\widetilde{\overline{u}_j}} \tag{3.59}$$

3.3 Further possibilities of the SGS modeling

In this section some further strategies for the SGS modelling are presented. Nevertheless these models are not implemented in this work.

One can improve the performance of the Smagorinsky model by considering the classical theories of turbulence. For e.g. the Smagorinsky model coefficient is calculated by assuming a Kolmogorov spectrum. This strategy is also pursued when defining a wave-number dependent eddy viscosity to be employed with a spectral Fourier discretization and using EDQNM theory to determine $\nu_t(k)$ [51].The spectral eddy viscosity model has also been reformulated in physical space for application in complex flows yielding the structure function model [52].

Generally Dynamic models are based on the scale similarity approach. To remedy this deficiency Porte-Agel et. al. [53] have proposed the scale dependent dynamic model. The model is based on a second test-filtering operation which allows us to determine from the simulation how the coefficient varies with scale. Nevertheless this model requires more computation time compared to general dynamic model. There is another popular model called as approximate deconvolution model from Stolz et.al. [54], in which the model is an approximation of the non-filtered velocity field by a truncated series expansion of the inverse filter operator.

Chapter 4

LES of turbulent premixed combustion

This chapter describes the modelling techniques for turbulent premixed flames. Initially the basic difficulties that exist in the modelling of premixed flames are presented and then various modelling techniques for the premixed flames are discussed. Especially modelling techniques based on the progress variable are presented clearly. Finally different techniques to handle the flame-wrinkling and flame-wall interactions are presented.

4.1 Introduction

Premixed Turbulent Combustion is a highly complex process, but one which greatly affects everyday life. The quest to understand the physical processes better is continual, and one aspect of it is the search for computational models to describe the processes involved. Such models must of necessity be less detailed than the physical processes occurring in the system, but should aim to capture the essence of these processes. In turn, the models can provide a greater understanding of the processes involved, and provide us with the ability to predict the behaviour of specific combustion systems. Thus they are of great importance in the design of combustion devices such as Internal Combustion (IC) engines and gas turbines.

A working model of turbulent combustion must provide adequate treatments for the turbulence, the chemical reactions of the combustion (and consequential heat release), as well as the mutual interaction of these areas, since the combustion alters the physical properties of the fluid and drives the flow, whilst the flow moves reactants and products around and thus influences the combustion. About the simplest possible model combines a Reynolds Averaged Navier–Stokes (RANS) description of the turbulence with a simplistic model of the combustion which provides a model for the heat release as a straightforward function of the reactant species concentration (for example, the Eddy Break-up model of Spalding [27]). Numerous improvements on these simple models have been investigated over the years, in particular concentrating on improved methods for characterising the species concentration at a point (and thus the prediction of the heat release) by PDF techniques, or improved flame modelling.

The Large eddy simulations (LES) are now viewed as a promising tool to address combustion problems where classical Reynolds-averaging numerical simulations (RANS) approaches

have proved to lack precision or where the intrinsically unsteady nature of the flow makes RANS clearly inadequate. LES allows a better description of the turbulence–combustion interactions because large structures are explicitly computed and instantaneous fresh and burnt gas zones, where turbulence characteristics are quite different, are clearly identified [15]. But LES of premixed combustion is difficult due to the thickness of the premixed flame being about 0.1–1 mm and generally smaller than the LES mesh size. For example progress variable *C* is a very stiff variable and the flame front cannot be resolved in the computation leading to numerical problems. In fact, the most important contribution to the reaction rate probably occurs at the subgrid scale level suggesting that LES could be impossible for the reactive premixed flows. To overcome this difficulty several approaches have been developed, such as flame front tracking techniques (e.g., the G equation [55,56]), flame surface density approach [57], and the so called thickened flame approach (TF-LES)[58,59].

4.2 Models for turbulent premixed combustion

There are mainly two different types of approaches are available for the modelling of turbulent premixed combustion. One is based on the flame tracking techniques (based on the G-equation) and other is based on the progress variable equation (*C* -equation). There are four different methods available based on the progress variable equation. They are

- Turbulent flame (or flame-speed) closure (TFC) model
- Flame wrinkling density model
- Flame surface density model
- Artificial thickened flame model

These models have been presented in the following section.

4.2.1 Flame front tracking techniques

4.2.1.1 G-equation approach:

Following Williams [23] and Kerstein et al. [60], a model equation that describes the convection and propagation of a thin, laminar fame is the *G*-equation. The *G*-equation, in conservative form, can be written as:

$$\frac{\partial}{\partial t}\left(\rho G\right)+\nabla\cdot\left(\rho u G\right)=-\rho S_L\left|\nabla G\right| \tag{4.1}$$

where *G* is a scalar variable defining the flame location and S_L is the laminar burning velocity of the flame (flame speed). *G*-equation assumes that the flame thickness is zero and

the flame front is described as a propagating surface tracked using *G*. The scalar field *G* is defined in the region between 0 to1 in which the unburnt products are assigned G = 1 and hot, reacted gases are *G* = 0. The flame surface is defined as an iso-scalar surface, G_o ($0 < G_o < 1$). Essentially, this models a level-surface, at $G = G_o$, being convected by the local flow field and propagating at S_L. All chemical and diffusive processes are implicitly included in S_L and, therefore, no specific species transport needs to be modelled.

Applying the same spatial filtering operation, as before, equation (4.1) can be adapted for the LES formulation. The resulting filtered G-equation [55] and resulting *SGS* terms are:

$$\frac{\partial}{\partial t}\left(\overline{\rho}\widetilde{G}\right)+\nabla\cdot\left(\overline{\rho}\tilde{u}\widetilde{G}\right)=-S^{sgs}-G^{sgs} \tag{4.2}$$

Where the subgrid terms are

$$S^{sgs}=-\overline{\rho_o S_L\left|\nabla G\right|} \tag{4.3}$$

$$G^{sgs}=\nabla\cdot\left(\overline{\rho u\widetilde{G}}-\overline{\rho}\tilde{u}\widetilde{G}\right) \tag{4.4}$$

Here ρ_o is the density of the unburnt reactants. These two *sgs* terms S^{sgs} and G^{sgs} represent the filtered reaction source term and unresolved turbulent transport. G^{sgs} is modelled as

$$G^{sgs}=\nabla\cdot\left(\rho D_t^{\widetilde{G}}\nabla\widetilde{G}\right) \tag{4.5}$$

where $D_t^{\widetilde{G}}$ is the turbulent diffusivity defined as ν_t/Sc_t (Sc_t is the turbulent Schmidt number which is defined as the ratio of viscous to chemical turbulent diffusion rates and usually assumed to be unity). This closure model has been successfully used in past studies [55, 62] of turbulent swirling flows.

The unresolved source term S^{sgs} can be modelled as,

$$S^{sgs}=-\rho_o S_t\left|\nabla\widetilde{G}\right| \tag{4.6}$$

where S_t is the local turbulent flame speed averaged over a characteristic LES cell and generally calculated by using Pocheau's flame speed model [63] . This model is explained in the section 4.2.3. This G-equation approach is similar to regress variable approach explained in the section 4.2.2.2.

4.2.1.2 Levelset G-equation

In this approach, G-equation is numerically tracked by using level-set methods [56]. Here a function *G* is constructed to have the property that the zero value iso-surface represents the combustion interface. *G* is not related to the progress variable, so other values of *G* have no physical significance and are merely chosen for computational convenience. The filtered flame front is represented by the G_o -iso-surface and separates the domain into perfectly mixed un-burnt (fresh) and burnt gas.

A straightforward transport equation is then solved for *G*:

$$\frac{\partial \widetilde{G}}{\partial t} = \left(\tilde{u}_u \cdot n + S_T\right)\left|\nabla \widetilde{G}\right| \tag{4.7}$$

Here S_T and u_u represents burning velocity and convective mass transport respectively. The unresolved wrinkling of the flame front is equivalent to an increase of the flame surface. This remains to be modelled. Under the assumption that the ratio of laminar to turbulent surface area is proportional to the ratio of laminar to turbulent flame propagation speed, the turbulent burning velocity is modelled by using:

$$S_T = S_L\left(1+\kappa L + C\left(\frac{u'_\Delta}{S_L}\right)^{3/4}\right) \tag{4.8}$$

Here, κ is the locally resolved curvature, *L* the Markstein length and the model constant *C* is set to unity [64]. Peters [20] used the thermal diffusivity D instead of $S_L L$, for a turbulent burning velocity valid in the regimes of the corrugated flamelets and the thin reaction zones. From theoretical arguments $D \sim S_L \delta_l$ and $L \sim \delta_l M$ can be derived, where *M* denotes the Markstein number and δ_l is flame thickness. Hence, equation (4.8) and the definition given in [20] are altered by the Markstein number, which is in the order of unity. The laminar flame speed, used in equation (4.8) depends only on the thermo-chemical state of the premixed gas [65].

4.2.2 Premixed combustion modelling based on progress variable equation

Several turbulent premixed combustion modelling approaches based on a *C*-equation are described briefly in this section.

4.2.2.1 C-equation

In an adiabatic premixed combustion with one-step and irreversible chemistry, if the specific heat capacity of species is assumed constant, then the reactive species concentration and the

temperature are all linearly related to a non-dimensional temperature *C*, known as reaction progress variable. It is defined as

$$C = \frac{T - T_u}{T_b - T_u} \tag{4.9}$$

The balance equation for the progress variable *C* may be written as [57]:

$$\frac{\partial \rho C}{\partial t} + \nabla \cdot \left(\rho u C\right) = \nabla . \left(\rho D \nabla C\right) + \dot{\omega}_C \tag{4.10}$$

$$= \rho S_d \left|\nabla C\right| \tag{4.11}$$

Here, *D* is the molecular diffusivity, *u* is velocity vector. Equation (4.11) is another form of *C*-equation written in terms of flame front displacement speed S_d . Appling the LES filter, it becomes

$$\frac{\partial \overline{\rho}\widetilde{C}}{\partial t} + \nabla \cdot \left(\overline{\rho}\tilde{u}\widetilde{C}\right) + \nabla \cdot \left[\overline{\rho}\left(\widetilde{uC} - \tilde{u}\widetilde{C}\right)\right] = \overline{\nabla . \left(\rho D \nabla C\right)} + \overline{\dot{\omega}_C} \tag{4.12}$$

$$= \overline{\rho S_d \left|\nabla C\right|} \tag{4.13}$$

The three terms on the l.h.s. of equation (4.12) are unsteady effects, resolved convective flux and unclosed transport flux, respectively. On the r.h.s. of equation (4.12), the two terms denote respectively filtered molecular diffusion and filtered reaction rate. The unclosed transport flux is usually modelled with a simple gradient expression:

$$\overline{\rho}\left(\widetilde{uC} - \tilde{u}\widetilde{C}\right) = -\frac{\mu_t}{Sc_t}\nabla\widetilde{C} \tag{4.14}$$

Several approaches are proposed to estimate the unclosed term on (4.13). A brief description of them is given in the following sections.

4.2.2.2 Turbulent flame closure model

In the turbulent flame (or flame-speed) closure (TFC) model, the unclosed term on (4.13) is estimated based on a turbulent flame speed as

$$\overline{\rho S_d \left|\nabla C\right|} = \rho_u S_t \left|\nabla \widetilde{C}\right| \tag{4.15}$$

S_t is the subgrid turbulent flame speed in LES framework.

The TFC model was first proposed by [66] and has recently been applied and tested on some premixed combustion cases [67, 68]. Based on the Kolmogorov assumption of the equilibrium fine-scale turbulence and the assumption of the universal small-scale structure of the wrinkled

flamelet sheet, Zimont [68] proposed an expression for the turbulent flame speed S_t in RANS context. It is shown below:

$$S_t = C \cdot u' \cdot \left(Da\right)^{1/4} \tag{4.16}$$

C is an empirical parameter, which has a value around 0.5. *Da* is the Damköhler number. Flohr and Pitsch [69], and Zimont and Battaglia [70] have applied the TFC model in LES framework. The subgrid turbulent flame speed is S_t expressed as [69]

$$S_t / S_L = 1 + C\left(\mathrm{Re}_\Delta \, \mathrm{Pr}\right)^{1/2} Da^{-1/4} \tag{4.17}$$

Where $\mathrm{Re}_\Delta = u'_\Delta \Delta / \nu$. The subgrid turbulent velocity u'_Δ is estimated as

$$u'_\Delta = C_S \Delta \left(2\widetilde{S_{ij}}\widetilde{S_{ij}}\right)^{1/2} \tag{4.18}$$

where $\widetilde{S_{ij}}$ is the filtered strain rate tensor.

4.2.2.3 Flame wrinkling density model

This model is developed by the application of conditional averaging techniques to the turbulent flame interface. The flame distribution is represented by a flame wrinkle density scalar Ξ, which is the ratio between the turbulent flame surface and its projection in the propagation direction. A detailed derivation of this model in RANS framework may be found in Weller [71]

A new flame wrinkling model in LES context is proposed by Weller et al. [72] and then applied to study combustion instabilities in a jet engine afterburner [73] Like the model used in RANS, it considers a regress variable *b* instead of progress variable *C.* Here *b* represents the unburnt gas mass fraction, which has a relation with *C* as *b=1-C.* A transport equation is obtained by filtering the conditional transport

$$\frac{\partial \overline{\rho}\tilde{b}}{\partial t} + \nabla \cdot \left(\overline{\rho}\tilde{u}\tilde{b}\right) = \nabla . \left(\overline{\rho} D \nabla \tilde{b}\right) + \rho_u S_L \Xi \left|\nabla \tilde{b}\right| \tag{4.19}$$

A transport equation for the flame wrinkle density scalar Ξ is then proposed

$$\frac{\partial \Xi}{\partial t} + \widehat{\upsilon_s} \cdot \nabla \Xi = G\Xi - R\left(\Xi - 1\right) + \left(\sigma_s - \sigma_t\right)\Xi \tag{4.20}$$

where $\widehat{\upsilon_s}$ is the surface-filtered effective velocity of the flame. $G\Xi$ and $R\left(\Xi - 1\right)$ are the subgrid turbulent generation and removal rates, respectively. Expressions for $\widehat{\upsilon_s}$, $G\Xi$ and

$R(\Xi-1)$ are proposed by Weller et al. [72] σ_t and σ_s are two resolved strain rates, which can be expressed with resolved quantities.

In addition to the transport equation for Ξ, Weller et al. [72] even proposed a transport equation for the laminar flame speed S_L to account for the strain rate influence on the laminar flame speed though no rigorous validation is made. Information regarding this equation can be found in Weller et al. [72]

4.2.2.4 Flame surface density model

This model is based on the approach to describe the unclosed term in equation (4.13) is based on the concept of filtered flame surface density. The flame surface density $\sum$ describes the flame front convolutions.

$$\overline{\rho S_d \left|\nabla C\right|} = \left(\rho_u S_L\right)\sum \tag{4.21}$$

Where ρ_u is the unburnt gas mass density, S_L is the laminar flame speed.

The surface density $\sum$ can be expressed either in an algebraic form or in a balanced equation. In the present study the algebraic form is used. This approach was developed by [57]. They carried out 3-D DNS analysis of a laminar flame into a homogeneous and isotropic turbulent flow field and proposed to LES-filter the progress variable equation using a filter larger than the mesh size. The surface density $\sum$ was modeled with DNS data in their calculations.

The proposed LES-filtered surface density reads as

$$\sum = 4\sqrt{\frac{6}{\pi}}\Xi\frac{C(1-C)}{\Delta_C} \tag{4.22}$$

Here Ξ denotes the *sgs* flame front wrinkling factor (Ξ =1 in absence of subgrid-scale flame surface wrinkling) and Δ_C is the filter size larger than the actual LES mesh.

Finally progress variable equation in the contest of LES is expressed as

$$\frac{\partial\bar{\rho}\widetilde{C}}{\partial t}+\nabla\cdot\left(\bar{\rho}\tilde{u}\widetilde{C}\right)=\nabla.\left[\left(\rho_u\frac{S_L\Delta_C}{16\sqrt{6/\pi}}+\frac{\mu_t}{Sc_t}\right)\nabla.\widetilde{C}\right]+4\rho_u S_L\Xi\sqrt{6/\pi}\,\frac{\widetilde{C}(1-\widetilde{C})}{\Delta_C} \tag{4.23a}$$

$$\bar{\rho}=\frac{\rho_u}{1+\tau\widetilde{C}} \qquad or \qquad \bar{\rho}\widetilde{C}=\frac{\rho_u-\bar{\rho}}{\tau} \tag{4.23b}$$

Where μ_t is the turbulent viscosity, Sc_t is turbulent Schmidt number, ρ_u is unburnt density and τ is expansion ratio.

The extra diffusion term in equation (4.23a) is added to preserve the correct flame propagation speed and thickness even in the laminar regions of the flow [74].

One can also use a transport equation for the evaluation of the surface density Σ, which is proposed by the Hawkes and Cant [75] and written as

$$\frac{\partial \Sigma}{\partial t}+\frac{\partial\left(\widetilde{u}_i \Sigma\right)}{\partial x_i}+\frac{\partial}{\partial x_i}\left(\left(\overline{\left(u_i\right)_s}-\widetilde{u}_i\right)\Sigma\right)=\overline{\left(a_T\right)_s}\Sigma - \frac{\partial}{\partial x_i}\left(\overline{\left(S_L N_i\right)_s}\Sigma\right)+\overline{\left(S_L \frac{\partial N_i}{\partial x_i}\right)_s}\Sigma \tag{4.24}$$

where the subscript s represents the subgrid scale. The three terms on the l.h.s of (4.24) are the rate of change, the mean flow convection, and the subgrid convection respectively. On the r.h.s. there are the effects of fluid strain, a planar propagation term, and production of flame surface density related to the curvature and propagation effect. The last four terms on (4.24) are unclosed and have to be modelled. Boger et al. [57] argued that these terms may be easily extracted from DNS or experimental results, since they are physically well defined terms.

4.2.2.4 Artificial Thickened Flame Model

It was argued that reducing the flame to an infinitely thin surface is interesting from a modeling point of view but that in practice, numerics always impose a certain thickness of the flame on the computational grid. This will compromise the accuracy of the approach if the thickness of the flame is not controlled and its influence not taken in the combustion modeling. An alternative method is to drop the theoretical “zero thickness” of G-equation approach and build a method where the flame has a controlled, non-zero thickness. This leads to the artificially thickened flame model (TFLES), described in the following.

Thickening

From asymptotic analysis on laminar premixed flames a simple expression for the laminar flame speed and thickness follows:

$$S_l \propto \sqrt{DA} \qquad \delta_l \propto \frac{D}{S_l}=\sqrt{\frac{D}{A}} \tag{4.25}$$

where A is the pre-exponential constant of a global reaction and D is the molecular diffusivity.If the thermal conductivity is increased by a factor F while the pre-exponential

constant is decreased by F, the flame thickness δ_l is multiplied by F while the flame speed is maintained. This approach was initially proposed by Butler et al. [76] and extended to LES by Colin et al. [77].

Unfortunately, when the flame is thickened from δ_l to $F\delta_l$, the interaction between turbulence and chemistry is modified because Karlovitz and Damköhler numbers change:

$$Ka^m = Ka.F \qquad Da^m = Da / F \tag{4.26}$$

By applying the thickening approach to the progress variable equation one can get the following equation [58,59]

$$\frac{\partial \bar{\rho}\tilde{c}}{\partial t} + \nabla \cdot \left(\bar{\rho}\tilde{u}\tilde{c} \right) = \nabla \cdot \left(\bar{\rho} DF \nabla \tilde{c} \right) + \frac{A}{F} \bar{\rho}(1-\tilde{c}) \exp\left(-\frac{T_a}{T} \right) \tag{4.27}$$

Here A represents pre-exponential factor and T_a is the activation temperature. The thickened flame approach has several attractive features [77]: (1) From a numerical point of view, the chemical reaction is described in a way which properly tends to the DNS expressions when $F \rightarrow 1$, and whose implementation is attractive since it has the same form as DNS (i.e., the same code can be used for LES and DNS). (2) Because of the use of an Arrhenius law, various phenomena such as ignition, flame stabilization, flame/wall interactions, and so forth can be described, at least qualitatively.

However, as discussed in Refs. [77] the thickening of the flame implies that flame turbulence interaction is modified since the Damköhler number Da comparing turbulent and chemical time scales is decreased by the factor F when thickening the flame. Thus, the response of the thickened flame to the spectrum of eddies found in turbulent flows will not be the same as that of the unthickened flame. Moreover, it obviously cannot be wrinkled at scales below the resolution limit of the LES. To account for this E_F is introduced which is explained in the section 4.2.3. With this factor the equation (4.27) is written as:

$$\frac{\partial \bar{\rho}\tilde{c}}{\partial t} + \nabla \cdot \left(\bar{\rho}\tilde{u}\tilde{c} \right) = \nabla \cdot \left(\bar{\rho} DE_F F \nabla \tilde{c} \right) + \frac{A}{F} E_F \bar{\rho}(1-\tilde{c}) \exp\left(-\frac{T_a}{T} \right) \tag{4.28}$$

Local optimal thickening

Assuming that the computational grid in the region where combustion takes place is uniform ($\Delta \approx$ const.), the thickening factor F can be fixed as a constant value. This rarely applies to meshes describing complex geometries. Two extreme cases may occur:

- If the flame is thicker than Δ_e=10Δ, the sub-grid contribution to combustion will be too large, the flame will not be wrinkled and the LES will actually be a URANS computation.
- If the flame is thinner than the resolution capability of the numerical scheme, either the solver will diverge or the efficiency function will be dominated by numerical errors.

This requires the computation of a local, optimal value of *F*. As the efficiency function needs the thermal flame thickness δ_l as an input, this value can be used and compared to the local mesh spacing Δ_C (characteristic length of the computational cell). This results in a relation for the thickening factor:

$$F = 1 + \left(\frac{N_C . \Delta_C}{\delta_l} - 1 \right) . S \tag{4.29}$$

where N_C is the number of computational cells needed to resolve a flame without significant numerical errors. N_C depends on the numerical scheme used but not on the cell-type. *S* is a flame sensor for the local thickening and is generally taken as 1 for premixed flames.

4.3 Flame-wrinkling models

4.3.1 Pocheau's flame speed model

In this flame speed model [63], the turbulent flame speed is calculated by the following expression:

$$S_T = S_L \left[1 + \beta \left(\frac{u'_\Delta}{S_L} \right)^\alpha \right]^{1/\alpha} \tag{4.30}$$

where u'_Δ is the unresolved fluctuating velocity and is calculated as:

$$u'_\Delta = C_S \Delta \left(S_{ij} S_{ij} \right) \tag{4.31}$$

Here C_S is Smagorinsky model constant which can be evaluated by using dynamic procedure explained in the chapter 3. Following Kim et al. [55] α and β are taken as 2 (based on energy conservation) and 20, respectively.

4.3.2 Efficiency Function

In this approach an "efficiency function" E_F takes into account the effects of thickening and residual turbulence on the turbulent flame speed [77]. Based on the ideas behind the ITNFS

approach by Meneveau et al. [78], the ability if different turbulence length scales to wrinkle the flame was incorporated in this model. This is essential, as shown for example by Poinsot et al. [79] via flame/vortex interactions.

The wrinkling factor of the flame surface Ξ is estimated from the flame surface density Σ, assuming equilibrium between the turbulence and the residual flame surface:

$$\Xi = 1 + \alpha_f \frac{\Delta_e}{S_l} \langle a_T \rangle_s \tag{4.32}$$

where $\langle a_T \rangle_s$ is the residual strain rate, Δ_e is the filter size and α_f is a model constant. $\langle a_T \rangle_s$ is estimated from the filter size Δ_e and the associated turbulent velocity fluctuation u'_Δ :

$$\langle a_T \rangle_s = \Gamma \frac{u'_\Delta}{\Delta_e} \tag{4.33}$$

The function Γ corresponds to the integration of the effective strain rate induced by all scales affected by the artificial thickening. They range from Kolmogorov scale to η_k to the filter scale Δ_e [4.24]. Γ is written as:

$$\Gamma\left(\frac{\Delta_e}{\delta_l}, \frac{u'_{\Delta_e}}{S_l}\right) = 0.75 \exp\left[-\frac{1.2}{\left(u'_\Delta / S_l\right)^{0.3}}\right]\left(\frac{\Delta_e}{\delta_l}\right)^{\frac{2}{3}} \tag{4.34}$$

Finally, the efficiency function is defined as the wrinkling ratio between the non-thickened reference flame and the artificially thickened flame:

$$E = \frac{\Xi(\delta_l)}{\Xi(F\delta_l)} = \frac{1 + \alpha_F \Gamma\left(\frac{\Delta_e}{\delta_l}, \frac{u'_\Delta}{S_l}\right)\frac{u'_\Delta}{S_l}}{1 + \alpha_F \Gamma\left(\frac{\Delta_e}{F\delta_l}, \frac{u'_\Delta}{S_l}\right)\frac{u'_\Delta}{S_l}} \tag{4.35}$$

The constant α_F depends nearly exclusively on the turbulence Reynolds number Re_t. Details on its evaluation can be found in the literature [77]. The filter size Δ_e is generally not identical to the LES filter. In practical calculations it is set to $\Delta_e = 10\Delta$. The obtained E_F is varies between 1 (for weak turbulence) and

$$E_{\max} \approx F^{2/3} \tag{4.36}$$

(for large residual scale wrinkling). Multiplying the thermal diffusivity and the pre-exponential constant by the efficiency function E_F keeps the flame thickness constant and accelerates the flame by a factor E_F. In summery, the residual turbulent flame speed S_T and the LES flame thickness δ_T become:

$$S_T = E_F.S_L \qquad \delta_T = F.\delta_L \tag{4.37}$$

This has an impact on the Karlovitz and Damköhler numbers. The error introduced by the thickening is partly compensated (when replacing S_L with S_T):

$$Ka' = Ka.F/E_F \qquad Da' = Da.E_F/F \tag{4.38}$$

In combination with equation (4.36) it is seen that the final model still modifies the regime depending on the thickening factor chosen. Therefore, too high values of *F* should be avoided. However in practical simulations it is assumed that $\Delta_e/F\delta_l$ is equal to 1 [58]. With this assumption, efficiency function calculated as $E_F = \Xi(\delta_l)$.

4.3.3 Charlette model

This model [58] is based on calculating the unresolved flame surface density in terms of a general power-law expression that involves an inner cutoff scale. This scale is derived from an equilibrium assumption of flame-surface production and destruction. In this model, flame wrinkling is calculated as:

$$\Xi = \left[1 + \min\left(\frac{\Delta}{\delta_l}, \Gamma\frac{u'_\Delta}{S_L}\right)\right]^\beta \tag{4.39}$$

Γ represents efficiency function and calculated by using the following fit.

$$\Gamma = \left[\left(\left(f_u^{-a} + f_\Delta^{-a}\right)^{-1/a}\right)^{-b} + f_{\mathrm{Re}}^{-b}\right]^{-1/b} \tag{4.40}$$

Where

$$f_u = 4\cdot\left(\frac{27\cdot C_k}{110}\right)^{1/2}\left(\frac{18C_k}{55}\right)\left(\frac{u'_\Delta}{S_L}\right)^2 \tag{4.41}$$

$$f_\Delta = \left[\frac{27C_k\pi^{4/3}}{110}\times\left(\left(\frac{\Delta}{\delta_L}\right)^{4/3} - 1\right)\right]^{1/2} \tag{4.42}$$

$$f_{\mathrm{Re}} = \left[\frac{9}{55}\exp\left(-\frac{3}{2}C_k\pi^{4/3}\,\mathrm{Re}_\Delta^{-1}\right)\right]^{1/2}\times\mathrm{Re}_\Delta^{1/2} \tag{4.43}$$

Here C_k is universal Kolmogorov constant and is equal to 1.5. Re_Δ can be evaluated as $\frac{u'_\Delta \Delta}{\nu}$.

In the equation (4.40) exponents *a* and *b* control the sharpness of the transitions between the asymptotic behaviours, and good results are obtained with the following expressions:

$$a = 0.60 + 0.20\exp\left[-0.1\left(u'_\Delta / S_l\right)\right] - 0.20\exp\left[-0.01\left(\Delta/\delta_l\right)\right] \quad (4.44)$$

$$b = 1.4 \quad (4.45)$$

In equation (4.39) β represents power exponent and it varies in between 0 to 1.0. Nevertheless this constant value can be calculated by dynamic procedure [59]. For the present work $\beta = 0.5$ is used.

4.4 Flame-wall interactions:

Flame wall interactions are handled by the two different approaches [15] based on the flame propagation relative to the wall. These approaches are

4.4.1 Head on quenching (HOQ):

If the premixed flame propagates towards the wall, HOQ is observed; the flame stops at a certain distance from the wall (of the order of the flame thickness) and the maximum wall flux (reached when the flame quenches) is of the order of one third of the total flame.

4.4.2 Side–wall quenching (SWQ):

If the premixed flame propagates along the wall, the distance between wall and flame is larger than HOQ and the flux slightly lower.

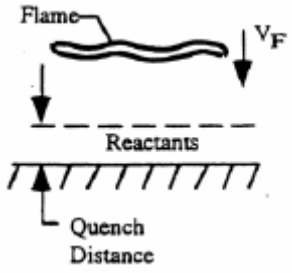

Fig. 5.1 Head on quenching

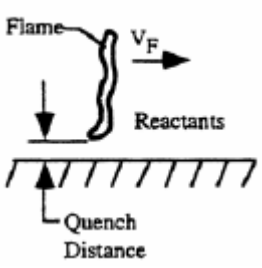

Fig. 5.2 Side wall quenching

But the above two methods can be used only if the wall temperatures are available as mention by Poinsot et al [15]. But, in general, this information is very rarely available.

4.4.3 Two-zones approach

For the cases where wall temperatures are not available the following numerical quenching method has been proposed by the author in the present work. This has been performed in two

zones near the wall. The basic idea of this method is not to allow the flame in to viscous sub-layer.

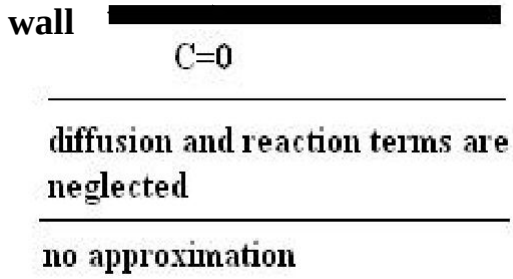

Fig. 5.3 *Quenching used in this work*

In the immediate zone to the wall progress variable has been always taken as zero. In the next zone reaction term in equation is neglected first and then the diffusion term is neglected. Neglecting the reaction term represents numerical quenching and whereas neglecting diffusion term means not allowing the excessive thickening of the flame near the wall.

Chapter 5

Numerical Methodology

This chapter describes the numerical techniques used for the present work based on the governing equations described in the previous chapters. In the present work the CFD package FASTEST-3D (Flow Analysis Solving Transport Equations Simulating Turbulence 3 Dimensional) was used. In this chapter initially the overall structure of the code has been presented and then finally methodologies of the implemented techniques are presented.

5.1 Introduction to FASTEST -3D code

FASTEST -3D was originally developed by INVENT computing company and obtained as a source code in the framework of the collaborative research project SFB-568. The basic features of this code are:

- Finite Volume discretisation method based on hexahedral control volumes
- Cartesian coordinate and basis vector system
- Boundary-fitted non-orthogonal block-structured grid with matching interfaces and collocated variable arrangement
- Implicit and semi-implicit temporal treatment and first (upwind) and second (central difference and TVD schemes) order discretisation schemes.
- Strongly implicit procedure for the iterative solution of the linearised equation system
- Parallelisation based on domain decomposition in space using the MPI message passing library

Nevertheless for the present work only the fully implicit scheme with second order discretisation was used.

5.1.1 Finite volume method

The finite volume method is used in the frame of this work to describe the continuous phase. This method is based on the governing equations in the integral form given by the equation (5.1):

$$\int_V \frac{\partial}{\partial t}(\rho\psi)\,dV + \int_V \frac{\partial}{\partial x_i}(\rho u_i \psi)\,dV = \int_V \frac{\partial}{\partial x_i}\left(\Gamma_\psi \frac{\partial \psi}{\partial x_i}\right)dV + \int_V S_\psi\,dV \tag{5.1}$$

.

The quantity ψ represents a conserved variable (velocity component, scalar, etc.), Γ_ψ notes the diffusivity coefficient, S_ψ the sum of all source terms and V the volume of the considered cell. The volume integrals are transformed to area integrals by using Gauss' Law as:

$$\int_V \frac{\partial}{\partial t}(\rho\psi)\,dV + \int_\sigma \left(\rho u_i \psi - \Gamma_\psi \frac{\partial \psi}{\partial x_i} \right) n_i\, d\sigma = \int_V S_\psi\, dV \qquad (5.2)$$

where σ represents the surface confining the volume V (of the cell) and n_i the unit vector normal to the surface σ. The equation (5.2) is applied for each control volume (CV) of the numerical grid which defines the computational domain where the discrete locations at which the variables are to be calculated (see Fig. 5.1). The storage of the flow information related to every CV divides the discretization problem into two different arrangements, namely: collocated grid and staggered grid.

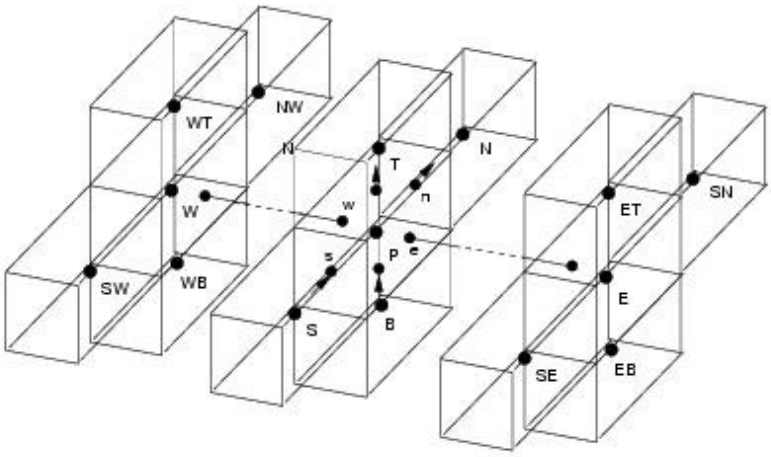

Figure 5.1 *Topology and control volume notification*

Collocated grid, as used in this work, is one in which the pressure and velocity variables share the same grid (see Fig. 5.2). Thus all variables are stored on the same grid point and the same control volume is used for all variables. It is the preferred method for nonorthogonal coordinates. The implementations of collocated grids on nonorthogonal coordinates require regularization to prevent the formation of oscillations because of pressure velocity decoupling [80].

Now consider a hexahedral control volume with central point denoted as P, having six neighbors CVs: E (east), W (west), N (north), S (south), T (top) and B (bottom) (see Fig. 5.1) and sharing common faces with neighbors: e, w, n, s, t and b, respectively. The final objective

within finite volume method is to transform the integral differential equation (5.2) into an algebraic equation of the following form:

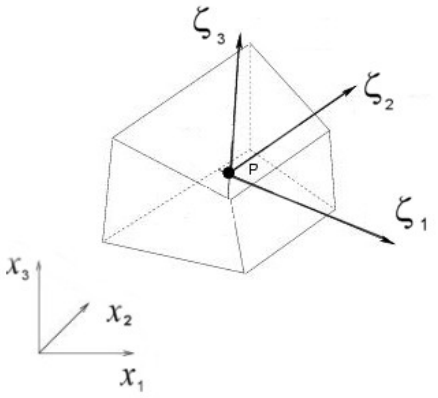

Figure 5.2 *Collocated grid*

$$\underbrace{A_p\psi_p - \sum_{Nb} A_{Nb}\psi_{Nb}}_{\text{implicit part}} = \underbrace{S_p}_{\text{explicit part}} \tag{5.3}$$

Here, the subscript *Nb* corresponds to the 6 neighbors CVs: W, E, S, N, B, T and A_p, A_{Nb} denote the coefficients belonging to the dependent variable values ψ_p, ψ_{Nb} in the point P, *Nb* derived from the discretization. All the remaining terms resulting from the discretization that can not be included into the implicit part of equation (5.3) are treated explicitly and put into the source term S_p on the RHS.

5.1.2 Coordinate transformation

Taking into account the non-orthogonality of the grid used, it is plausible to use in each CV and on each CV face a local coordinate system and then to transform the operators (derivatives) from local into the global (Cartesian) coordinate system. In Fig. 5.3 a local coordinate system arranged in the CV central point is shown. The basis vectors of the local coordinate system are obtained connecting the CV central point with the central points of the CV's faces.

The local coordinates are in the following denoted as $(\zeta_1, \zeta_2, \zeta_3)$ while global (Cartesian) coordinates are denoted as (x_1, x_2, x_3). The transformation matrix (for transformation from the global into the local coordinate system) is shown in equation (5.4).

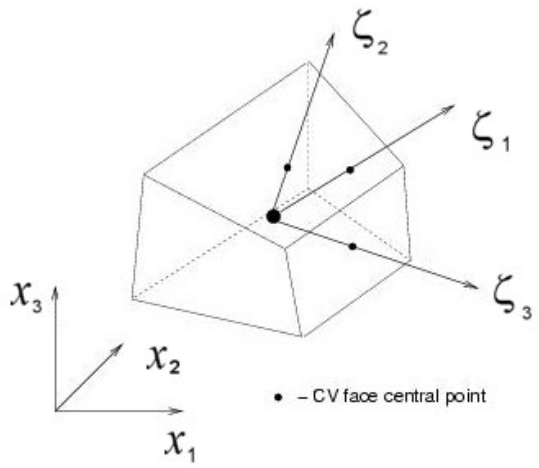

Figure 5.3 Local coordinate system arranged in the CV central point.

$$A=\begin{pmatrix} \frac{\partial x_1}{\partial \zeta_1} & \frac{\partial x_1}{\partial \zeta_2} & \frac{\partial x_1}{\partial \zeta_3} \\ \frac{\partial x_2}{\partial \zeta_1} & \frac{\partial x_2}{\partial \zeta_2} & \frac{\partial x_2}{\partial \zeta_3} \\ \frac{\partial x_3}{\partial \zeta_1} & \frac{\partial x_3}{\partial \zeta_2} & \frac{\partial x_3}{\partial \zeta_3} \end{pmatrix} \tag{5.4}$$

The derivative of some field variable ψ with respect to Cartesian coordinates can be expressed in terms of the local coordinates according to

$$\frac{\partial \psi}{\partial x_i}=\frac{\partial \psi}{\partial \zeta_j}\frac{\partial \zeta_j}{\partial x_i} \tag{5.5}$$

The elements of the inverse transformation matrix, A^{-1}, (local to global),

$$A^{-1}=\begin{pmatrix} \frac{\partial \zeta_1}{\partial x_1} & \frac{\partial \zeta_1}{\partial x_2} & \frac{\partial \zeta_1}{\partial x_2} \\ \frac{\partial \zeta_2}{\partial x_1} & \frac{\partial \zeta_2}{\partial x_2} & \frac{\partial \zeta_2}{\partial x_3} \\ \frac{\partial \zeta_3}{\partial x_1} & \frac{\partial \zeta_3}{\partial x_2} & \frac{\partial \zeta_3}{\partial x_3} \end{pmatrix} \tag{5.6}$$

are obtained from the well-known linear algebraic relation:

$$A^{-1}=\frac{1}{J}\left(A_{adj}\right)^T \tag{5.7}$$

where $J = \det(A)$ is the Jacobean and (A_{adj}) is the transpose adjoint matrix obtained from matrix A. I.e.

$$\frac{\partial \zeta_j}{\partial x_i} = \frac{1}{J}\left[adj\left(\frac{\partial x_j}{\partial \zeta_i}\right)\right]^T = \frac{1}{J}\beta_{ij} \tag{5.8}$$

and

$$\frac{\partial \psi}{\partial x_i} = \frac{1}{J}\beta_{ij}\frac{\partial \psi}{\partial \zeta_j} \tag{5.9}$$

where β_{ij} is the element of matrix B given by

$$B = \begin{pmatrix} \frac{\partial x_2}{\partial \zeta_2}\frac{\partial x_3}{\partial \zeta_3} - \frac{\partial x_2}{\partial \zeta_3}\frac{\partial x_3}{\partial \zeta_2} & \frac{\partial x_1}{\partial \zeta_3}\frac{\partial x_3}{\partial \zeta_2} - \frac{\partial x_1}{\partial \zeta_2}\frac{\partial x_3}{\partial \zeta_3} & \frac{\partial x_1}{\partial \zeta_2}\frac{\partial x_2}{\partial \zeta_3} - \frac{\partial x_1}{\partial \zeta_3}\frac{\partial x_2}{\partial \zeta_2} \\ \frac{\partial x_2}{\partial \zeta_3}\frac{\partial x_3}{\partial \zeta_1} - \frac{\partial x_2}{\partial \zeta_1}\frac{\partial x_3}{\partial \zeta_3} & \frac{\partial x_1}{\partial \zeta_1}\frac{\partial x_3}{\partial \zeta_3} - \frac{\partial x_1}{\partial \zeta_3}\frac{\partial x_3}{\partial \zeta_1} & \frac{\partial x_1}{\partial \zeta_3}\frac{\partial x_2}{\partial \zeta_1} - \frac{\partial x_1}{\partial \zeta_1}\frac{\partial x_2}{\partial \zeta_3} \\ \frac{\partial x_2}{\partial \zeta_1}\frac{\partial x_3}{\partial \zeta_2} - \frac{\partial x_2}{\partial \zeta_2}\frac{\partial x_3}{\partial \zeta_1} & \frac{\partial x_1}{\partial \zeta_2}\frac{\partial x_3}{\partial \zeta_1} - \frac{\partial x_1}{\partial \zeta_1}\frac{\partial x_3}{\partial \zeta_2} & \frac{\partial x_1}{\partial \zeta_1}\frac{\partial x_2}{\partial \zeta_2} - \frac{\partial x_1}{\partial \zeta_2}\frac{\partial x_2}{\partial \zeta_1} \end{pmatrix} \tag{5.10}$$

Substitution of the expression for the differential operator (5.9) into equation (5.2) gives

$$\int_V \frac{\partial}{\partial t}(\rho\psi)\,dV + \int_\sigma \left(\rho u_i \psi - \Gamma_\psi \frac{\partial \psi}{\partial x_i}\right) n_i\, d\sigma = \int_V S_\psi\, dV \tag{5.11}$$

5.1.3 Discretization of the convective and diffusion terms

The discretization of the convective term is given by:

$$\begin{aligned} \int_\sigma \rho u_i \psi n_i\, d\sigma = \sum_{k=e,w,n,s} a_k \sigma_k = (\rho u\psi)_e\, \sigma_e - (\rho u\psi)_w\, \sigma_w + \\ (\rho u\psi)_n\, \sigma_n - (\rho u\psi)_s\, \sigma_s + (\rho u\psi)_t\, \sigma_t - (\rho u\psi)_b\, \sigma_b \end{aligned} \tag{5.12}$$

The problem now is how to approximate the value ψ at the faces *e, w, n, s, t* and *b.* There are three basic discretization schemes.

The first common way is to use linear interpolation leading to a **Central Differencing Scheme** (CDS). The value of ψ (e.g. at the east face) is estimated using the neighbors nodes P and E (see Fig. 5.1)

$$\psi_e = f_x \psi_E + (1 - f_x)\psi_P \tag{5.13}$$

where f_x is the interpolation function, and for a constant mesh spacing $f_x = 0.5$. The central differencing scheme has a second order accuracy. One can prove this by applying the Taylor series expansion on the point *P*. The accuracy is proportional to the square of grid width. I.e.

if the number of cells within one direction is doubled, the error will be divided by a factor of 4.

The Upwind Differencing Scheme (UDS) assumes that the neighboring cell value for ψ will be convected across the boundary:

$$\psi_e = \begin{cases} \psi_P & \text{if} \quad u_e \geq 0 \\ \psi_E & \text{if} \quad u_e < 0 \end{cases} \tag{5.14}$$

The main drawback of the upwind scheme is that it is inaccurate and very diffusive, because it is of first order.

The Flux Blending switches between the two, according to the relative size of the convective and diffusive fluxes across the cell face. By resulting in oscillation, one can combine UDC and CDS to calculate the value at the faces *e*:

$$\psi_e = \underbrace{\psi_e^{UDS}}_{I} + \underbrace{\gamma\left(\psi_e^{CDS} - \psi_e^{UDS}\right)}_{II} \tag{5.15}$$

where $0 \leq \gamma \leq 1$ is factor which scales the manner of flux blending. For $\gamma = 1$, the interpolation is pure CDS whereas for $\gamma = 0$, the interpolation is pure Upwind. Part I of (5.15) is treated implicitly whereas part II is treated explicitly. The flux blending scheme is a good control tool to achieve an optimum between stability and accuracy. Nevertheless the present work deals with the large eddy simulation and therefore only central difference schemes are used to avoid the numerical diffusion.

For the diffusive part, a centered difference for the discretization of the normal gradient of the flux on the control volumes faces is used. Thus the diffusive part is discretized by:

$$\left(\frac{\partial \psi}{\partial x}\right)_e = \frac{\psi_E - \psi_P}{x_E - x_P} \tag{5.16}$$

These numerical schemes reflect the way how information is transported through the faces. It is dependent on the ratio between convection and diffusion, i.e. the Peclet number, which is defined as:

$$Pe = \frac{\rho u_i \Delta x_i}{\Gamma} \tag{5.17}$$

If the Peclet number is small, the transport is dominated by diffusion, which transports information equally in all directions. Contrarily if the Peclet number is large, information is transported in the direction of the velocity field. Having a large Pe is undesired, since it

influences the solution convergence very much. The numerical results may contain oscillations due to the fact that while computing the convective term at the note *P* only the values at *E* (east) and *W* (west) nodes are used, but not at the *P* node. Thus, ψ_P can take any value, i.e. oscillations are allowed.

Other than CDS, UDS, and the flux blending schemes there is a large number of interpolation methods, e.g. Quadratic Upwind Interpolation for Convective Kinematics "QUICK", which is third accurate order. Unfortunately it was not used within this work. A recent review on numerical schemes and their performance can be found [80] and [81].

5.1.4 Unsteady term discretization

In this work, the volume integral is approximated by the value in the central of the cell (denote by P) cumulated over the volume. The unsteady term is approximated as:

$$\int_V \frac{\partial \rho\Phi}{\partial t} dV \approx \left(\frac{\partial}{\partial t} \rho\Phi\Delta V \right)_P \tag{5.18}$$

where ΔV is the volume of the CV. To approximate the term in the right hand side, one can use first order scheme

$$\left(\frac{\partial \rho\Phi}{\partial t} \Delta V \right)_P^{n+1} \approx \frac{(\rho\Phi)_P^{n+1} - (\rho\Phi)_P^{n}}{\Delta t} \Delta V \tag{5.19}$$

or second order scheme

$$\left(\frac{\partial \rho\Phi}{\partial t} \Delta V \right)_P^{n+1} \approx \frac{3(\rho\Phi)_P^{n+1} - 4(\rho\Phi)_P^{n} - (\rho\Phi)_P^{n-1}}{2\Delta t} \Delta V_p \tag{5.20}$$

Here, Δt denotes a time interval and the superscripts and $n, n-1$ and $n+1$ are related to the actual, previous and following time steps. The method to evaluate the dependent values (e.g. Φ and Γ_Φ) on which time step can be categorized as explicit scheme

$$\left(\frac{\partial}{\partial t} \rho\Phi\Delta V \right)_P^{n+1} = f^{n}(\Phi, \Gamma_\Phi, \cdots) \tag{5.21}$$

or implicit scheme

$$\left(\frac{\partial}{\partial t} \rho\Phi\Delta V \right)_P^{n+1} = f^{n+1}(\Phi, \Gamma_\Phi, \cdots) \tag{5.22}$$

Explicit schemes are characterized by calculating values of the dependent variables at one time level entirely in terms of values calculated previously, making them relatively easy to implement. However, they tend to require restrictions on the interval of the time step to avoid numerical instability, and this can be expensive in terms of computation time.

Implicit schemes are characterized by calculating values of the dependent variables simultaneously so that a system of equations must be solved at each time level. This leads to complicated code and can also be computationally expensive. However, implicit schemes tend to have much better stability properties than their explicit counterparts and so have been preferred for many commercial applications.

In FASTEST-3D, a hybrid scheme (Crank-Nicholson Scheme) is implemented for solving both the accuracy and the stability problem as:

$$\left(\frac{\partial}{\partial t}\rho\Phi\Delta V\right)_P^{n+1} = \frac{f^{n+1}(\Phi,\Gamma_\Phi,\cdots)+f^{n}(\Phi,\Gamma_\Phi,\cdots)}{2} \tag{5.23}$$

5.1.5 Pressure velocity coupling

The 3D-incompressible non-reactive flow is described numerically by three equations of momentum and the continuity. Thus we have four unknowns (*u, v, w,* and *P*) and four equations (3 for momentum + 1 for continuity). One should mention here, that the density ρ is not considered as variable, because the flow is incompressible. In other words, the density may change due to variations in temperature and concentration of species, but not due to pressure variations ($\partial\rho/\partial p = 0$). The problem is that we do not have any equation for pressure *P*. In case of compressible flow, i.e. Mach number > 0.3, the pressure is deduced by the equation of state. Unfortunately, the flows under investigation are incompressible. Therefore we can use the continuity equation as an indirect equation for the pressure. This method is called the SIMPLE (Semi Implicit Method for Pressure Linked Equation) algorithm.

The SIMPLE algorithm is preceded as follows: first the momentum equations are solved, using an "old" pressure to give u^*, v^*, and w^*. In the following we are going to consider only the *x*-direction with the velocity component u^*, the other two directions can be treated in the same way. The discretized governing equation (5.3) for the u^* velocity component is given by:

$$a_e u_e^* = \sum_{nb} a_{nb} u_{nb}^* + S_{\tilde{u}} + \left(p_W^* - p_P^*\right)\sigma_e \tag{5.24}$$

where $S_{\tilde{u}}$ represents a source term, σ_e the control volume surface in the east face and a_{nb} are the discretization coefficients related to all faces. Now we introduce:

$$u_i^{n+1} = u_i^* + u_i^{cor}, \qquad p^{n+1} = p^* + p^{cor} \tag{5.25}$$

where u_i^* have been obtained from the momentum equations, and p^* was obtained from the previous iteration. u_i^{cor} and p^{cor} are the velocity and pressure correction respectively.

Now, velocities u_i^{n+1} are used (corrected) to solve the continuity equation

$$\sum_i \left(\rho u^{n+1}\sigma\right)_i = 0 \tag{5.26}$$

Then we use the momentum equations to obtain a relation between u_i^{n+1} and p^{cor}:

$$a_e u_e^{n+1} = \sum_{nb} a_{nb} u_{nb}^{n+1} + S_u + \left(p_W^{n+1} - p_P^{n+1}\right)\sigma_e \tag{5.27}$$

where *nb* denotes the neighboring faces. The equation (5.26) provides a relation between u_i^{cor} and p^{cor} as follows:

$$a_P u_P^{cor} = \sum_{nb} a_{nb} u_{nb}^{cor} - \sigma_e \left(p_W^{cor} - p_P^{cor}\right) \tag{5.28}$$

Equation (5.27) necessitates the determination of p^{cor} to calculate the corrected velocities. So we use equation (5.25) and deduce the following expression:

$$a_P p_P^{cor} = \sum_{nb} a_{nb} p_{nb}^{cor} - \underbrace{\sum_{nb}\left(\rho u_i^* \sigma_i\right)}_{b'} \tag{5.29}$$

The object of the pressure correction equation is to satisfy the continuity equation, i.e. to make the term b' in equation (5.28) vanish and thus determine p^{cor}. Once $\left(p_W^{cor} - p_P^{cor}\right)$ is calculated, we can compute the new velocities as follows:

$$u_e^{n+1} = u_e^* - \frac{\sigma_e}{a_e - \sum_{nb} a_{nb}}\left(p_W^{cor} - p_P^{cor}\right) \tag{5.29}$$

The equation (5.29) includes the term $\sum_{nb} a_{nb}$, which is unknown and therefore it will be set to zero in the frame of the SIMPLE method [81]. Other pressure correction method (SIMPLEC) assumes that $\sum_{nb} a_{nb} u_{nb}^{cor} \approx \sum_{nb} a_{nb} u_e^{cor}$ in equation (5.27) to get the equation (5.29).

The solution procedure using the SIMPLE method can be summarized as follows:

1. Guess the pressure p^* (or take it from previous step)
2. Solve the Navier-Stokes equations and get u_i^*
3. Solve the pressure correction p^{cor} (equation (5.28))
4. Correct the velocities and pressure (equations (5.24)and (5.29))
5. Repeat Steps 2-4 till convergence.

5.1.6 Solvers

5.1.6.1 Solution of the linear equation system

The discretization of the governing equations summarized in this section by means of the finite volume procedure explained in the previous sections results in a system of linear algebraic equations each having a form. This system can be written in matrix notation as

$$A\underline{\Psi} = \underline{S} \tag{5.30}$$

where A is the square coefficient matrix built from the coefficients of the linear equations (5.3) for each CV, $\underline{\Psi}$ is a vector containing the values of the variable Ψ in each CV and $\underline{S}$ is the vector containing the terms on the RHS of equation (5.30).

The system has to be solved by means of an efficient solution method. The coefficient matrix A resulting from (5.3) is sparse, i.e. most of its elements are zero and the non-zero elements lie on a small number of well-defined diagonals (in FASTEST-3D seven diagonals). Advantage should be taken from this structure. Since direct methods like Gauss elimination or LU decomposition do not use this advantage, being quite costly, and since discretization errors are normally much larger than the computer accuracy, there is a clear reason to apply an iterative method. Furthermore, the fully implicitly discretized momentum equations are actually non-linear and can not be solved by means of a direct method. The details of their linearization are discussed in the following section. In an iterative method some initial solution is guessed and then systematically improved. One would have after *n* iterations an approximate solution of equation (5.30), $\underline{\Psi}^n$, that is not the exact one. The non-zero residual vector $\underline{r}^n$ (a difference between the left and the right hand side of equation (5.30) satisfies the expression

$$A\underline{\Psi}^n = \underline{S} - \underline{r}^n \tag{5.31}$$

An iterative scheme for the linear system, that should drive the residual to zero, can be written as :

$$M\left(\underline{\Psi}^{n+1} - \underline{\Psi}^n\right) = B - \left(M - N\right)\underline{\Psi}^n \tag{5.32}$$

or

$$M\underline{\delta}^n = \underline{r}^n \tag{5.33}$$

Here, $\underline{\delta}^n = \underline{\Psi}^{n+1} - \underline{\Psi}^n$ is the correction vector which is simultaneously an approximation to the convergence error. Once the computation of $N\underline{\Psi}^n$ is inexpensive and the solution of equation (5.32) converges rapidly the optimal iterative method is found. For rapid convergence in the solution of equation (5.33) the matrix M must be as good an approximation to A as possible. For that purpose the *strongly implicit procedure* (SIP), originally proposed by Stone [82] and further developed for the seven diagonal coefficient matrix by Leister and Peric [83] is applied in FASTEST-3D. In this method the matrix M is chosen to be equal to the incomplete LU decomposition (ILU):

$$M = LU = A + N \tag{5.34}$$

In the ILU decomposition the procedure is the same as in standard LU factorization. But for each zero element of the original matrix A a corresponding element of the lower triangular matrix L or the upper triangular matrix U is set to zero too. Even though L and U have the non-zero elements only on the same diagonals as $A(W,E,S,N,B,T,P)$, their product LU has additional non-zero diagonals (*SE, NW* etc.). Stone [5.3] found that convergence can be improved by allowing *N* to have non-zero elements on the diagonals corresponding to all non-zero diagonals of *LU*. The elements of the matrix *N* must be defined so that the elements of vector $N\underline{\Psi} \approx 0$ and that the matrix *M* to be the best approximation to *A*. This means that the contribution of the terms on the 'additional' diagonals (*SE, NW* etc.) in *N* must be nearly cancelled by the contribution of other diagonals (*W,E,S,N,B,T,P*). Expecting the solution of the elliptic partial differential equations to be smooth, Stone [83] approximated the unknown function values in 'additional' nodes in terms of the known function values at nodes corresponding to the diagonals of *A*.

Finally, one proceeds as follows. Having a matrix *A* the elements of *N* can be found. The elements of *M*, which are the sum of *A* and *N*, do not need to be computed. Instead, the elements of *L* and *U* are found in sequential order for the given *A* and *N*. Once the elements of *L* and *U* are known, the *inner iterations* begin. The system given in equation (5.33) can be rewritten as

$$LU\underline{\delta}^n = \underline{r}^n \tag{5.35}$$

or

$$U\underline{\delta}^n = L^{-1}\underline{r}^n = \underline{R}^n \tag{5.36}$$

Using the advantage of LU decomposition the elements of the vector $\underline{R}^n$ are computed first using equation (5.36) by marching in the order of increasing CV's index (*forward substitution*). Then the elements of the correction vector $\underline{\delta}^n$ are calculated by marching in the order of decreasing CV's index (*backward substitution*). In addition to that the variable values in the CVs are updated following $\underline{\Psi}^{n+1} + \underline{\Psi}^n = \underline{\delta}^n$. The iterations proceed until the sum over all elements of the residual vector $\underline{r}^n$ becomes lower than some given tolerance.

5.1.6.2 Solution of steady and unsteady problems

In steady computations a steady state solution of the governing equation system is sought. In this case the time history is of no interest. One can either neglect the unsteady terms in the

governing equations or iterate until the steady equations are satisfied, or march in time without requiring full satisfaction of the equations at each time step.

The iterations within one time step or during steady computations, in which the coefficient matrices and source vectors in equation (5.3) are updated, are called *outer iterations* in order to distinguish them from the *inner iterations* performed on the linear systems in equation (5.3) with fixed coefficients (in the SIP solver).

The changes in variables after each outer iteration may be significant and particularly at the beginning where they may cause instabilities. In order to reduce this effect the under-relaxation of the variables is applied:

$$\psi^m = \psi^{m-1} + \alpha_\psi \left(\psi^m - \psi^{m-1} \right) \tag{5.37}$$

where ψ^m and ψ^{m-1} are the values of the variable ψ after *m*-th and *(m-1)*st outer iteration, ψ^{new} is the result of solution of equation (5.3) and the under-relaxation factor α_ψ satisfies $0 < \alpha_\psi \leq 1$.

In unsteady computations (LES) the time accuracy is required in order to resolve in time e.g. some periodical process. In this case the iterations must be continued within each time step until the entire system of the governing equations is satisfied to within a narrow tolerance.

5.2 Handling of Variable density

With regard to numerical implementation of reactive flows, an important problem is how to include the variable density in an incompressible flow solver where the weak density coupling exists. The procedure for this coupling may differ from solver to solver based on the type of numerical procedure used. Improper inclusion of the variable density can lead to false results. Different procedures are proposed for the explicit procedure based numerical solvers [84, 85] and semi-implicit ones [86]. In the present work an implicit solver is used, and therefore developed and applied an adequate variable density approach. For this purpose a equation for the divergence of the velocity field is developed by using equations (4.23a), (4.23b) and (2.21). By substituting $\overline{\rho}\widetilde{C}$ of equation (4.23b) in to equation (4.23a) on can get the following equation.

$$\frac{\partial}{\partial t}\left(\frac{\rho_u - \overline{\rho}}{\tau} \right) + \nabla \cdot \left(\tilde{u} \frac{\rho_u - \overline{\rho}}{\tau} \right) = \nabla . \left[\left(\rho_u \frac{S_L \Delta_C}{16\sqrt{6/\pi}} + \frac{\mu_t}{Sc_t} \right) \nabla . \widetilde{C} \right] + 4\rho_u S_L \Xi \sqrt{6/\pi} \frac{\widetilde{C}(1-\widetilde{C})}{\Delta_C} \tag{5.38}$$

Let us consider the unsteady term (first term on l.h.s). this term can be rewritten as:

$$\frac{\partial}{\partial t}\left(\frac{\rho_u-\overline{\rho}}{\tau}\right)=\frac{\partial}{\partial t}\frac{\rho_u}{\tau}-\frac{\partial}{\partial t}\frac{\overline{\rho}}{\tau} \tag{5.39}$$

The first term on the r.h.s is zero for the pure premixed flame case: as ρ_u and τ are constants. Now equation (5.39) can be written as

$$\frac{\partial}{\partial t}\left(\frac{\rho_u-\overline{\rho}}{\tau}\right)=-\frac{\partial}{\partial t}\frac{\overline{\rho}}{\tau} \tag{5.40}$$

Now the second term, i.e. convection term, is reformulated as

$$\nabla\cdot\left(\tilde{u}\frac{\rho_u-\overline{\rho}}{\tau}\right)=\tilde{u}\left(\nabla\frac{\rho_u}{\tau}\right)-\left(\nabla\frac{\overline{\rho}\tilde{u}}{\tau}\right)+\frac{\rho_u}{\tau}\nabla\tilde{u} \tag{5.41}$$

As explained above for the pure premixed case $\nabla\frac{\rho_u}{\tau}$ is zero. Now the equation (5.42) can be written as:

$$\nabla\cdot\left(\tilde{u}\frac{\rho_u-\overline{\rho}}{\tau}\right)=-\left(\nabla\frac{\overline{\rho}\tilde{u}}{\tau}\right)+\frac{\rho_u}{\tau}\nabla\tilde{u} \tag{5.42}$$

By combining equations (5.39) and (5.40) l.h.s of equation becomes:

$$\frac{\partial}{\partial t}\left(\frac{\rho_u-\overline{\rho}}{\tau}\right)+\nabla\cdot\left(\tilde{u}\frac{\rho_u-\overline{\rho}}{\tau}\right)=-\left(-\frac{\partial}{\partial t}\frac{\overline{\rho}}{\tau}+\nabla\frac{\overline{\rho}\tilde{u}}{\tau}\right)+\frac{\rho_u}{\tau}\nabla\tilde{u} \tag{5.43}$$

By using continuity equation (2.21), first part on the r.h.s of the equation (5.43) becomes zero for the pure premixed case as τ is constant. So, now combining the equations (5.38) and (5.43) an equation for the divergence of the velocity is derived.

$$\nabla\tilde{u}=\frac{\tau}{\rho_u}\left[\nabla.\left[\left(\rho_u\frac{S_L\Delta}{16\sqrt{6/\pi}}+\frac{\mu_t}{Sc_t}\right)\nabla.\widetilde{C}\right]+4\rho_u S_L\Xi\sqrt{6/\pi}\,\frac{\widetilde{C}(1-\widetilde{C})}{\Delta}\right] \tag{5.44}$$

In the numerical procedure, the time derivative of the density was updated by using the relation equation (5.44) and the continuity equation (2.21). Here the second term of the equation (2.21) is written in vectorial form as $\overline{\rho}\nabla\tilde{u}+\tilde{u}\nabla\overline{\rho}$. The above expression is derived for the flame surface density approach. Nevertheless density is still related with the progress variable only. For artificial thickened model (see equation (4.28)) derivation of the divergence of velocity similar and is given by the equation (5.45).

$$\nabla\tilde{u}=\frac{\tau}{\rho_u}\left[\nabla\cdot\left(\overline{\rho}DE_F F\nabla\tilde{c}\right)+\frac{A}{F}E_F\overline{\rho}(1-\tilde{c})\exp\left(-\frac{E_a}{RT}\right)\right] \tag{5.45}$$

5.3 Boundary conditions

5.3.1 Inlet boundary conditions

The inlet boundary conditions for the velocity components (momentum) as well as other scalar variables like temperature and concentration are set by means of Dirichlet boundary condition. This is the simplest method to deal with the inflow conditions. However this approach can lead to large coherent structures instead of turbulence. This type of treatment neglects the turbulent fluctuations but reasonable if the inflow is far upstream of the area of interest or if all the relevant fluctuations develop inside the computational domain. In the present study, which is related to the premixed combustion cases, all the fluctuations are developed after the bluff body (see Fig. 6.29). In this case along with the Dirchlet condition some random noise is introduced at the inlet.

5.3.2 Wall boundary conditions

The velocities in grid nodes conjoined with the wall are set equal to the wall movement. In the frame of this work they are set to zero in the tangential as well as in the normal direction, because the wall is fixed. This condition is also valid for the turbulent quantity k_{sgs}. Nevertheless in order to handle the flame-wall interactions, progress variable is treated by using two-zone approach as explained in section 4.4.3.

5.3.4 Periodic boundary conditions

The periodic boundary conditions (between boundary I and II) make the variables at the *boundary I* equal the variables at the *boundary II* conforming to the following equation.

$$\psi(\vec{r}) = \psi(\vec{r} + \vec{L}) \tag{5.45}$$

where $\vec{r}$ is the position vector and $\vec{L}$ is the periodic length vector of the domain considered. The periodic boundary condition corresponds to zero flux. Making the boundaries periodic means inflow through one of the boundaries equal the outflow through the other. In the present study for the simulation of fully developed channel flows and rotating channel flows this boundary condition is used in the streamwise and spanwise directions of the domain. For the premixed combustion case, i.e., bluff-body stabilized flame, this condition is used in the span wise direction.

5.3.5 Outlet boundary condition

A convective outlet boundary condition is used for the premixed combustion case. In general a convective outlet boundary condition is defined by using

$$\frac{\partial \phi}{\partial t} + U_C \frac{\partial \phi}{\partial n} = 0 \tag{5.46}$$

where U_C is the convective velocity, ϕ represents any velocity component or scalar and n represents the direction normal to the boundary. This velocity is calculated by using equation (5.44). By applying Gauss theorem to equation (5.44) one can get the following relation for the present case as:

$$U_C * (outflow\_surface) - \int_S u_{inlet} ds = \int_v \frac{\tau}{\rho_u} \left[\begin{array}{l} \nabla . \left[\left(\rho_u \frac{S_L \Delta}{16\sqrt{6/\pi}} + \frac{\mu_t}{Sc_t} \right) \nabla . \widetilde{C} \right] \\ +4\rho_u S_L \Xi \sqrt{6/\pi} \frac{\widetilde{C}(1-\widetilde{C})}{\Delta} \end{array} \right] dv \tag{5.47}$$

The above relation allows then to calculate the convective outlet velocity U_C. In order to fulfil the mass conservation through out the system, equation (5.44) will be further used for correcting the velocities which are calculated by the equation (5.46). For this, two types of methods are used. One is additive correction and the other is a multiplicative one. For open boundaries additive correction provides good results where as for the wall bounded flows multiplicative correction is known to give better results. For the present study, LES of premixed combustion case, multiplicative correction technique is used.

Chapter 6

Results and Discussion

In this chapter, some applications of the derived LES code to the simulation of non-reactive flows and premixed combustion are presented. In the first part LES of channel flow simulations are presented by considering different SGS models. In the second part of LES of rotating channel flow simulations presented by considering the Lagrangian dynamic model and anisotropic one equation dynamic model. In the last part LES of the bluff-body stabilized premixed flame by considering flame surface density and thickened flame model are presented.

6.1 LES of fully developed 3-D channel flow simulations

In this section LES of channel flows are presented by considering different SGS models. Initially the following studies are performed for the clear understanding of these models.

- Influence of the filter widths on the simulations are studied by considering the Smagorinsky model.
- Robustness of the dynamic model is studied.
- Comparisons between different dynamic procedures are performed.
- Understanding the mixed model.
- Comparisons between one equation models have been performed.

Finally comparisons between selected models are presented.

All these simulations were performed first on a fully developed turbulent channel flow at Reynolds number 395 based on the friction velocity and half-width of the channel. The two walls of the channel are treated as no-slip boundaries. In the streamwise and spanwise directions of the domain is truncated to a finite size and periodic boundary conditions are imposed. For the present case the domain size of $2\pi\delta \times \pi\delta \times 2\delta$ in the streamwise, spanwise and wall-normal has been considered. Simulations are carried out on a coarse grid with cells 64×32×32. All these models are compared with the DNS data of AGARD test case PCH10 [87].

6.1.1 Influence of the filter widths on the Smagorinsky model

Despite many disadvantages, mentioned in section 3.2.1.1, the Smagorinsky model is a very commonly used SGS model in the LES community. The main advantages of this model are less computational effort and easy implementation. Due to this reason it is useful to study the behavior of this model under the influence of different filter widths. In general these filter widths are calculated by using different filter width formulas mentioned in the section 3.2.1.1. Equation (3.5) gives the formula based on volume of the grid cell (Vol: case1), equation (3.6) gives the formula based on area of the sides of the grid cell (Area: case2) and where as equation (3.7) gives the formula for filter width based on the anisotropic extension of the volume of grid cell (Ani: case3). Comparison between obtained normalized mean velocity and normalized Reynolds stress profiles (normal to the wall) are shown in the Fig. 6.1 and Fig. 6.2. All the results are normalised by the friction velocity.

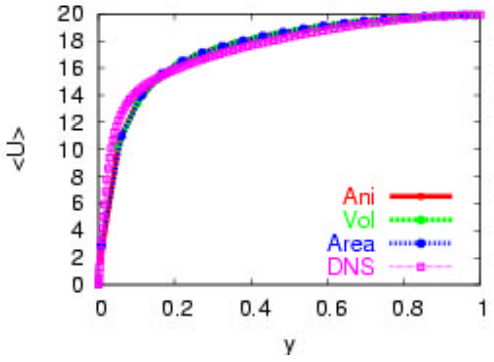

Figure 6.1 Comparison between normalized mean velocity profile <u>

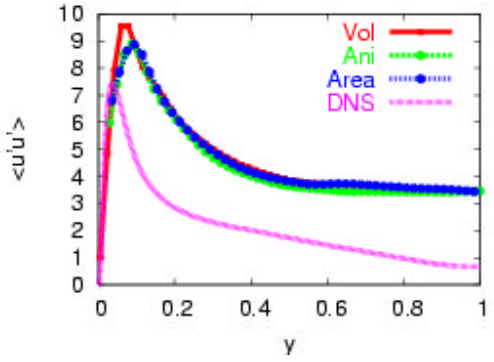

Figure 6.2 Comparison between normalized Reynolds stress profile <u´u´>

It is very clear from Fig. (6.2) that all the models over predicts the normalized Reynolds stress profile. Nevertheless case1 give a bad result compared to other cases. Main reason for this behavior is the filter width found by the volume is unrealistic as towards wall grid cells become of pencil type. This behavior is improved by considering the anisotropic correction to the filter width (case 3). Nevertheless it clear that overall performance of the Smagorinsky model is bad. This performance of the model is improved by considering the damping function give by van Driest [3.6]. But this correction is not considered for the present study.

6.1.2 Robustness of the dynamic Germano-Lilly model

To investigate the robustness of the Germano-Lilly (section 3.2.2.1) model four different cases are considered. These are without variation of the dynamically predicted model coefficient

(germ) and three different externally varied model coefficients C/2(germ/2), C/4(germ/4) and 2×C(germ*2) respectively. In Fig. 6.3 and 6.4 it has been clearly shown that the variations in the results are negligible due to the external imposed variation.

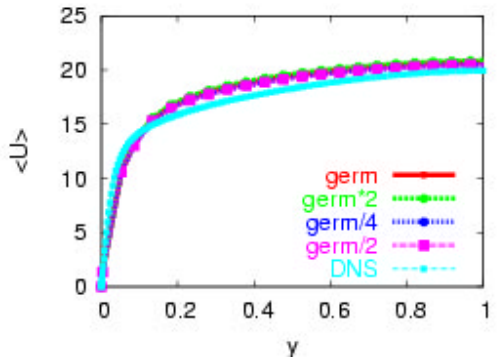

Figure 6.3 Comparison between normalized mean velocity profile <u>

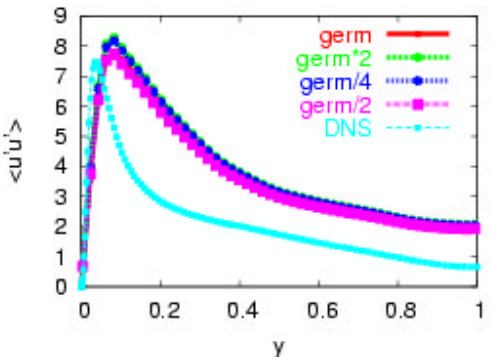

Figure 6.4 Comparison between normalized Reynolds stress profile <u´u´>

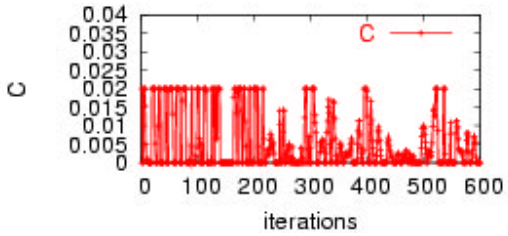

Figure 6.5 Variation of the Germano-Lilly model coefficient (germ/2)

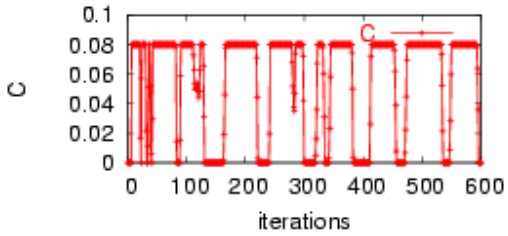

*Figure 6.6 Variation of the Germano-Lilly model coefficient (germ*2)*

But on the other hand variation of the model coefficients is very different as shown in the Fig. 6.5 and Fig. 6.6. This shows the robustness of the model under critical conditions. To explain these phenomena two different possible scenarios can be considered. One is scale similarity assumption and other one is scale dependent situation.

6.1.2.1 Scale similarity assumption

Let us consider a simple case where we are imposing the external variation as C/2 to equation (3.17). This can be reformulated as:

$$\frac{C}{2}=\frac{L_{ij}M_{ij}}{2M_{ij}M_{ij}}=\frac{L_{ij}(2M_{ij})}{(2M_{ij})(2M_{ij})} \tag{6.1}$$

In the above expression $2M_{ij}$ can be expressed as:

$$2M_{ij}=-2\left(\sqrt{2}\tilde{\bar{\Delta}}\right)^2\left|\tilde{\bar{S}}\right|\tilde{\bar{S}}_{ij}+\widetilde{2\left(\sqrt{2}\bar{\Delta}\right)^2\left|\bar{S}\right|\bar{S}_{ij}} \tag{6.2}$$

here factor 2 has been brought inside the expression. The above expression can be reformulated with modified test filter width $\tilde{\bar{\Delta}}_{mt} = \sqrt{2}\tilde{\bar{\Delta}}$ and grid filter width $\bar{\Delta}_m = \sqrt{2}\bar{\Delta}$.

$$2M_{ij} = -2\left(\widetilde{\bar{\Delta}_{mt}}\right)^2 \left|\tilde{\bar{S}}\right| \tilde{\bar{S}}_{ij} + \widetilde{2\left(\bar{\Delta}_m\right)^2 \left|\bar{S}\right| \bar{S}_{ij}} \tag{6.3}$$

By using scale similarity assumption one reformulate the above expression as:

$$2M_{ij} = -2\left(\widetilde{\bar{\Delta}_{mt}}\right)^2 \left|\tilde{\bar{S}}\right|^{mt} \tilde{\bar{S}}_{ij}{}^{mt} + \widetilde{2\left(\bar{\Delta}_m\right)^2 \left|\bar{S}\right|^{m} \bar{S}_{ij}{}^{m}}^{mt} \tag{6.4}$$

Here by following scale similarity we have assumed that $\tilde{\bar{S}}_{ij}{}^{mt} = \tilde{\bar{S}}_{ij}$, $\bar{S}_{ij}{}^{m} = \bar{S}_{ij}$ etc. Finally one can rewrite the above expression as:

$$M_{ij}^{m} = -2\left(\widetilde{\bar{\Delta}_{mt}}\right)^2 \left|\tilde{\bar{S}}\right| \tilde{\bar{S}}_{ij} + \widetilde{2\left(\bar{\Delta}_m\right)^2 \left|\bar{S}\right| \bar{S}_{ij}} \tag{6.5}$$

Here one can understand only modified filter widths but not the modified the filtered quantities. Similarly the term L_{ij} can be reformulated and is straight forward. Due to similarity assumption original L_{ij} is retained. Finally resultant dynamic coefficient can be shown as:

$$\frac{C}{2} = \frac{L_{ij} M_{ij}^{m}}{M_{ij}^{m} M_{ij}^{m}} \tag{6.6}$$

This resultant dynamic coefficient can be calculated directly by using grid filter $\sqrt{2}\bar{\Delta}$ and test filter $\sqrt{2}\tilde{\bar{\Delta}}$ with implicit LES. Nevertheless this can be true only when scale similarity assumption is valid.

6.1.2.2 Scale Dependent case

With this type of assumption one cannot reformulate the equation (6.2) to equation (6.4) as $\tilde{\bar{S}}_{ij}{}^{mt} \neq \tilde{\bar{S}}_{ij}$, $\bar{S}_{ij}{}^{m} \neq \bar{S}_{ij}$ etc. if we consider $\tilde{\bar{S}}_{ij}{}^{mt} = \tilde{\bar{S}}_{ij}$, $\bar{S}_{ij}{}^{m} = \bar{S}_{ij}$ etc.., then we are introducing the physical error. But in channel flow simulations one can have scale dependent situations in many places inside the computational domain. But results show that external variation has no significant effect on the simulation results. Possible explanation for these results is that total error, which is nothing but summation of numerical and physical error, is not changed. This implies additional physical error is compensated by the some additional numerical error. Nevertheless it is very difficult to differentiate physical and numerical errors in a simulation in the case of implicit LES method. On the other hand one can study the behaviour of physical and

numerical error by using explicit LES method but this is not considered in this work. The above two explanations give some reason for the robustness of the dynamic model and which enables better prediction of the local turbulent statistics. Nevertheless one has to understand that the overall behaviour of the model can be improved by using better SGS models like Lagrangian dynamic model.

6.1.3 Comparison between different dynamic models

For this purpose three different dynamic models are considered. These models are the Germano model, the localized dynamic model (section 3.2.2.2) and the Lagrangian dynamic model (section 3.2.2.3).

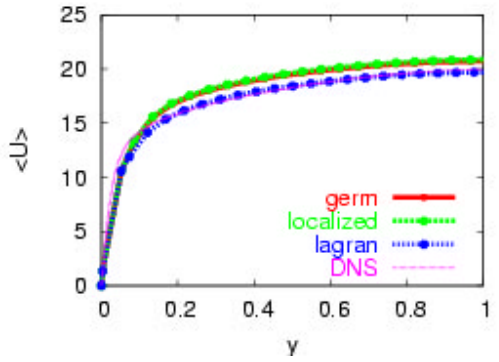

Figure 6.7 *Comparison between normalized mean velocity profile <u>*

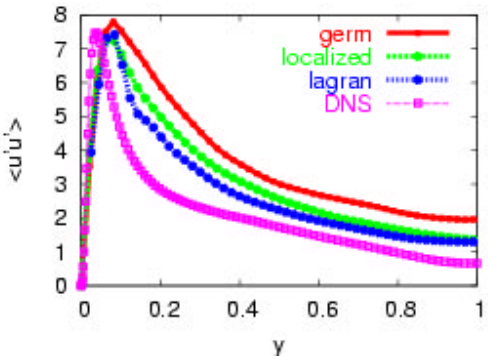

Figure 6.8 *Comparison between normalized Reynolds stress profile <u´u´>*

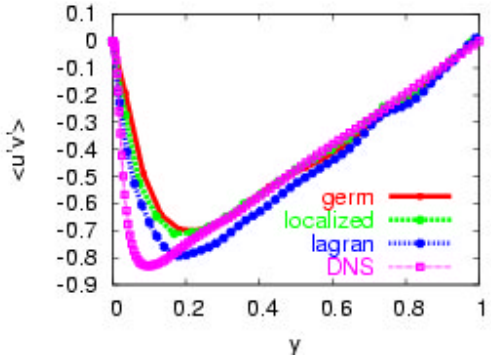

Figure 6.9 *Comparison between normalized Reynolds stress profile <u´v´>*

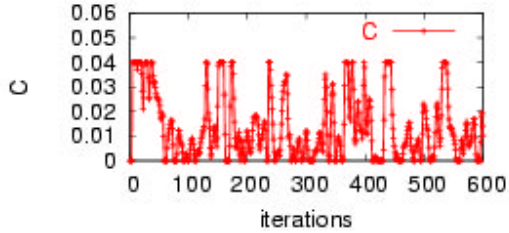

Figure 6.10 *Variation of the Lagrangian model coefficient*

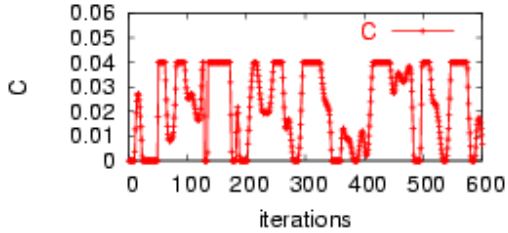

Figure 6.11 *Variation of the localized model coefficient*

Comparison between the obtained normalized mean velocity and normalized Reynolds stress profiles (normal to the wall) are shown in the Fig. 6.7, Fig. 6.8 and Fig. 6.9. All the results are normalised by the friction velocity. Variation of the model coefficient for Lagrangian and localized dynamic model are shown in the Fig. 6.10 and Fig. 6.11. The overall behaviour of these models in comparison with Smagorinsky model is good. But all these models give different results and show the influence of different dynamic procedures on simulations. All these simulations are done without taking any average along the homogeneous direction. The main reason behind this is to test the models under the real conditions where no homogeneous direction exists. Nevertheless the Lagrangian model behaves better compared to the other dynamic models. Main reason behind this behaviour is the averaging performed in time by considering the fluid particle history along its path line. This is more reasonable compared to other types of averaging procedures which are working in spatially local fashion. The computational overhead in the Lagrangian dynamic model is about 10% above the CPU requirements of the other dynamic models

6.1.4 Comparison between mixed models

For this purpose three different models are considered. These models are dynamic mixed model with 0.4 times (mix1p) the scale similarity model (equation (3.53)) and dynamic mixed model with 0.6 times (mix) the scale similarity model (section 3.2.5). Comparison between obtained normalized mean velocity and normalized Reynolds stress profiles (normal to the wall) are shown in the Fig. 6.12, Fig. 6.13 and Fig. 6.14. All the results are normalised by the friction velocity. Variations of the model coefficient for dynamic mixed model are shown in Fig. 6.15 and Fig. 6.16 case mix and mix1p.

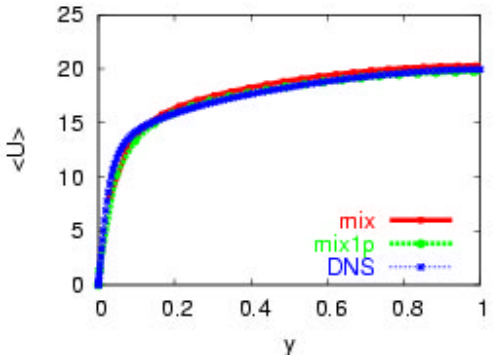

Figure 6.12 Comparison between normalized mean velocity profile <u>

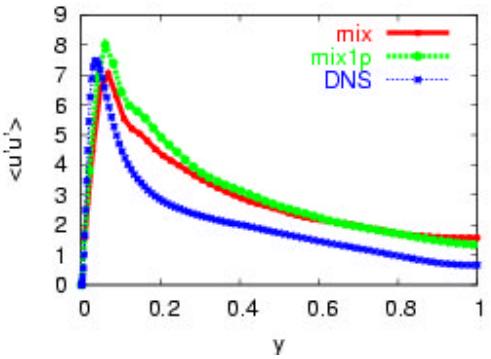

Figure 6.13 Comparison between normalized Reynolds stress profile <u´u´>

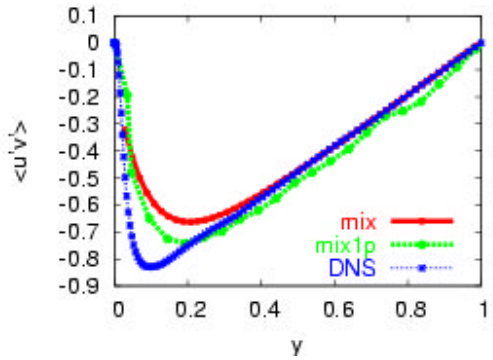

Figure 6.14 *Comparison between normalized Reynolds stress profile <u´v´>*

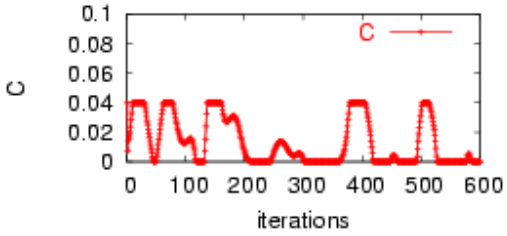

Figure 6.15 *Variation of the model coefficient with less contribution scale similarity term*

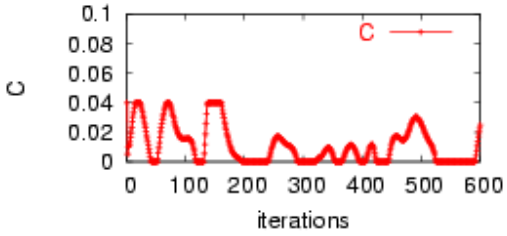

Figure 6.16 *Variation of the model coefficient with more contribution scale similarity term*

In mixed models the contribution of the Smagorinsky model is less. It was found that the scale similarity part without any relaxation gives bad results [6.2]. This is mainly because the model does not provide enough dissipation. There are two ways to overcome this problem. One is by using upwind discretisation schemes and the other one is relaxing the scale similarity part. Among these remedies first one is not preferred as LES codes employ energy conserving schemes where numerical dissipation is almost negligible or does not exist. So the better technique is to relax the scale similarity term. By relaxing the scale similarity part, the contribution of the Smagorinsky model increases as shown in Fig. 6.15 and Fig. 6.16 with variation of the model coefficient. With decreasing of the contribution of the scale similarity part, mixed model approaches the dynamic Smagorinsky model. Nevertheless the overall behaviour of the mixed model is very good compared to Germano-Lilly dynamic Smagorinsky model. The performance of the mixed model can be further improved by using Lagrangian dynamic procedure but this is not considered in this work. But the disadvantage with this model is the additional computational effort, which is 1.5 times the Germano-Lilly dynamic Smagorinsky model. This is mainly because of the additional filtering operations involved in the mixed model.

6.1.5 Comparisons between one equation models

For this purpose two different one equation models are considered. One is based on the isotropic formulation (one) (section 3.2.2.4) and the other one is based on the anisotropic formulation (aniso) (3.2.3.1). Comparison between obtained normalized mean velocity and normalized Reynolds stress profiles (normal to the wall) are shown in the Fig. 6.17, Fig. 6.18 and Fig. 6.19. From these results it becomes very clear that the one equation models can predict better results compared to the previously presented models. In addition, these models are capable of predicting the backscatter. Comparision between forward scatter and the back scatter are presented in Fig. 6.20 and Fig. 6.21 are evaluated by using following expression:

$$P^{+} = \frac{1}{2}\left(P_{ksgs} + \left|P_{ksgs}\right|\right) \ , \ P^{-} = \frac{1}{2}\left(P_{ksgs} - \left|P_{ksgs}\right|\right) \tag{6.7}$$

The computational overhead in the isotropic model is about 1.6 times and in the anisotropic model 2 times the CPU requirements of the Germano-Lilly dynamic model. But the main advantage of these models is that they can be used with the very coarse grids as k_{sgs} don't exactly represent the subgrid-scale energy. It also contains some part of the kinetic energy of large eddies. This part is mainly responsible for the interaction between the large and small scales, and the influence of the large scale on the small scales. With the coarsening of the grid one has to model properly the influence of the large scale eddies on the small eddies. So, with one equation models one can properly simulate the flow field even with coarse grids, which gives the justification for the computational overhead. Nevertheless from Fig. 6.17, Fig. 6.18 and Fig. 6.19 it is clear that isotropic one equation model is little diffusive. This is rectified by using anisotropic model.

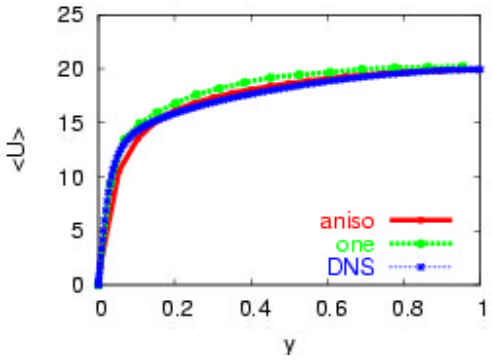

Figure 6.17 Comparison between normalized mean velocity profile <u>

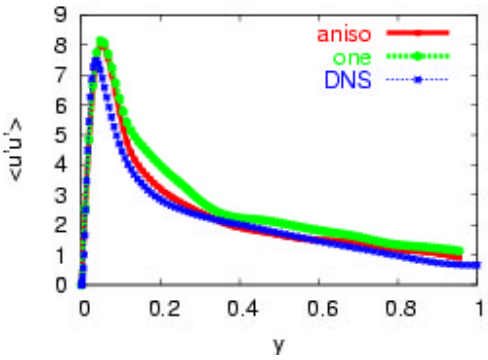

Figure 6.18 Comparison between normalized Reynolds stress profile <u´u´>

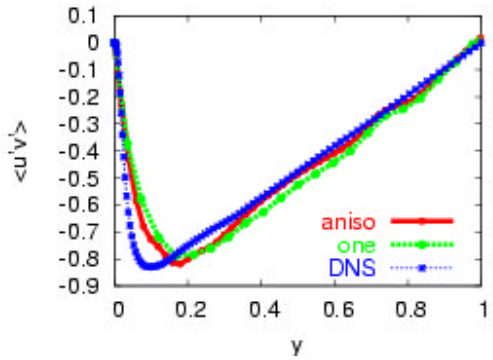

Figure 6.19 Comparison between normalized Reynolds stress profile <u´v´>

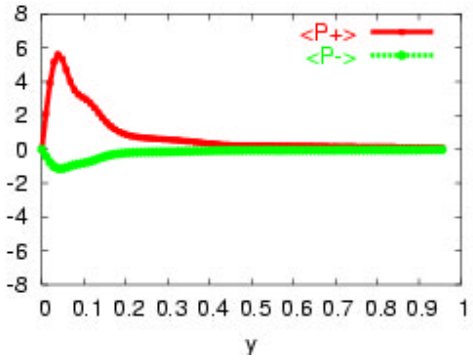

Figure 6.20 Comparison between forward and backward scatter

Figure 6.21 Comparison between forward and backward scatter

6.1.6 Comparisons between selected models

For this purpose the Smagorinsky model with an anisotropic filter width, the Lagrangian dynamic model, the mixed model and the anisotropic dynamic one equation model are considered. Comparison between obtained normalized mean velocity and normalized Reynolds stress profiles (normal to the wall) are shown in the Fig. 6.22, Fig. 6.23 and Fig. 6.24.

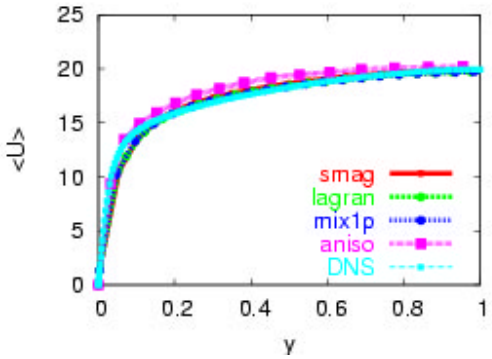

Figure 6.22 Comparison between normalized mean velocity profile <u>

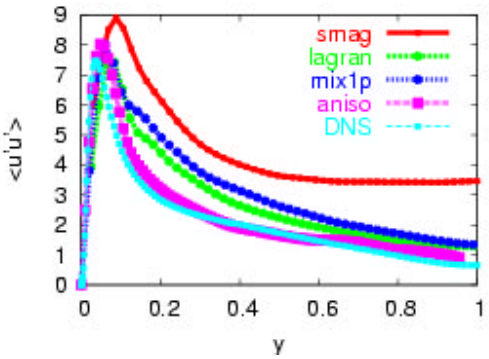

Figure 6.23 Comparison between normalized Reynolds stress profile <u´u´>

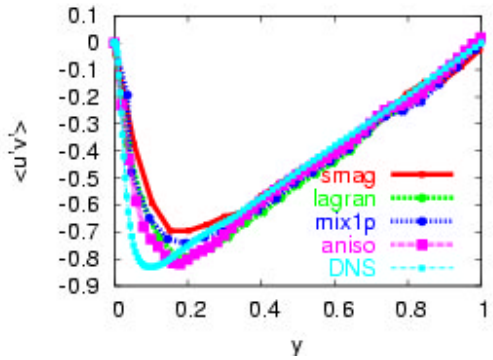

Figure 6.24 Comparison between normalized Reynolds stress profile <u´v´>

From these results it is very clear that the anisotropic one equation model out performs the other models. But as it is mentioned before, anisotropic model causes more computational over head and is very difficult to implement. Lagrangian dynamic model provides a better compromise between computational effort and performance. Mixed model performs almost like Lagrangian dynamic model. But this model performance can be improved by using the Lagrangian dynamic procedure. Even though Smgorinsky model is very simple it performance is not encouraging. Nevertheless as mentioned in the section 6.1.2, dynamic procedures are robust. For simulating complex geometries this robustness is very useful. So it is very clear that Lagrangian dynamic model and anisotropic one equation model give good results. So these two models are considered for the rotating channel flow simulations.

6.2 LES of rotating channel flow

For the second test case fully developed spanwise rotating channel (Fig. 6.25) has been considered. Rotating channel flow is an attractive test for subgrid-scale models because system rotation has some important effects on turbulence: for instance, it inhibits energy transfer from large to small scales; this leads to a reduction in turbulence dissipation and a decrease in the decay rate of turbulence energy. Furthermore, the turbulence length scales along the rotation axis increase relative to those in non-rotating turbulence. The presence of mean shear normal to the axis of rotation may have either a stabilizing or a destabilizing effect, depending on whether the angular velocity and mean shear have the same or opposite signs.

For this case computational domain of $4\pi\delta \times 4\pi\delta/3 \times 2\delta$ in the streamwise, spanwise and wall-normal with grid size of 48×51×64 is considered. For the simulation of rotating channel flow a source is added to the Navier-Stokes equation (2.2) as shown in equation (6.8).

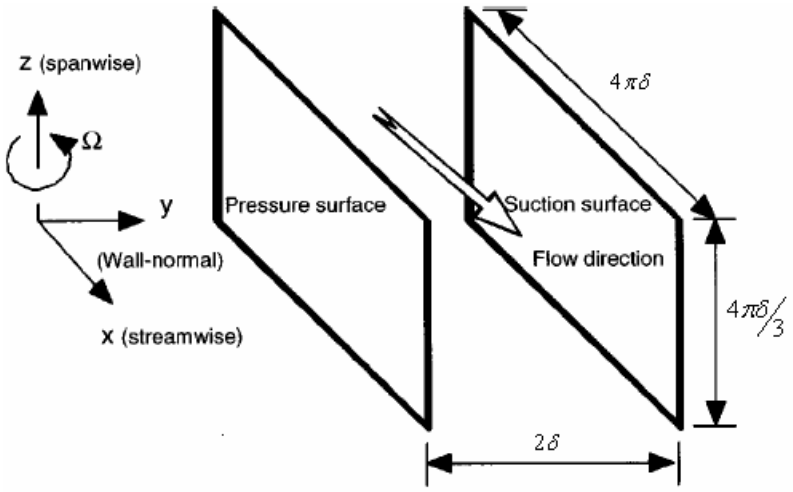

Figure 6.25 *Spanwise rotating channel*

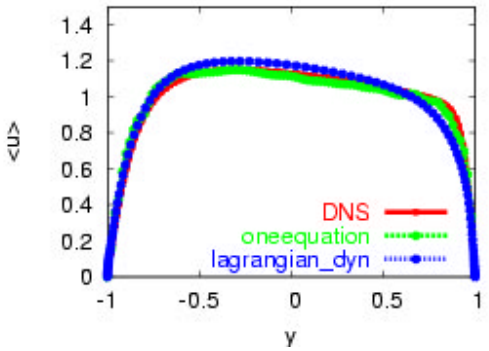

Figure 6.26 *Comparison between normalized mean velocity profile <u>*

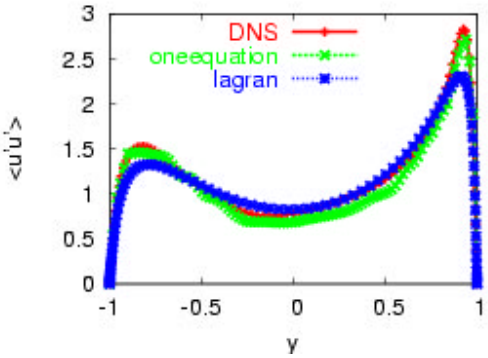

Figure 6.27 *Comparison between normalized Reynolds stress profile <u´u´>*

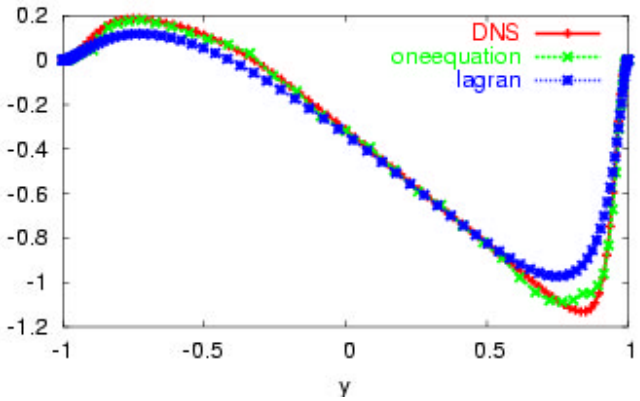

Figure 6.28 *Comparison between normalized Reynolds stress profile <u´u´>*

$$\frac{\partial\left(\overline{\rho}\overline{u_i}\right)}{\partial t}+\frac{\partial\left(\overline{\rho}\overline{u_j}\overline{u_i}\right)}{\partial x_j}=-\frac{\partial\overline{p}}{\partial x_i}+\frac{\partial}{\partial x_j}\left(\overline{\rho}\nu\left(\frac{\partial\overline{u_j}}{\partial x_i}+\frac{\partial\overline{u_i}}{\partial x_j}\right)-\overline{\rho}\overline{u_i'u_j'}\right)+2\varepsilon_{ij3}\Omega\overline{u}_j \tag{6.8}$$

where ε_{ijk} is Levi-Civita's alternating tensor and the Ω angular velocity of the system. The axis of rotation is in the positive z, or x3 direction.

Periodic boundary conditions are applied in the streamwise and spanwise directions, and no-slip conditions at the solid walls.

Reynolds number and rotation number are 177 and 0.144 respectively, which are based on the friction velocity and half-width of the channel. Results are compared to that obtained with the DNS results of AGARD test case PCH21 [87]. Comparison between the obtained mean velocity and Reynolds stress profiles are shown in the Fig. 6.26, Fig. 6.27 and Fig. 6.28. It can be seen that anisotropic model predicts better results compared to the Lagrangian dynamic model. But nevertheless Lagrangian dynamic model also predicts good results. The anisotropic model is able to predict flow phenomena on the both sides of the channel flow, i.e., suction side and pressure side. This shows the applicability of the anisotropic model. Nevertheless the Lagrangian dynamic model also gives reasonable results. But as pointed earlier Lagrangian dynamic model provides a better compromise between computational effort and performance for this case also. Due to this reason this model is considered for the simulation of premixed flames.

6.3 Numerical simulations of premixed flame

In this section numerical simulations of premixed flames are presented.

6.3.1 Experimental set up of a turbulent lean premixed propane/air flame

To assess the performance of both flame surface density and artificial thickened model approaches, simulations of premixed flames have been compared to an experimental flame. This experiment was conducted in Volvo Aero Corporation [89], and named as VR–1. In this thesis work, one of VR–1 lean premixed flames is chosen to be simulated. It is a bluff body stabilized lean propane/air turbulent premixed flame, which is schematically shown in Fig. 6.29. The combustion chamber is a simple rectangular channel with a channel height of 120 mm and width of 240 mm. The propane/air mixture has an equivalence ratio of 0.6 and inlet temperature 600K. The mixture enters the chamber from left at a mass flow rate 0.6 kg/s. The unstretched laminar

flame speed is S_L =0.76 m/s [90]. The flame holder is of prismatic triangular shape, with the side length H=40 mm. The inflow velocity is about 36 m/s with a Reynolds number about 85000 based on the inflow condition and height of the combustion chamber.

The velocity, temperature, and mole fractions of species O_2, CO_2 were measured using Laser Doppler Anemometry (LDA) and gas analysis equipment. Details about the experiment can be found in Sjunnesson et al. [89]. Based on the measurement data and the laminar flame calculation it has been found that the flame is in the corrugated flamelet regime, with a Karlovitz number about 0.1–0.7.

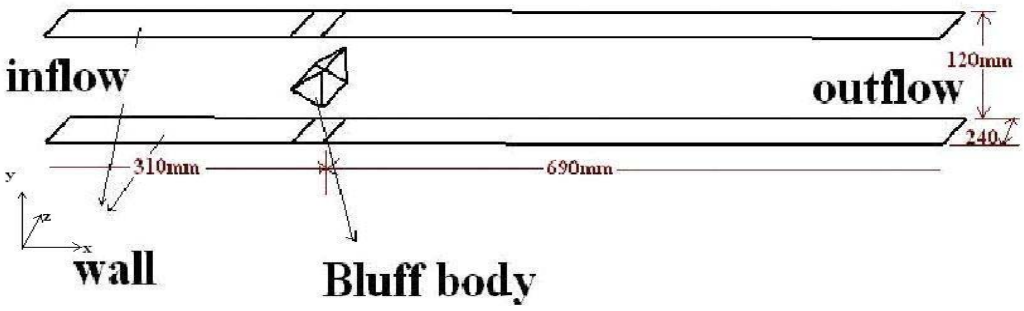

Figure 6.29 *Bluff body test configuration (VR–1)*

6.3.2 Boundary conditions and grid resolution

No-slip boundary condition is applied along all solid walls. For scalars, such as progress variable *C*, zero-gradient condition is generally used. But in this study two-zones approach explained in section 4.4.3 is used. In general for the case of artificial thickened model this type of treatment is not necessary. This is mainly because Arrhenius law which can handle flame-wall interactions is used. For this purpose detailed information regarding the surface reactions is required. But in the present case only global one step reaction is considered and the flame-wall interactions are handled by the proposed approach, i.e. two-zone approach is used. A mass-conserving convective outflow condition is applied (see Section 5.3.5). Some random noise is introduced at the inlet along with the axial velocity 36 m/s. Periodic boundary condition is applied along the spanwise direction.

Due to the limitation of the computational resource and the large computation domain of VR–1 case, very fine grid resolution is not affordable. By comparing the convergence of the mean temperature and mean flow velocities with respect to the refinement of grid resolution, it was

shown that the grid with (after bluffbody) 148, 71, 72 grid points in the streamwise, spanwise and transverse directions, respectively, is satisfactory.

6.3.3 Results obtained by using flame surface density

In this section large eddy simulation of the bluff-body stabilized flame by using flame surface density are presented. For this purpose the algebraic formulation for the flame surface density is used (see section 4.2.2.4). In Fig. 6.30, mean axial velocity and stream lines contours are showed. Fig. 6.31 shows the mean streamwise velocity distribution along the centre line. It is shown that a large size reverse flow zone is attached to the flame holder, which is good for flame stabilization. The predicted length of central circulation zone is about two times of flame holder width, which is shorter than the experimental result. So from these results it was clear that velocity is over-predicted and the recirculation length is under-predicted. The profiles of the mean streamwise velocity at two different transverse stations, where LDA measurement data are available, are shown in Figure 6.32 and 6.33. The overall agreement between experimental and computational results is good.

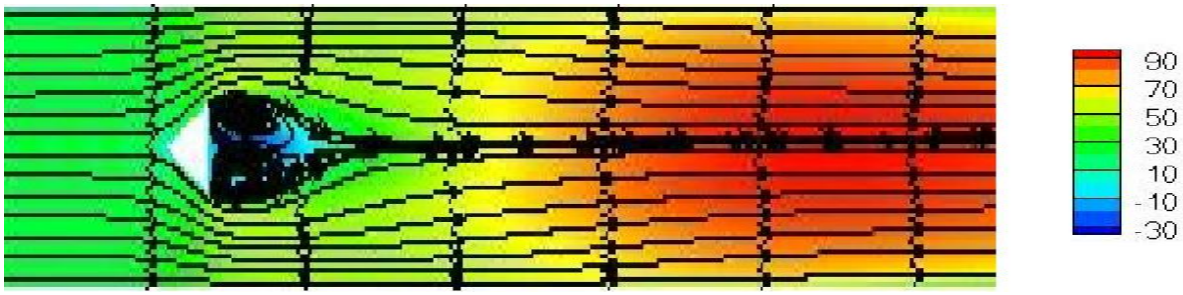

Figure 6.30 Mean axial velocity and stream lines contours

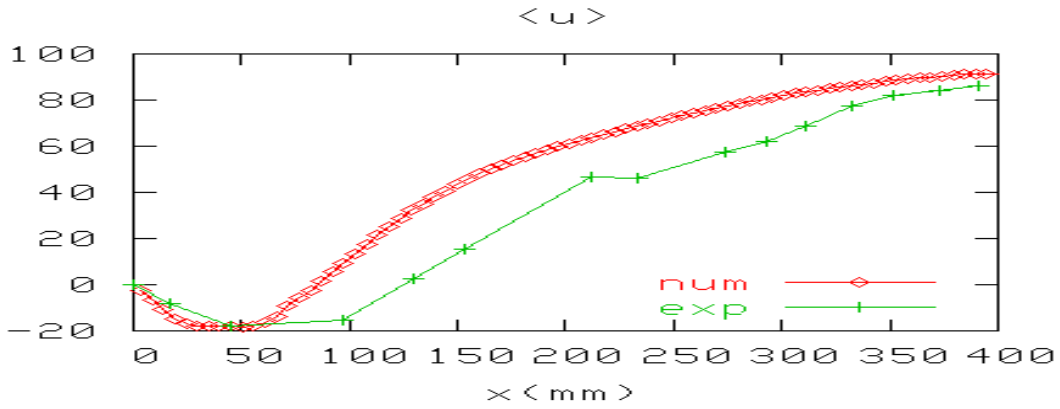

Figure 6.31 Axial velocity prediction along the centreline in the stream-wise direction

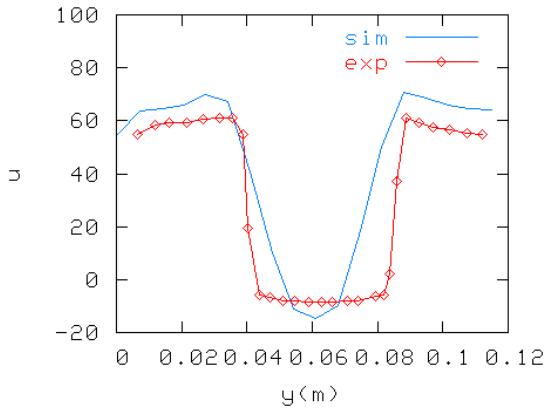

Figure 6.32 *Mean streamwise velocity profile at 0.015m after bluff-body*

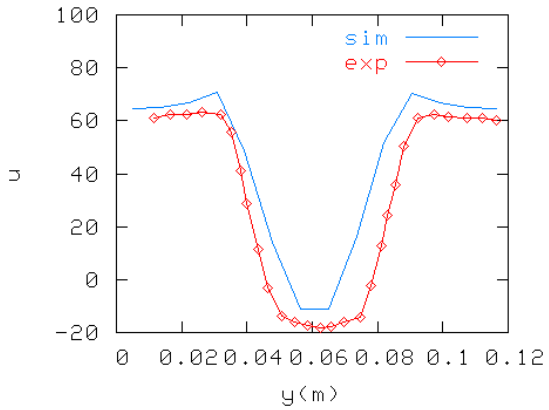

Figure 6.33 *Mean streamwise velocity profile at 0.061m after bluff-body*

The mean major species and temperature distributions are closely related to the mean flame thickness and mean flame position. Once they are properly simulated in LES, the mean major species field and temperature are also properly simulated. Fig. 6.34, Fig. 6.35 and Fig. 6.36 shows the distribution of instantaneous progress variable, instantaneous density and instantaneous flame front position. From Fig. 6.35, it is very clear that density varies along flame front and it can be related to progress variable.

The profiles of temperature, species and other important features of a premixed flame can be obtained using CFD tools employing detailed or simplified chemical mechanism. These profiles are evaluated by using CHEM1D [91] for a lean propane-air flame with equivalence ratio 0.6 and fresh mixture temperature 600 K (which is used for the present simulations).

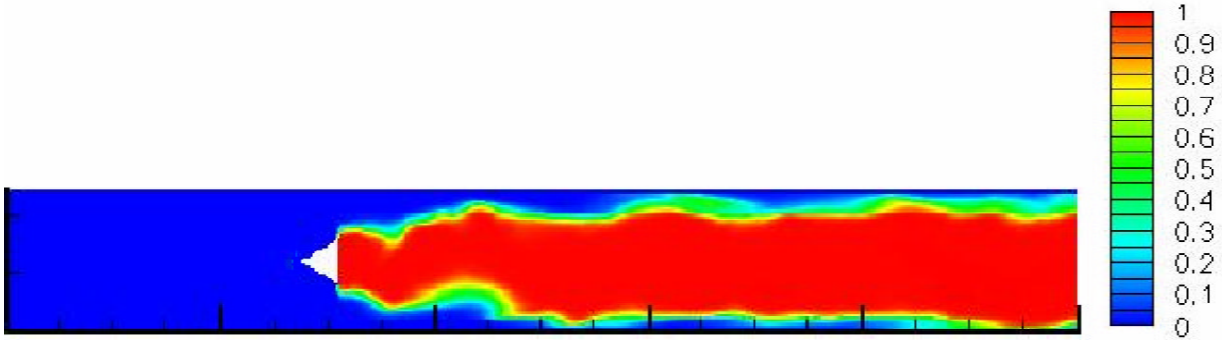

Figure 6.34 *Instantaneous progress variable*

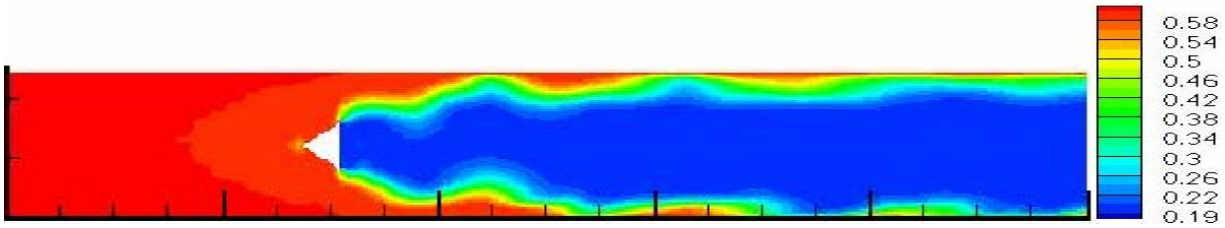

Figure 6.35 Instantaneous density

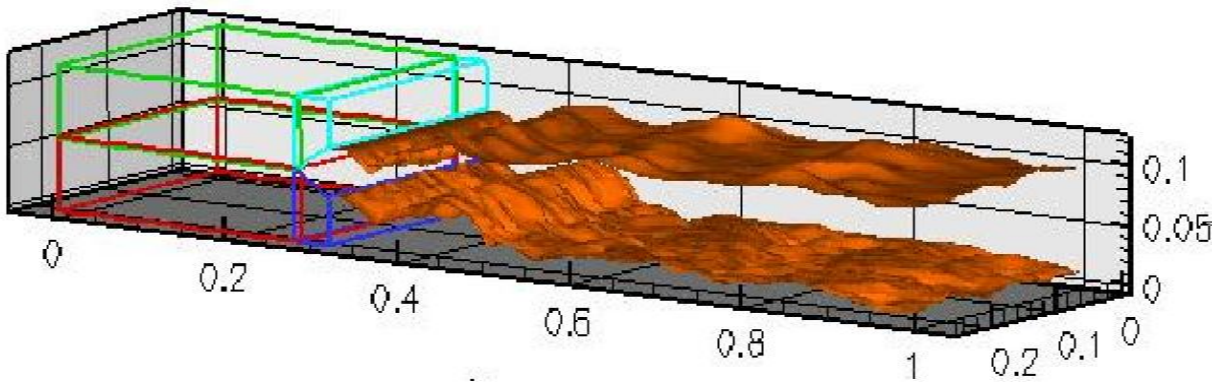

Figure 6.36 Instantaneous flame front

The time averaged CO_2 mole fractions at two transverse stations are plotted in Fig. 6.37 and Fig. 6.38. In Fig. 6.39 and Fig.6.40 time averaged O_2 mole fractions at two transverse stations are plotted. Fig. 6.41 and 6.42 shows the mean temperature predicted at the two transverse stations. The agreements of the mean velocity and major species from LES with the measurement are reasonably good. The mean temperature and major species are very sensitive to the position of reattachment point. A little difference of flame position will move some part of the flow field from unburnt zone to burnt zone, or vice versa.

In the present work the wrinkling model given by the Charlette (see section 4.3.3) has been used. By using this model it has been found that wrinkling factor varies in the range of 0 to 3. Instantaneous profile of wrinkling factor is shown in the Fig. 6.43. This range of values for this factor is quite good.

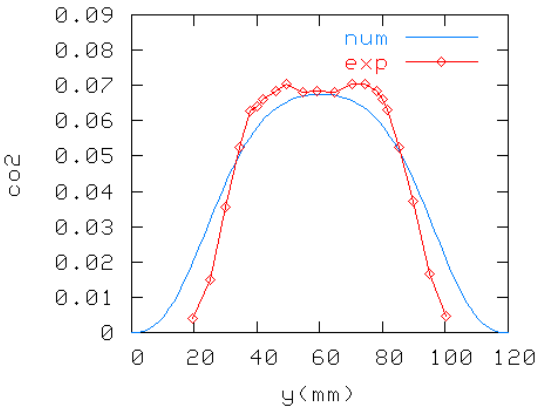

Figure 6.37 *CO_2 mole concentration at .15m after bluff-body*

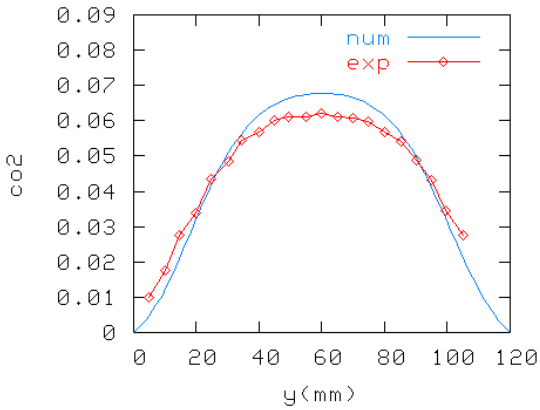

Figure 6.38 *CO_2 mole concentration at .35m after bluff-body*

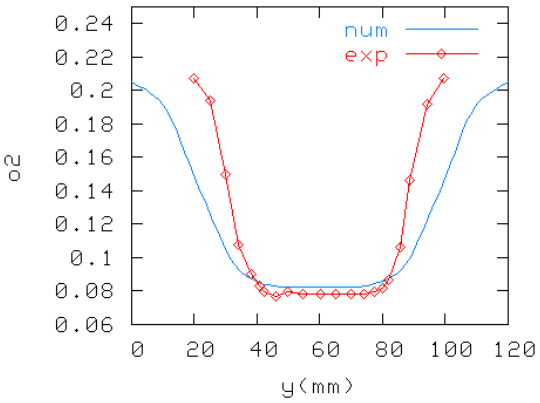

Figure 6.39 *O_2 mole concentration at .15m after bluff-body*

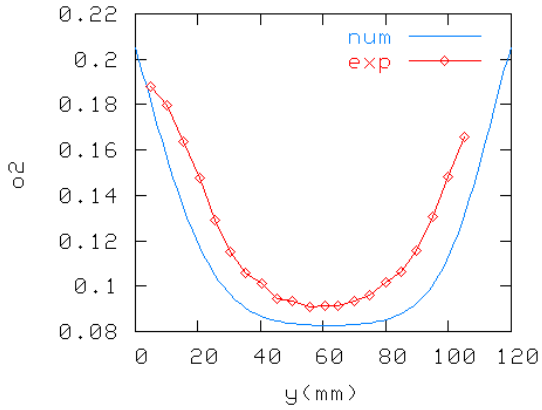

Figure 6.40 *O_2 mole concentration at .35m after bluff-body*

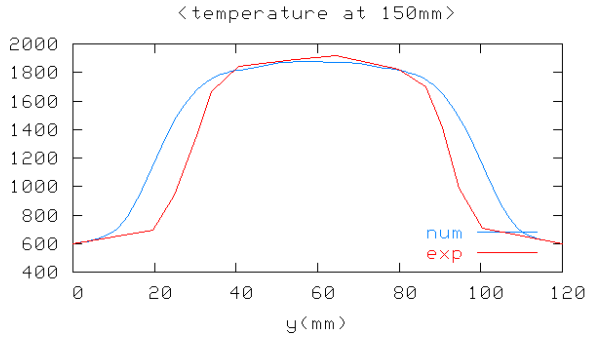

Figure 6.41 *Mean temperature profiles at .15m after bluff-body*

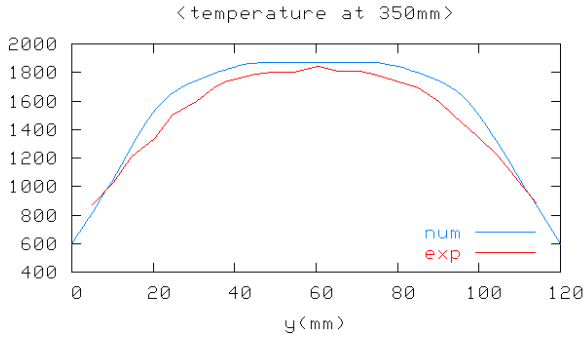

Figure 6.42 *Mean temperature profiles at .35m after bluff-body*

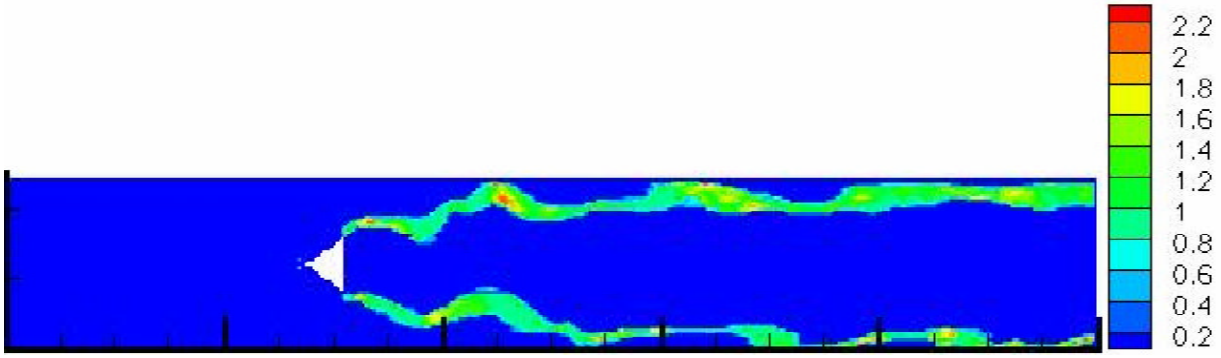

Figure 6.43 Wrinkling factor calculated by the Charlette

On the other hand, it has been found that with Pocheau's flame speed model wrinkling values varies from 0 to 50 (Fig. 6.44), and with Colins model (Fig. 6.45) it was found that wrinkling factor varies between 0 to 20. These values have been calculated by switching the wrinkling model from Charlette's model to these models. Maximum and minimum wrinkling factor values occur at the same location for the all the three wrinkling models.

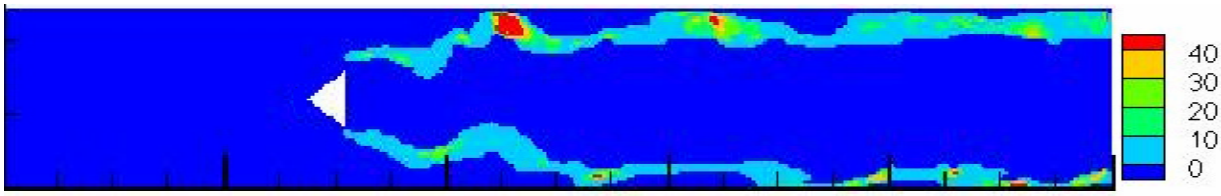

Figure 6.44 Wrinkling factor calculated by the Pocheau's model

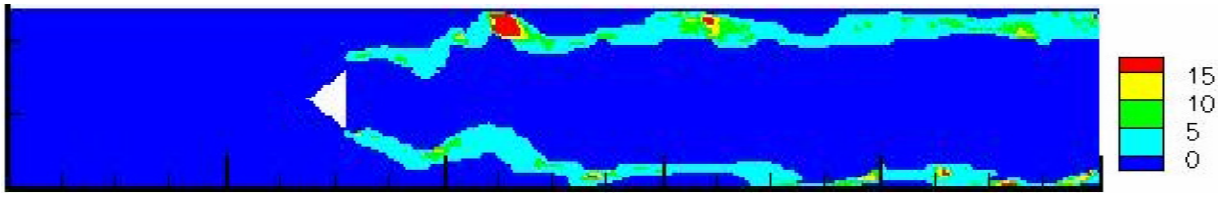

Figure 6.45 Wrinkling factor calculated by the Colin's model

6.3.4 Results obtained by using Artificial thickened model

In this section large eddy simulation of bluff-body stabilized by using artificial thickened model are presented. For this purpose one-step global chemistry model was considered.

$$C_3H_8 + 5O_2 \rightarrow 3CO_2 + 4H_2O \qquad (6.9)$$

Here the reaction rate given by equation (4.27) with pre-exponential factor *2.E9* and activation temperature 15,700k are considered. Value for the thickening factor considered for this case is equal to 25.

In these simulations it was found that the wrinkling factor for the present case play's an important role (more compared to the flame surface density model), especially near the bluff-body. Improper handling of this factor can cause flame entering behind the flame holder or the flame detachment from the flame holder. Fig. 6.46, Fig. 6.47 and Fig. 6.48 shows the distribution of instantaneous progress variable, instantaneous density and instantaneous flame front position. Nevertheless thickness of flame front in this case is more compared to flame surface density case.

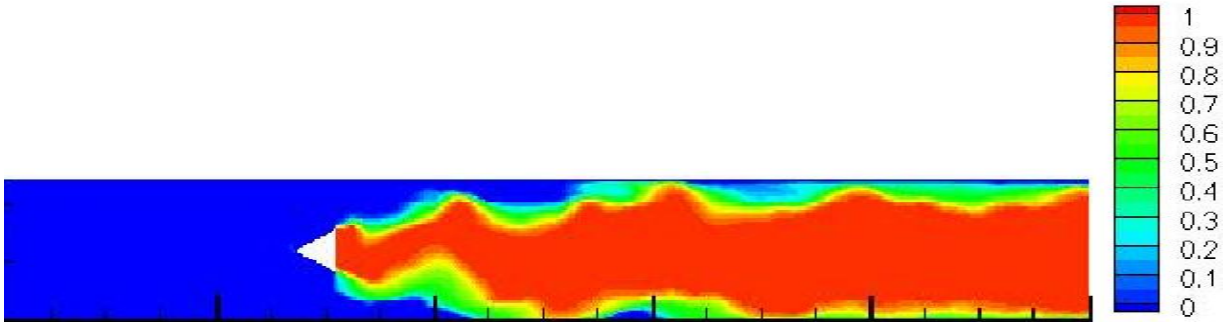

Figure 6.46 *Instantaneous progress variable*

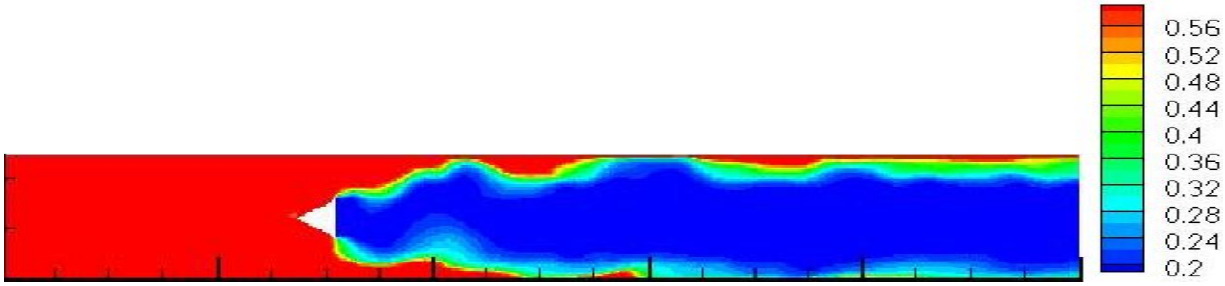

Figure 6.47 *Instantaneous density*

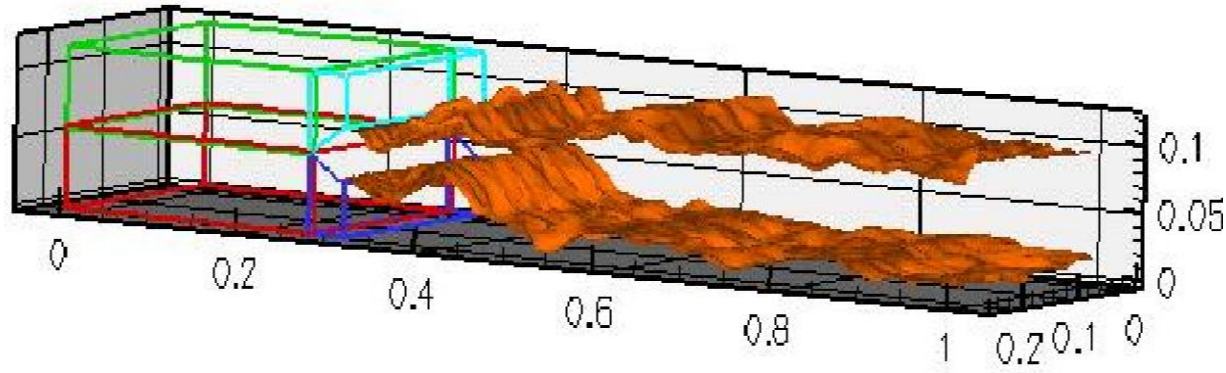

Figure 6.48 *Instantaneous flame front*

Fig. 6.49 shows the mean streamwise velocity distribution along the centre line. In the present simulation wrinkling model given by the Charlette (see section 4.3.3) has been used. By using this model it has been found that wrinkling factor varies in the range of 0 to 4.5. Instantaneous profile of wrinkling factor is shown in the Fig. 6.50. From the Fig. 6.49 it was clear the recirculation length is under-predicted and its size is half of the recirculation length given by the experiments. Due to this flame stabilization becomes a problem and the importance of wrinkling model increases.

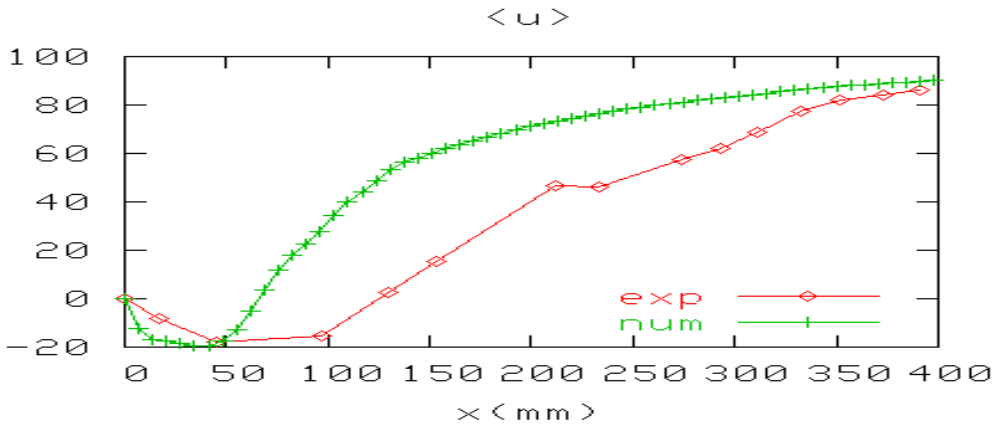

Figure 6.49 Axial velocity prediction along the centreline in the stream-wise direction

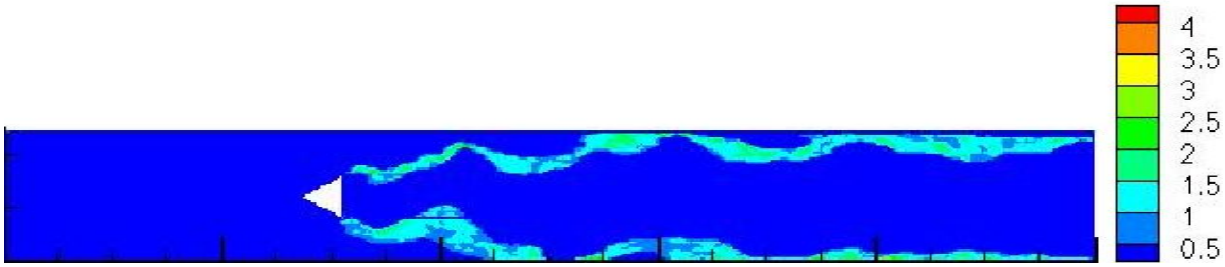

Figure 6.50 Wrinkling factor calculated by the Charlette

The time averaged CO_2 mole fractions at two transverse stations are plotted in Fig. 6.51 and Fig. 6.52. In Fig. 6.53 and Fig.6.54 time averaged O_2 mole fractions at two transverse stations are plotted. Fig. 6.55 and 6.56 shows the mean temperature predicted at the two transverse stations. The agreements of the mean velocity and major species from LES with the measurement are reasonably good.

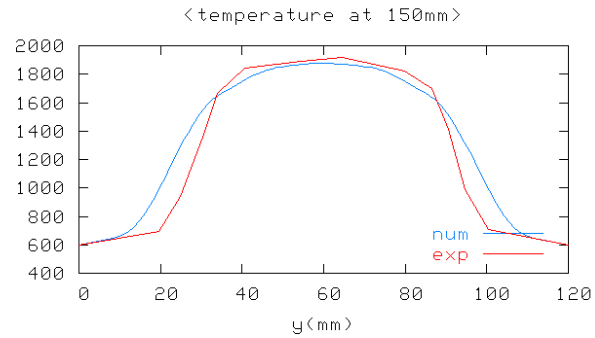

Figure 6.51 Mean temperature profiles at .15m after bluff-body

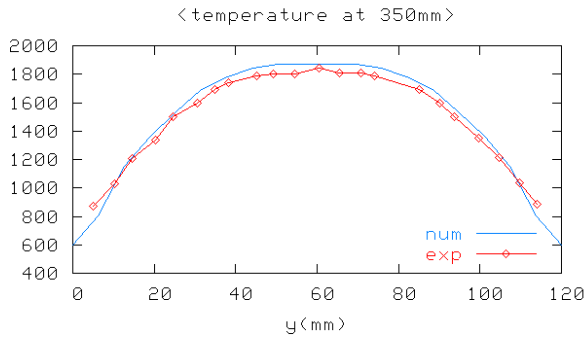

Figure 6.52 Mean temperature profiles at .35m after bluff-body

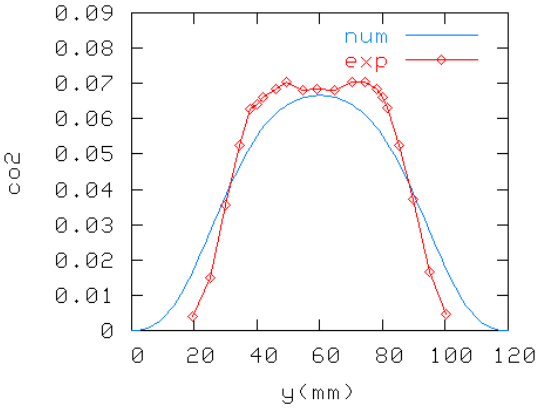

Figure 6.53 CO_2 mole concentration at .15m after bluff-body

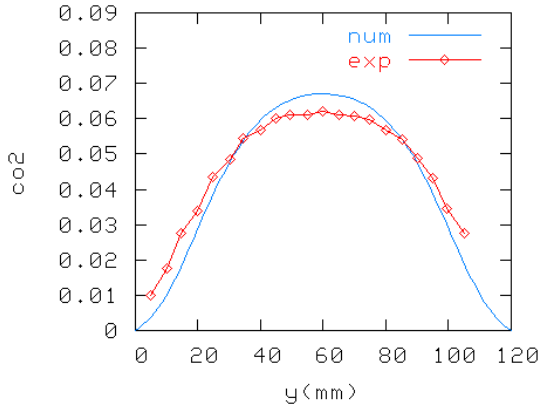

Figure 6.54 CO_2 mole concentration at .35m after bluff-body

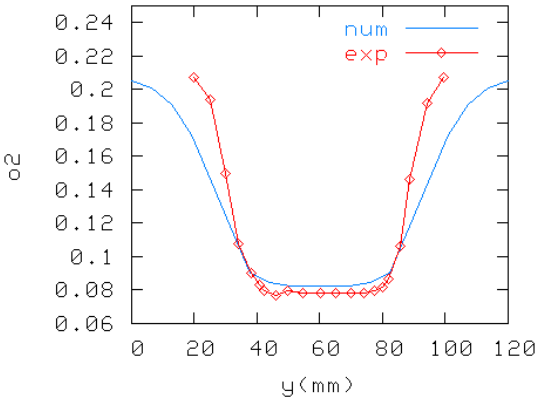

Figure 6.55 O_2 mole concentration at .15m after bluff-body

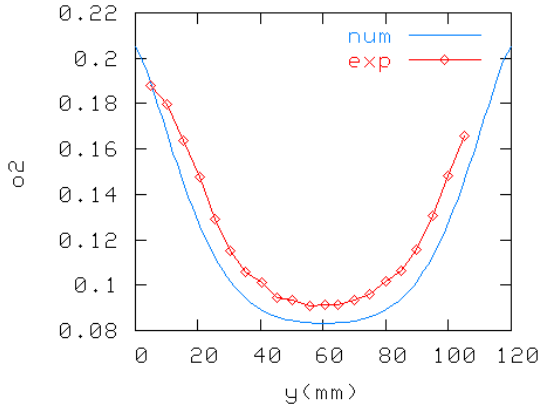

Figure 6.56 O_2 mole concentration at .35m after bluff-body

6.3.5 Comparison between Flame surface density and Artificial thickened flame model

The bluff body stabilized flame simulations mainly depends on the accurate capturing of the recirculation zone. From the simulations it is observed that among the two models the flame surface density approach is very stable and gives better results. This is mainly because the wrinkling factor is only present in the reaction term for the flame surface density approach,

whereas in the artificially thickened flame model it is present in both diffusion and the reaction term. Because of this reason it is very difficult to control the thickness of the flame in the case of artificially thickened model and increase the demands proper modelling of the wrinkling. Fig. 6.57 shows the comparison between axial velocities along the centreline. It is very clear that central circulation zone is under predicted in the both simulations. In artificial thickened model length of the circulation zone is smaller compared to the flame surface density approach. This explains the reason behind the stability of the flame surface density based calculations. Fig. 6.58 shows the comparisons between the temperature profiles. Temperature profiles mainly depend on the flame front position. In these simulations the flame front position is controlled mainly by the walls. And in both simulations flame-wall interactions are handled in same way (see section 4.4.3). Due to this reason temperature profiles of the both simulations are more or less identical.

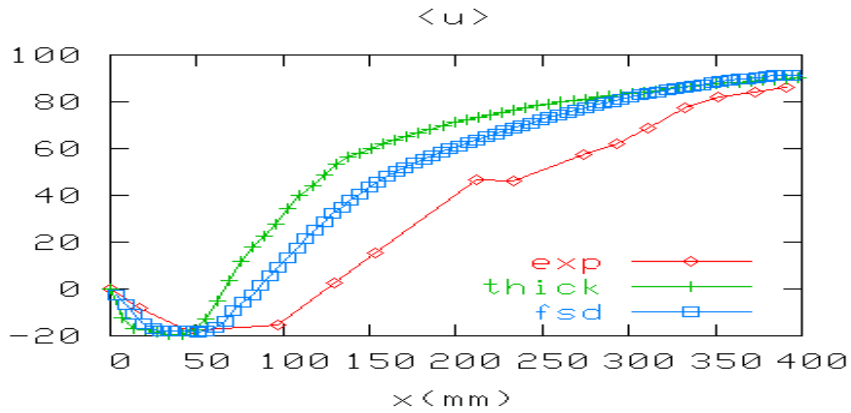

Figure 6.57 *Axial velocity prediction along the centreline in the stream-wise direction*

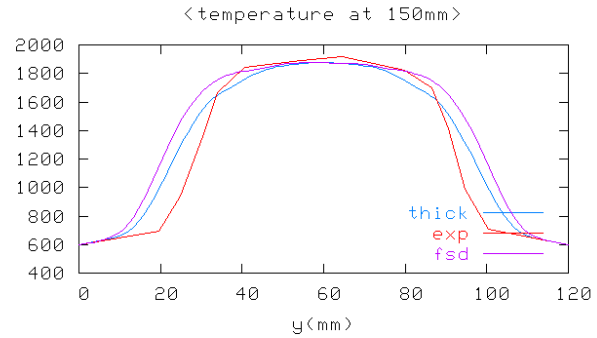

Figure 6.58 *Mean temperature profiles at .15m after bluff-body*

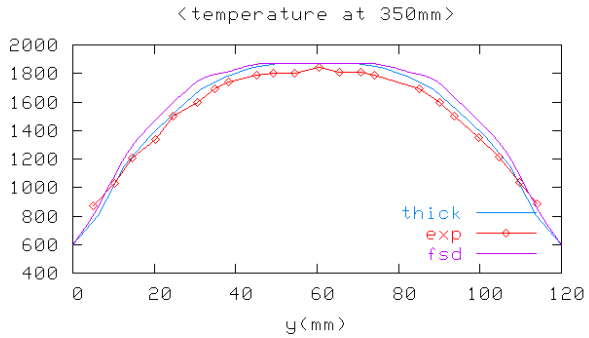

Figure 6.59 *Mean temperature profiles at .35m after bluff-body*

Chapter 7

Conclusions

In the present work large eddy simulations of non-reactive and reactive flows are performed. Large eddy simulations of non-reactive flows is related to the study of the performance of different Subgrid-scale models and where as Large eddy simulations of reactive flows is related to simulation of premixed flames.

In the study of the performance of different Subgrid-scale models following elements are investigated:

- Influence of the filter widths on the 3D-channel flow simulations are studied by considering the Smagorinsky model. For this purpose three different filter widths are considered. These filter widths are: 1) filter width based on volume of the grid cell 2) filter width based on area of the sides of the grid cell 3) filter width based on the anisotropic extension of the volume of grid cell. It has been found that bad results are found with the usage of the volume based filter width. This deficiency can be rectified by considering the anisotropic correction to this filter width. Nevertheless all these test cases give bad results for the Reynolds stress profiles.

- Robustness of the Germano-Lilly dynamic model is investigated by considering the four different cases. In these cases model coefficient is varied externally. The final 3D-channel flow simulations show that all the cases behave almost identical. To explain this phenomenon two different possible scenarios are considered. One is scale similarity assumption and other one is scale dependent situation. In the scale similarity case proper mathematical proof was given. But for the scale dependent case a probable reason was given. No mathematical proof was given for this case. This is mainly because implicit based LES method is used in this work.

- Different dynamic procedures are compared. For this purpose Germano-Lilly model, Localized dynamic model and Lagrangian dynamic model are considered. During the channel flow simulations no homogeneous averaging is done for the model coefficient. Main reason behind this is to test the models under the real conditions, where no homogeneous condition exists. Nevertheless Lagrangian dynamic model gives better results compared to the other dynamic models. Main reason behind this

behaviour is the averaging performed in time by considering the fluid particle history along its path line. This is more reasonable compared to the spatial type time averaging done in other dynamic procedures.

- Performance of the mixed models is studied by relaxing the scale similarity term. It has been found that with more relaxing Smagorinsky model coefficient value increases. Nevertheless the overall behaviour of the mixed model is very good compared to Germano-Lilly dynamic Smagorinsky model.
- A new anisotropic one-equation SGS model is developed in this work. Performance of this model is tested against the existing isotropic one-equation model. Both these models are capable of predicting backscatter. The simulation results show that both models are able to predict accurate results, which proves that with coarse grids the usage of the one equation model is recommended.
- After comparing all the models, it has been found that one equation anisotropic model gives the best results. But unfortunately this model requires more computation power compared to the other models and it approximately 2 times the Germano-Lilly model. Also it has been found that Lagrangian dynamic model provides a better compromise between computational effort and performance. Computational overhead in Lagrangian dynamic model is about 10% above the CPU requirements of the other dynamic models.
- Performance of the Lagrangian dynamic model and the one equation anisotropic model are also compared by considering the spanwise rotating channel flow. Simulations show that anisotropic model predicts better results compared to the Lagrangian dynamic model. But nevertheless Lagrangian dynamic model also predicts good results.

In the second part of the work large eddy simulations of premixed flames are performed by considering a Bluff-body stabilized flame. These simulations are performed by considering the artificial thickened model and the flame surface density approach with algebraic expression for the flame surface density. For this purpose a simple technique for the density coupling is proposed for the extension of the incompressible solver to variable solver. In this technique, first divergence of the velocity is evaluated by using the progress variable equation, relation between density and the progress variable and the continuity equation. By using this derived equation density is updated with help of continuity equation. This derived equation is also used for the convective outlet velocity boundary treatment. A two way

approach for the handling of flame wall interactions is presented. Effect of different flame wrinkling models on the simulations is studied for the flame surface density case. It has been found that Pocheau's flame speed model gives unrealistic values where as Charlette’s model gives reasonable values. From the simulations it is observed that the flame surface density approach is very stable and gives better results compared to the artificial thickened flame model. This is mainly because the wrinkling factor only present in the reaction term for the flame surface density approach, where as in artificial thickened model both diffusion and the reaction term consists this term. For this reason it is very difficult to control the thickness of the flame in the case of the artificialy thickened flame model and this model demands proper modelling of the wrinkling.

The simulation results show that, velocity is over-predicted and the recirculation length is under-predicted for the both premixed models. In artificial thickened flame model the length of the circulation zone is smaller compared to the flame surface density approach. The overall agreement between experimental and computational results is good for the both the simulations in the case of species and temperature profiles for downstream of the bluff body.

Using the proposed numerical technique one can formulate an equation for the density. This equation is formulated by using the derived equation for the divergence of the velocity and the continuity equation. Instead of progress variable equation one can solve this derived equation for the density for simulating premixed combustion flows without using density update approach proposed in this work. Nevertheless for this purpose basic structure of the FASTEST3D solver has to be changed and is left for the future.

Bibilography

1 Buenos Aires, Weltenergiekonzern, 2001.

2 Turns S.R.,“An introduction to combustion: concepts and applications”. McGraw–Hill International Editions, 2000.

3 Glassman I., “Combustion”, Third edition, Academic press, 1996.

4 Kohse-Höinghaus K., Barlow R.S., Aldén M. and Wolfrum J, “Combustion at the focus: laser diagnostics and control”. 50th anniversary lecture on 30th International Symposium on Combustion”, Proceedings of the Combustion Institute, **30**, 2004.

5 Pope S. B, “Turbulent Flows”, Cambridge University Press, 2000.

6 Kolmogorov A. N., “Dissipation of energy in the locally isotropic turbulence” C. R. Acad. Sci. USSR, **32**,16-18, 1941.

7 Kolmogorov A. N., “The local structure of turbulence in incompressible viscous fluids for very large Reynolds numbers”. Dokl. Akad. Nauk SSSR, **30**,301-305, 1941.

8 Kim J., Moin P. and Moser R., “Turbulence statistics in fully developed channel flow at low Reynolds number”, Journal of Fluid Mechanics, **177**,133-166, 1987.

9 Le H., Moin P. and Kim J. Direct numerical simulation of turbulent flow over a backward-facing step”. Journal of Fluid Mechanics, **330**,349–374, 1997.

10 Hinze J. O., “Turbulence”. McGraw-Hill, New York, 1975.

11 Germano M., “Turbulence: the filtering approach”, Journal of Fluid Mechanics, **238**, 325-336, 1992.

12 Moin P., “Numerical and physical issues in large eddy simulation of turbulent flows”, In Proceedings of the International Conference on Fluid Engineering, Tokyo, 1997.

13 Lund T. S. and Kaltenbach H. J. “Experiments with explicit filtering for LES using a finite difference method”, Annual Research Briefs, Centre for Turbulent Research, 91-105, 1994.

14 Frank-Kamenstsky D.A.: “Diffusion and heat exchange in chemical kinetics” Moscow, third edition, 1987.

15 Poinsot T. and Veynante D. “Theoretical and numerical combustion” ,R.T. Edwards, Inc. Philadelphia USA, 2001

16 Burke, S.P. and Schumann T.E.W., "Diffusion Flames", Industrial Engineering chemistry, **20**, 998-1004, 1928.

17 Peters N., “Laminar Diffusion flamelet Models in non-Premixed turbulent combustion”, Progr. Energy Combust. Sci., **10**, 319-339, 1984.

18 Maas, U. and Pope, S. B., "Implementation of Simplified Chemical Kinetics Based on Intrinsic Low-Dimensional Manifolds", Twenty-Fourth Symposium (International) on Combustion, Proceedings of the Combustion Institute, Pittsburgh,

103-112, 1992.

19 Williams F.A., “Recent advances in theoretical descriptions of turbulent diffusion flames”, In S.N.B. Murthy, editor, Turbulent mixing in non-reactive and reactive flows, Plenum press, New York, 189–208, 1975.

20 Peters N., “turbulent combustion” Cambridge university press, 2000.

21 Bilger R.W., “Conditional moment closure for turbulent reaction flows”, *Physics of Fluids A,* **5**, 434–444.,1993.

22 Klimenko A.Y., “Multicomponent diffusion of various scalars in turbulent flows” J. *Fluid Dynamics,* **25** ,327–334,1990.

23 Williams F.A., “Combustion theory” Benjamin Cummings, 1985.

24 Damköhler G.,“Der Einfluß der Turbulenz auf die Flammengeschwindigkeit in Gasgemischen“, *Z. Elektrochem.* **46**,601–652. 1940.(English translation NASA Tech. Mem. 1112, 1947).

25 Bradley D. “How fast can we burn?”, Proceedings of the Combustion Institute, **24**, 247–262., 1992.

26 Borghi R., “Turbulent combustion modelling”, Progress in Energy and combustion Science, **14**,245–292,1988.

27 Spalding D.B. “Mixing and chemical reaction in steady confined turbulent flames”. Proceedings of the Combustion Institute., **13**,649-657, 1971.

28 Smagorinsky J., “General circulation experiments with the primitive equations I. The basic experiments” J. Mon Weather Rev. 91, 99-164,1963

29 Yoshizawa A., “Eddy-viscosity-type subgrid-scale model with a variable Smagorinsky coefficient and its relationship with the one-equation model in large eddy simulation”, Physics of Fluids, **25**(9), 1539-1538, 1982.

30 Clark R. A., Ferziger J. H. and Reynolds W. C., “Evaluation of subgrid-scale models using an accurately simulated turbulent flow”, J. Fluid Mech., **91**(1), 1-16

31 Deardorff J. W., “A numerical study of three dimensional turbulent channel flow at large Reynolds number flows, J. Fluid Mech., **41**, 453-465

32 Scotti A., Meneveau C. and Lilly D.K., “ Generalized Smagorinsky model for anisotropic grids”, Physics of Fluids A. **5**(9), 2306-2308, 1993.

33 Van Driest E., “On turbulent flow near a wall”, J. Aeronaut. Sci., **23**, 1007-1011, 1956.

34 Lund T. S., “On dynamic models for large eddy simulation,” Annual Research Briefs, Centre for Turbulence Research, Stanford University NASA-Ames, **177,** 1991.

35 Germano M., Piomelli U., P. Moin P. and Cabot W. H., “A dynamic subgrid-scale eddy viscosity model”, Phy. Fluids, **3**(7), 1760-1765,1991.

36 Lilly D. K., “A proposed modification of the Germano subgrid-scale closure method”, Phys. Fluids, **4**(3), 633-635, 1992

37 Ghosal S., Lund T. S., Moin P. and Akselvoll K., “ A dynamic localization model for large-eddy simulation of turbulent flows”, Journal of Fluid Mechanics, **286**, 229-255, 1995.

38 Piomelli U., and Liu J., " Large eddy simulation of rotating channel flows using a localized dynamic model", Phys. Fluids, **7**(4), 839-848, 1995.

39 Meneveau C., Lund T. S. and Cabot W. H., " A Lagrangian dynamic subgrid-scale model of turbulence" J. Fluid Mech., **319**, 353-385, 1996.

40 Sohankar A., Davidson L. and Norberg C., "Large eddy simulation of flow past a square cylinder: Comparison of different subgrid scale models", Trans. ASME, J. Fluids Eng., **122**, 39-47. 2000.

41 Aupiox B., "Subgrid-scale models for homogeneous anisotropic turbulence", Proceedings of Euromech colloquium 199, Direct and large eddy simulation of turbulence, **15**, 36-66.

42 Abba A., Bucci R., Cercignani C. and Valdttaro L., "A new approach to the dynamic subgrid.scale model", Unpublished.

43 Carati D. and Cabot W., "Anisotropic eddy viscosity models", Proceedings of the summer program- Center for Tubulence Research, Stanford University, 249-259, 1996.

44 Akula R. A., Sadiki A., And Janicka J., Turbulent Shear Flow Phenomena IV, **2**, 595-600., 2005.

45 Speziale C. G. and Gatski T. B., 1997, "Analysis and modelling of anisotropies in the dissipation rate of turbulence", Journal of Fluid Mechanics, **344**, 155-180.

46 Bardina J., Ferziger J. H. and Reynolds W. C., "Improved subgrid scale models for large eddy simulation", AIAA paper 80–1357, 1980.

47 Liu S., Meneveau C. and Katz J.,"On the properties of similarity of subgrid-scale models as deduced from measurements in a turbulent jet", Journal of Fluid Mechanics, **275**, 83-119, 1997.

48 Kim J., Mom J. P., and Moser R., "Turbulence statistics in fully developed channel flow at low Reynolds number," Journal of Fluid Mechanics, **177**, 133-147, 1987.

49 Cabot W., "Large eddy simulation of passive and buoyant scalars with dynamic subgrid-scale models," Annual Research Briefs, Centre for Turbulence Research, Stanford University/NASA-Ames, **191**, 1991.

50 Vreman B., Geurts B. and Kuerten H., "On the formulation of the dynamic mixed subgrid-scale model", Phys. Fluids, **6**(12), 4057-4059, 1994.

51 Chollet J. P. and Lesieur M., "Parametrization of small scales of three dimensional isotropic turbulence utilizing spectral closures", J. Atmos. Sci., **38**, 2747-2757.

52 Metais O. and Lesieur M., "Spectral large-eddy simulation of isotropic and stably stratified turbulence", Journal of Fluid Mechanics, **256**, 157-194, 1992.

53 Porté-Agel F., Meneveau C. and Parlange M. B., "A scale-dependent dynamic model for large-eddy simulation: an application to the atmospheric boundary layer", Journal of Fluid Mechanics, **415**, 261-284, 2000.

54 Stolz S. and Adams N. A., "An approximate deconvolution procedure for large-eddy simulation", Phys. Fluids, **11**(7), 1699-1701, 1999

55 Kim W.W. and Menon S., "Numerical modelling of turbulent premixed flames in the thin-reaction-zones regime", Combustion Science and Technology, **160**, 113–150, 2000

56 Freitag M. and Janicka J., “Investigation of a strongly swirled unconfined premixed flame using LES”, Proceedings of the Combustion Institute, in press, 2006.

57 Boger M., Veynante D., Boughanem H. and Trouvé A., “Direct numerical simulation analysis of flame surface density concept for large eddy simulation of turbulent premixed combustion”, Proceedings of the Combustion Institute, 917-925, 1998

58 Charlette F., Meneveau C. and Veynante D., “A power-law wrinkling model for LES of premixed turbulent combustion. Part I : Non-dynamic formulation and initial tests”. Combustion and Flame, **131**, 159-180, 2002

59 Charlette, F., Meneveau, C. and Veynante, D., “ A Power-law wrinkling model for LES of premixed turbulent combustion. Part II : Dynamic formulation”, Combustion and Flame, **131,**181-197, 2002

60 Kerstein A. R., Ashurst W T, and Williams F. A., “The field equation for interface propagation in an unsteady homogeneous flow field”, Physical Review A, **37**, 2728-2731, 1988.

61 Smith T. M. and Menon S. “The structure of premixed flames in a spatially evolving turbulent flow”, Combustion Science and Technology, **119**, 77-106, 1996.

62 Kim W. W, Menon S, and Mongia H. “Large eddy simulations of a gas turbine combustor flow”, Combustion Science and Technology, **143**, 25-62, 1999.

63 Pocheau A, “Scale invariance in turbulent front propagation”. Physical Review E, **49**, 1109-1122, 1994.

64 Kerstein A.R. and Ashurst W.T., “Field equation for interface propagation in an unsteady homogeneous flow field”, Physical reviews A, **37(7)**, 2728–2731, 1998.

65 Warnatz J., “Resolution of gas phase and surface chemistry into elementary reactions”, Proceedings of the Combustion Institute, **24**, 553–579, 1992.

66 Zimont V.L. “Theory of turbulent combustion of a homogeneous fuel mixture at high Reynolds number”. Combustion, explosion, and shock waves, **15**, 305–311, 1979.

67 Karpov V., Lipatnikov A. and Zimont V. “A test of an engineering model of premixed turbulent combustion”, Proceedings of the Combustion Institute, **26**, 249–257., 1996.

68 Zimont V.L., “Gas premixed combustion at high turbulence: turbulent flame closure combustion model”, Experimental Thermal and Fluid Science, **21**,179–186, 2000.

69 Flohr P. and Pitsch H., “A turbulent flame speed closure model for LES of industrial burner flows”, Proceedings of the summer program, Centre for Turbulence Research, 169–179, 2000.

70 Zimont V.L. and Battaglia V., “RANS, LES and hybrid RANS/LES turbulent premixed combustion TFC model”, Joint meeting of the Scandinavia–Nordic and Italian sections of the combustion institute, **2.6**, Ischia, Italy, 2003.

71 Weller H.G., “The development of a new flame area combustion model using conditional averaging”, Thermo-fluids section report TF–9307, Imperial college science, Technology and medicine, 1993.

72 Weller H.G., Tabor G., Gosman A.D. and Fureby C., “Application of a flame wrinkling LES combustion model to a turbulent mixing layer”. Proceedings of the Combustion Institute, **27**, 899–907, 1998

73 Fureby C., “Large eddy simulation of combustion instabilities in a jet engine afterburner model”, Combustion Science and Technology, **161**, 213–243, 2000.

74 Boger M. and Veynante D., “Large eddy simulation of a turbulent premixed V-shaped flame”, 8th European Turbulence, Barcelona, Spain, 2000

75 Hawkes E.R. and Cant R.S., “Implications of a flame surface density approach to large eddy simulation of premixed turbulent combustion”, Combustion and Flame,**126**, 1617–1629., 2001

76 Butler T.D. and O’Rourke P.J., “A numerical method for two-dimensional unsteady reacting flows”, Proceedings of the Combustion Institute, **16**, 1503–1515, 1997.

77 Colin O. Ducros F. Veynante D. and Poinsot T., “A thickened flame model for large eddy simulation of turbulent premixed combustion”, Physics of Fluids,**12**(7),1843–1863, 2000.

78 Meneveau C. and Poinsot T., “Streching and quenching of flamelets in premixed turbulent combustion”, Combustion and Flame, **86**, 311-332, 1991.

79 Poinsot T., Veynante D., and Candel S.,“Quenching processes and premixed turbulent combustion diagrams”, Journal of Fluid Mechanics, **228**, 561-605, 1991.

80 Schäfer M., “Numerik im Maschinenbau”, Springer Verlag Berlin,1999.

81 Ferziger J.H. and Peric M., “Computational Methods for Fluid Dynamics”, Springer Verlag, Berlin, Heidelberg, 1999

82 Stone L. H., “Iterative solution of implicit approximations multidimensional partial differential equations”, SIAM J. Numer. Anal., **5** (3), 530-558, 1968.

83 Leister H. J. and Peric M., “Vectorized strongly implicit solving procedure for seven-diagonal coefficient matrix”, Int. J. Numer. Meth. Heat Fluid Flow, **4**, 159-172, 1994

84 McMurtry P. A, Jou W. H , Riley J. J. and Metcalfe R. W. “Direct Numerical Simulations of a Reacting Mixing Layer with Chemical Heat Release”, AIAA Journal, **24**(6), 962-970, 1986

85 Boersma B. J., “Direct numerical simulation of a turbulent reacting jet”, Annual Research Briefs 1998, Centre of turbulence research, Stanford University, 47-56, 1998.

86 Najm H. N., Wyckoff P. S., and Knio O. M., “A Semi-Implicit Numerical Scheme for Reacting Flow”, J. Computational Physics, **143**, 381-402.1998

87 AGARD, “A selection of test cases for the validation of large-eddy simulations of turbulent flows”, AGARD advisory report, **345**, 1998.

88 Krajnovic S. and Davidson L., "A Mixed One-Equation Subgrid Model for Large-Eddy Simulation", International Journal of Heat and Fluid Flow, **23**(4), 413-425, 2002.

89 Sjunnesson A., Olovsson S., Sjöblom B., “Validation rig – a tool for flame studies”, Internal Report VFA 9370–308, Volvo Flygmotor, Sweden, 1991.

90 Nilsson P., Bai X. S, “Effects of flame stretch and wrinkling on co-formation in

turbulent premixed combustion", Proceedings of the Combustion Institute, **29**, 1873–1879.

91 Somers B., "The simulation of flat flames with detailed and reduced chemical models", PhD. Thesis, 1994.